Apparent Stress Estimates of Seismic Events Associated with Underground Mining Operations in Sedimentary Rock Units:

Implications for Improving Underground Roof Collapse Warning Systems

by

Elige Buckhanan Grant V

Thesis submitted to the Faculty of the
Virginia Polytechnic Institute and State University
in partial fulfillment of the requirements for the degree of
Master of Science in the Department of Geosciences

Dr. Martin C. Chapman (Chair)
Dr. J. Arthur Snoke
Dr. Anthony Iannacchione

July 21, 2006
Blacksburg, Virginia

APPARENT STRESS ESTIMATES OF SEISMIC EVENTS ASSOCIATED WITH UNDERGROUND MINING OPERATIONS IN SEDIMENTARY ROCK UNITS:

IMPLICATIONS FOR IMPROVING UNDERGROUND ROOF COLLAPSE WARNING SYSTEMS

Elige Buckhanan Grant V

Abstract

We analyze recordings of seismic events induced by underground mining operations at the Moonee Colliery, located in Australia, and at the Springfield Pike Limestone Quarry, located in the United States. The data were recorded underground in the vicinity of active mining operations and were initially used by the monitoring systems at the two mines to evaluate the potential for roof failure based on the temporal and spatial distribution of the seismic activity. In an earlier study, the roof failures at the two underground mine locations were found to be the result of two distinct failure processes, both of which were correlated with escalated seismic activity before the roof collapsed. In this study, we reexamine the recordings of these seismic emissions for a further assessment of the state of instability in the roof.

We estimate the static seismic moment and radiated seismic energy for each recorded seismic event induced by mining operations at the two underground mine locations. These seismic source parameters are estimated from source spectra have been corrected for the instrument response, propagation effects and bandwidth limitations. The apparent stress, which provides an estimate of the stress drop (or stress release) associated with a seismic event, is then determined from the product between the modulus of rigidity and the ratio between the radiated seismic energy and static seismic moment. The validity of constant stress drop scaling for the seismic events at the two underground mine locations is tested. Estimation of the seismic source parameters indicate that the stress drop of the mining induced events increases over three orders of magnitude of increasing seismic moment (10^6 N·m $\leq M_0 \leq 10^9$ N·m) and indicate a divergence from constant stress drop scaling. When these results are compiled with the results from seven other independent studies, which analyzed the seismicity associated with a variety of seismogenic environments, this trend is found to span over ten orders of magnitude of seismic moment (10^6 N·m $\leq M_0 \leq 10^{16}$ N·m).

The observation that the mining induced events do not conform to constant stress drop scaling may assist in gaining a better understanding of the evolution of the roof failure process. We have found that the stress drop at one of the studied mines appears to increase through time prior to a roof collapse. More data are necessary to test this hypothesis. If this hypothesis is validated, it would have important implications for monitoring roof stability. Incorporation of near-real-time estimates of the stress drop into the existing seismic monitoring protocol may provide improved warning of imminent roof collapse hazards.

Acknowledgements

Table of Contents

List of Figures

List of Tables

Glossary of Symbols

- A Rupture area
- α P-wave velocity
- β S-wave velocity
- $c^{\#}$ "Sharpness" constant
- E Total strain (or elastic) energy released during a seismic event
- E_C Energy lost in creating new crack surfaces during rupture propagation
- E_F Energy lost in creating thermal energy from the work done by frictional forces
- E_L Accounts for the energy lost due to wave propagation effects
- E_S Energy lost in generating seismic radiation
- E_S / M_0 Ratio between the radiated seismic energy and seismic moment
- f Continuous frequency
- f_c Corner frequency
- f_{max} The high-frequency limit of the radiated seismic spectrum due to source or propagation effects
- f_{min} The low-frequency limit of the radiated seismic spectrum due to noise or band-limitations
- Δf Frequency interval
- F Factor that depends on S
- γ High-frequency displacement amplitude fall-off rate
- $H(t)$ Heaviside function
- η Seismic efficiency factor
- I_{D2} Integral of the square of the ground displacement
- I_{V2} Integral of the square of the ground velocity
- M_0 Static (or Scalar) seismic moment
- μ Modulus of rigidity
- N Number of sampled points in the time domain
- ν Discrete frequency sample
- ν_1 Discrete frequency sample of the low-frequency band-limited range
- ν_2 Discrete frequency sample of the high-frequency band-limited range
- ν_Ω Discrete frequency sample of the frequency just below the high frequency displacement amplitude fall-off

- ν_Ψ Discrete frequency sample of the frequency just above the low-frequency acceleration amplitude rise
- OS   Over-Shoot
- Ψ_0 Zero-period (or infinite frequency) acceleration amplitude
- Q Quality factor
- r Radius of circular fault
- R Hypocentral distance
- $\mathcal{R}_{\varphi\theta}$ Mean radiation pattern
- $\langle\mathcal{R}_{\varphi\theta}\rangle$ Root-mean-squared (RMS) radiation pattern
- ρ Density
- σ_a Apparent stress
- σ_B Brune stress drop
- σ_D Dynamic (or effective) stress drop
- $\Delta\sigma$ Static stress drop (difference between initial stress and final stress)
- $\bar{\sigma}$ Average stress (between the initial stress and final stress)
- σ_0 Initial shear stress
- σ_1 Final shear stress
- σ_F Frictional shear stress
- S Factor that accounts for the conversion of S-waves to P-waves
- t Continuous time
- Δt Time interval
- θ Discrete time sample
- τ Rise time
- T Travel time between source and receiver
- t^* Near-receiver propagation effects
- T^* Represents the combined near-receiver propagation effects and distance dependent propagation effects
- $u(t)$ Continuous displacement time-series
- $\mathring{u}(t)$ Continuous velocity time-series
- $U(f)$ Continuous Fourier displacement amplitude spectrum
- $\mathring{U}(f)$ Continuous Fourier velocity amplitude spectrum
- $\bar{u}$ Seismic slip spatially averaged over the rupture area
- υ Arbitrary wave velocity
- Ω_0 Zero-frequency displacement amplitude

Chapter 1: Introduction

This study analyzes the seismicity associated with roof instability during underground mining operations. The data sets were provided by the National Institute for Occupational Safety and Health (NIOSH). This study builds upon that of both Iannacchione *et al.* [2005a] and Iannacchione *et al.* [2005b]. In the [2005b] study, three different roof failure processes were characterized: Progressive, Episodic and Continuous. Progressive roof failure processes were characterized by the progressive nature of the failure process, in which the collapse of a section of roof often led to the initiation of failure and ultimate collapse of neighboring portions of roof until the strata in the roof equilibrated. Episodic roof failure processes were characterized by a significant amount of seismicity associated with the failure and ultimate collapse of one, large portion of roof. Continuous roof failure processes were characterized by constant, continuous caving of the roof behind long-wall coal mining operations (i.e. no catastrophic, sudden collapse of roof). This study focuses on further characterization of a subset of the seismic events involved in the work of Iannacchione *et al.* [2005b] using estimation techniques similar to that described in Iannacchione *et al.* [2005a].

1.1   Study Location Descriptions of the Two Data Sets

The first data set we study is from the Moonee Colliery, a longwall coal mining operation located in New South Wales 100 km north of Sydney, Australia [Iannacchione *et al.* (2005b)]. The Moonee Colliery data set involves seismic events that eventually lead to the ultimate collapse of approximately 10,000 square meters of roof. Typical longwall coal mine operations are characterized by a continuously caving roof behind the active mining operations. Instead, this mine is characterized by episodic roof failures, where the roof collapses in large, discrete segments. The second data set is from the Springfield Pike Quarry, a room-and-pillar limestone quarry in south-western Pennsylvania, USA [Iannacchione *et al.* (2005b)]. The Springfield Pike Quarry data set involves seismic events that lead up to over ten roof collapse events. This mine is characterized by progressive roof failures, where the failure of a portion of roof often leads to the progressive failure of neighboring portions of roof. The geographical locations of the Moonee Colliery and the Springfield Pike Quarry are illustrated in Figure (1.1).

1.2   Mitigating Hazards of Roof Collapse Events

Roof falls and roof caving events are serious hazards. Efforts are ongoing to improve the technology to help minimize the hazards to miners and equipment in the underground environment. The ability to recognize these hazards before they occur is highly dependent on our understanding of the failure processes [Iannacchione *et al.* (2005b)]. These events are not the result of sudden rock bursts or implosions of the rock mass. Instead, the seismic events are associated with the roof failure process leading up to a roof collapse, which consists of the progressive development of fractures and of the dislocations across these fractures within the rock mass due to both shear and tensile forces.

Iannacchione *et al.* [2005b] examined the characteristics of seismic events at both the Moonee Colliery and the Springfield Pike Quarry. They observed that there are significant

differences in the nature of the seismicity at the two sites. This observation led to the characterization of each mine in terms of the three different roof failure processes noted above. Iannacchione *et al.* [2005a] examined the characteristics needed to discriminate the seismic signals associated with rock fracturing in the roof and rock impacting the mine floor, which we use in this study to identify potential fall events directly from the seismic recordings. In that [2005a] study, it was found that the rock fracturing events radiated more energy than the rock impact events.

Iannacchione *et al.* [2005b] point out that safer mine layouts and better warning system algorithms can be developed by incorporating seismic monitoring systems in the vicinity of mining operations and assessing the stability of the underground structures in near real time. The goal of this study is to develop a better understanding of the different failure processes by making estimates of the seismic source parameters from the recordings of the seismic event emissions and using these estimates to quantify the changes in stress and the evolution of the failure process through time. A better seismological understanding of the nature of the seismic event emissions would offer better physical insight into the stability of the material in the roof.

1.3   Premise of Study

We determine the Seismic Moment (M_0), Radiated Seismic Energy (E_s), and Apparent Stress (σ_a), after Keilis-Borok [1960], Boatwright and Fletcher [1984] and Wyss and Brune [1968], respectively, for a suite of seismic event emissions from each mine location. We compare the estimates of the stress release from each study location with theoretical estimates of the stress release corresponding to constant stress drop (or self-similar) seismic events, events with stress drop that scale independently of seismic moment. We investigate whether the seismic events, associated with the two underground mining operations, obey or violate constant stress drop scaling. If the mining induced events do violate constant stress drop scaling, it would offer the chance to determine whether a temporal (or time-dependent) relationship exists between the stress drop of the seismic events and the roof falls that follow (i.e. whether the stress drops of the seismic events increase, decrease or show no systematic trend through time leading up to a roof fall). We also compare our results with those from previous studies within the moment magnitude range -4 < M_W < 4 [Abercrombie (1995); Boatwright *et al.* (1991), Gibowicz *et al.* (1991); Gibowicz *et al.* (1990); Ide *et al.* (2003); Jost *et al.* (1998), Oye *et al.* (2005) and Yamada *et al.* (2005a, 2005b)].

1.4   Previous Work

Ide and Beroza [2001] is a recent study that has compiled the results from earlier works and suggested that the stress drop, on average, is independent of the seismic moment (i.e. the results indicate constant stress drop scaling is obeyed) when corrected using their methods. On the other hand, Richardson and Jordan [2002] have suggested that the relationship between the stress drop and the seismic moment for the compiled data of the earlier workers do not conform to constant stress drop scaling and have argued that the trends in these data indicate a transition from fracture-dominated events to friction-dominated events. We hypothesize that the results from the *individual* studies, noted above, indicate that the stress release *does* depend on the

seismic moment and that this scaling relationship appears to differ between the various seismogenic environments.

Many studies have reported an apparent breakdown in the earthquake self similarity. This has been attributed to three main effects:

1. **Source effects** [e.g. Aki (1967, 1984, 1987); Archuleta *et al.* (1982); Archuleta (1986); Dietrich (1979, 1986); Fletcher *et al.* (1986); Guo *et al.* (1992); Ida (1973); Papageorgiou and Aki (1983a, 1983b); Richardson and Jordan (2002); Rydelek and Sacks (1989); Sacks and Rydelek (1995)]
2. **Propagation effects** [e.g. Abercrombie and Leary (1993); Abercrombie (1995); Anderson and Hough (1984); Anderson (1986); Frankel and Wennerberg (1989); Hanks (1987); Ide *et al.* (2003); Oye *et al.* (2005)]
3. **Limitations due to finite recording bandwidth** [e.g. Boore (1986); Di Bona and Rovelli (1988); Ide *et al.* (2003); Snoke (1987)]

A goal of this study is to examine and quantify, through theoretical analyses, the extent to which the three categories of effects listed above may affect seismic source scaling relations for our two study areas.

In the following, we briefly summarize the chief results of eight earlier studies. These studies are of particular relevance because they span the range in seismic moment that is of interest to this study. They all take into account propagation effects as well as limitations due to finite recording bandwidth through various approaches. Three of the studies deal specifically with mining related events. Events examined in these eight earlier studies spanned the seismic moment range $5 \cdot 10^3 < M_0 < 2 \cdot 10^{14}$ N·m, which is approximately equivalent to the moment magnitude range $-4 < M_W < 4$. The estimates of the ratio between the radiated seismic energy (E_S) and the static seismic moment (M_0), hereafter referred to as the E_s/M_0 ratio, made by the previous studies before and after correcting for propagation effects and finite recording bandwidth were in the range of $7 \cdot 10^{-8} < E_s/M_0 < 1 \cdot 10^{-3}$. For comparison, the estimates of the E_s/M_0 ratio for the present study before and after correcting for the propagation and bandwidth effects were in the range of $2 \cdot 10^{-8} < E_s/M_0 < 3 \cdot 10^{-6}$. The events in this study spanned the seismic moment range $4 \cdot 10^5 < M_0 < 2 \cdot 10^9$ N·m, which is an equivalent moment magnitude range $-2.2 < M_W < -0.2$.

1. **Abercrombie [1995]** compared the recordings made by surface and borehole sensors from events within a 100 kilometer radius of the 2500-meter deep Cajon Pass Borehole in California. The combination of surface noise and high attenuation in the upper few kilometers of the crust motivated the installment of a sensor down the 2500-meter deep borehole at Cajon Pass. A three-component set of high-temperature 10-Hertz geophones recorded small earthquakes in the vicinity of the San Andreas and San Jacinto Faults at 500 and 10^3 samples per second. The seismic moments of the earthquakes ranged over $10^9 - 10^{16}$ N·m and hypocenters ranged over $5 - 100$ kilometers from the Cajon Pass Borehole. The estimated quality factor for this study was $Q_p \approx 580 - 1400$ and $Q_s \approx 900 - 1300$.

2. **Boatwright *et al.* [1991]** examined aftershocks of the 1989 Loma Prieta earthquake. The aftershocks were recorded at stations located on both soft sediment as well as hard rock sites, at an average hypocentral distance of approximately 100 km. The seismic moments of the aftershocks ranged over $10^{12} - 10^{16}$ N·m. The estimated quality factor for this study was $Q_p \approx 414$ and $Q_s \approx 380$.

3. **Gibowicz *et al.* [1991]** monitored the seismicity associated with excavating a shaft at the Underground Research Laboratory (URL) in Manitoba, Canada. The excavation was done within the Lac du Bonnet granite batholith, where evidence of preexisting fracturing had been found. The events were recorded by a set of three-component accelerometers with a recording sample rate of 10^4 samples per second. In general, the events were located within 5 meters (below and to the side) of the cylindrical shaft as it was excavated at depths between 324 and 443 meters. The distances between the events and the stations varied between 35 and 100 meters. The seismic moments of the seismic events ranged over $10^4 - 10^6$ N·m. The estimated quality factor for this study was $Q \approx 200$, and did not distinguish between P- and S-wave quality factors.

4. **Gibowicz *et al.* [1990]** estimated the source parameters of mine tremors at Heinrich Robert Mine, in the Ruhr Basin of Germany, which were assumed to be associated with either the short term or long term effects of the local underground coal mine operations. The events were recorded by the Bochum University Germany (BUG) network, which consisted of a local array and two remote stations at the mines. The events were recorded by a remote three-component sensor at the Heinrich Robert mine, ~5.0 km from the cluster of events, recording with 100 Hz sampling rate. The seismic moments of the seismic events ranged over $10^{11} - 10^{12}$ N·m. The estimated quality factor in this study was $Q \approx 100 - 200$, and did not distinguish between P- and S-wave quality factors.

5. **Ide *et al.* [2003]** re-examined data collected by Prejean and Ellsworth [2001] from a borehole in the vicinity of the Long Valley Caldera in California. The main data set from Prejean and Ellsworth [2001] was collected from a 2054-meter deep borehole in the vicinity of the caldera. The data were recorded by a three-component sensor (10-Hertz geophone) at three different sampling rates (250, 10^3 and 10^4 samples per second). An additional cluster of five earthquakes was recorded from the same borehole (except 2046 meters deep) using a three-component set of broadband Wilcoxon piezoelectric accelerometers with a recording sample rate of 500 samples per second. The events had hypocenters that were between 2 and 30 kilometers from the Long Valley Exploratory Well (LVEW) borehole and had depths ranging over $3 - 9$ kilometers. The seismic moments of the seismic events ranged over $10^{10} - 10^{13}$ N·m. The estimated quality factor for this study was $Q_p \approx 100 - 2200$ and $Q_s \approx 150 - 4800$, indicating that for some events the estimated Q_s was greater than Q_p. For a small number of events, this study also computed estimates of the stress release after utilizing a Multiple Empirical Green's Function (MEGF) technique to remove the path and site effects from the spectra of a sub-set of their events. We display the results from only the constant Q analysis because the number of events considered under the MEGF approach was too small to provide a sufficient representation.

6. **Jost *et al.* [1998]** investigated the seismicity associated with fluid injection into the KTB Deep Drilling site in Germany. The seismicity occurred when the injection of fluid began to compromise the stability between preexisting fractures within the gneisses and amphibolites at the nine-kilometer injection depth. The KTB borehole was drilled in order to perform hydraulic-fracturing and fluid-injection experiments for the purpose of evaluating the brittle-ductile transition hypothesis in crystalline crust. The seismicity, induced by the injection of fluid, was recorded by a temporary network of 73 surface sensors (1-Hertz geophones recording at 200 samples per second) and an additional three-component sensor (28-Hertz borehole-geophone recording at 10^3 samples per second) down the 3990-meter deep KTB pilot hole. Approximately 400 seismic events were triggered, with locations that ranged between 4000 and 5000 meters from the sensor within the KTB pilot hole. The seismic moments of the seismic events ranged over $10^8 - 10^{10}$ N·m. The estimated quality factor for this study was $Q_p(f) = 420(f)^{0.5}$ and $Q_s(f) = 230(f)^{0.5}$.

7. **Oye *et al.* [2005]** investigated the source-scaling relations for small seismic events by determining the source parameters for events induced by mining operations at the 1400 meter deep Pyhäsalmi ore mine in Finland. The monitoring network at this location consisted of 16 sensors (4.5 Hertz geophones recording with 500, 10^3, and $3 \cdot 10^3$ Hertz sample rates). Source to receiver distances at this location ranged between 60 and 400 meters. The seismic moments of the seismic events ranged over $10^7 - 10^9$ N·m. The estimated quality factor for this study was $Q \approx 350$, and did not distinguish between P- and S-wave quality factors. This study estimated the stress release from spectra that had been corrected using a MEGF technique to remove the path and site effects for collocated events.

8. **Yamada *et al.* [2005a, 2005b]** examined mining induced earthquakes within an underground gold mine in South Africa. The Mponeng Gold Mine operates at over 2500 meters below the surface, where the overburden stress is approximately 70 MPa. The excavation of a gold reef between a basaltic and quartzite formation induced small tremors behind the excavated face. A seismic network of nine, very-high sample-rate ($1.5 \cdot 10^4$ samples per second) three-component accelerometers were installed along a haulage tunnel, which was approximately 50 meters below the excavating operations. The seismic moments of the seismic events ranged over $10^{10} - 10^{11}$ N·m. The estimated quality factor for this study was $Q = 20 - 170$, and did not distinguish between P- and S-wave quality factors.

In this thesis, we discuss and reference only a subset of a large number of studies that have examined problems that are related to the issues examined here. These studies discuss many important issues regarding the assumed source model, treatment of the propagation / recording bandwidth corrections, relationship between the *b*-value and stress drop for a set of seismic events, etc. For this reason we provide the Suggested Reading section, as it contains many additional sources of information that are related to the topics discussed in this thesis but may not have had immediate relevance to the overall objective of this study.

1.5   Outline of Thesis

     This chapter is followed by five chapters containing information regarding the estimation of seismic source parameters (i.e. seismic moment, radiated seismic energy, and stress drop), the assessment of wave propagation effects, the assessment of the limitations imposed by finite recording bandwidth, the application of these methods to real data, and our concluding remarks on constant stress drop scaling in the context of our results and the results from the eight earlier studies. We include four appendices that provide detailed information on important aspects of the analysis approach. A brief summary of the chapters and supporting appendices are provided below:

- **Chapter (2)** deals with a basic theoretical model of the seismic source. The chapter presents and discusses seismic source parameter estimation methods and objective methods of estimating source parameters in the context of two omega-squared models. Details of estimating the integrals of displacement and velocity power spectra are given in **Appendix (1)**. **Appendix (2)** details the method used to correct the integrals of displacement and velocity power spectra for finite recording bandwidth. **Appendix (3)** details the relationship between the apparent stress and Brune stress drop in the context of the Brune [1970, 1971] model.

- **Chapter (3)** assesses the impact of wave propagation effects, recording bandwidth limitations and physical effects at the source upon the estimates of seismic source parameters for theoretical events.

- **Chapters (4) and (5)** apply the analysis methods described in Chapters (2) and (3) to the data from the Moonee Colliery and Springfield Pike Quarry, respectively. **Appendix (4)** details the effect of an uncertain sample rate on estimates of source parameters, which is important in analyzing the Moonee Colliery data.

- **Chapter (6)** summarizes the results of this study and provides concluding remarks on constant stress drop scaling based on the results from this study and the results from eight earlier studies.
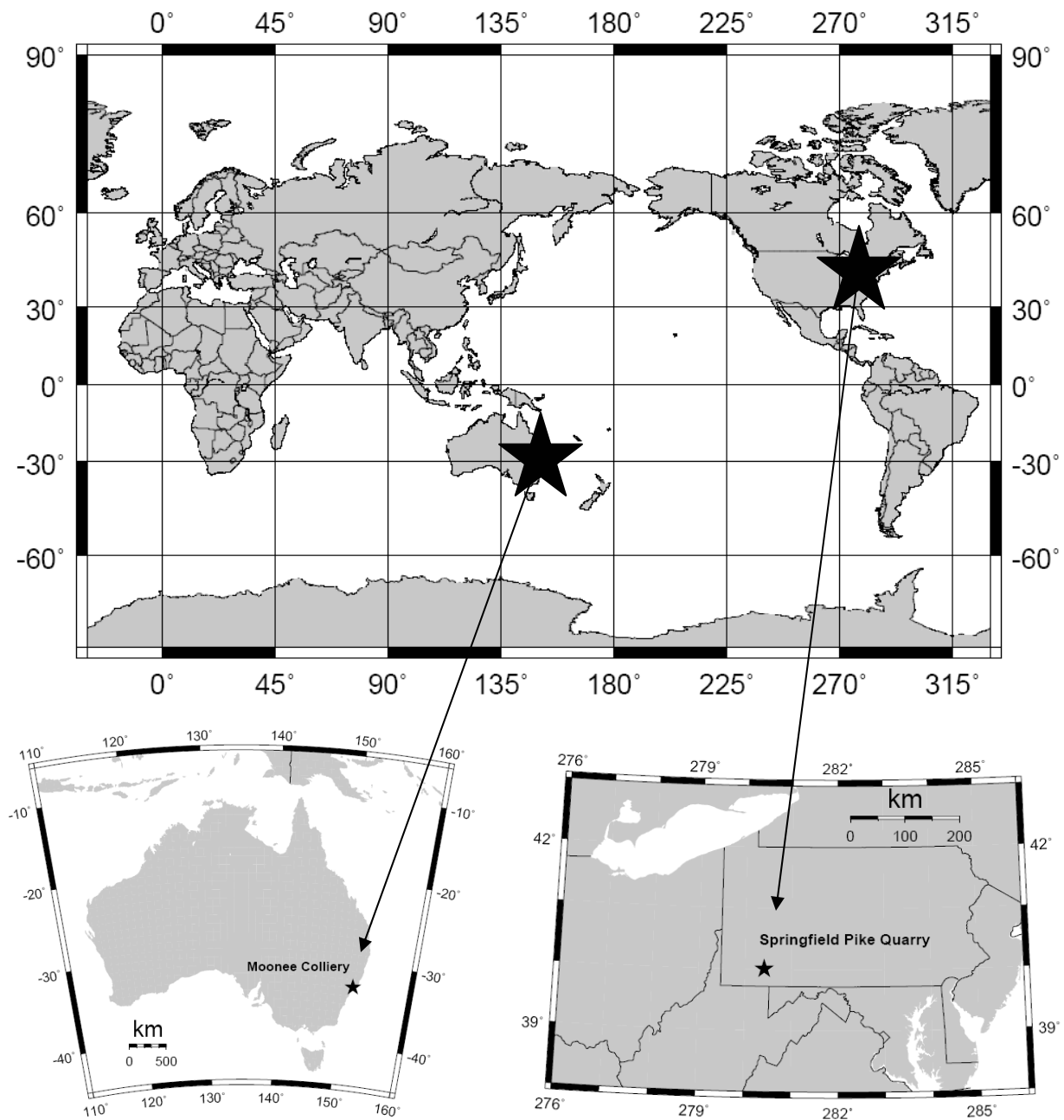
FIGURE 1.1: Locations of the two underground mining operations. The Moonee Colliery is located in New South Wales, Australia. The Springfield Pike Limestone Quarry is located in Southwestern Pennsylvania, United States.

Chapter 2: Seismic Source Parameter Estimates

The seismic source parameters we estimate in this study include the Seismic Moment (M_0), the Radiated Seismic Energy (E_s) and the Apparent Stress (σ_a). We estimate the seismic source parameters under the assumption of the Brune [1970, 1971] model, hereafter the Brune model, for the far-field displacement ground motion.

2.1   The Brune Model

The Brune model for the far-field displacement pulse assumes that the ground motion is caused by a complete effective stress drop across a circular fault during a shear dislocation due to double-couple forces. The far-field displacement pulse shape is proportional to the slip velocity at the source. The model for this pulse shape (shown in Figure 2.1) was also suggested by Ohnaka [1973], and is given by Equation (2.1):

Equation 2.1	$u(t) = \Omega_0 \dfrac{t}{\tau^2} H(t) e^{-t/\tau}$ $$H(t) = \begin{cases} 0 & \text{if } t < 0 \\ 1 & \text{if } t \geq 0 \end{cases}$$

The Brune Model for the Far-field Shear-wave Displacement Pulse Shape
- Ω_0 is the zero-frequency displacement amplitude (m/Hz)
- t is the time (sec)
- τ is the rise time (sec), where $\tau = (2\pi f_c)^{-1}$
- f_c is the source corner frequency (Hz)
- $H(t)$ is the Heaviside function over time

In general, a continuous time domain function, $g(t)$, can be transformed into the frequency domain via the forward Fourier transform of Equation (2.2):

Equation 2.2	$G(f) = \displaystyle\int_{-\infty}^{+\infty} g(t) \cdot e^{-i2\pi ft} dt$

Equation for Computing the Forward Fourier Transform of a Continuous Time-domain Function
- f is the frequency (Hz)
- The forward Fourier transform may also be defined by changing the sign of the exponential (i.e. Aki and Richards [2002], pg. 609), which for a real function $g(t)$ leads to a complex expression that is simply the complex conjugate of $G(f)$ above.

The Fourier displacement amplitude spectrum in the context of the Brune model (shown in Figure 2.2) is given by Equation (2.3) with displacement fall-off rate $\gamma = 2$ and constant $c^\# = 1$. The constant $c^\#$ affects the "sharpness" of the corner made by the amplitudes in the vicinity of the corner frequency (f_c), where larger values of $c^\#$ lead to "sharper" corners.

Equation 2.3	$$\|U(f)\| = \sqrt{U(f)[U(f)]^*} = \frac{\Omega_0}{\left(1 + (f/f_c)^{\gamma c^\#}\right)^{1/c^\#}}$$

General Equation for Modeling Source Spectra, after Abercrombie [1995]
- $U(f)$ is the Fourier displacement amplitude (m/Hz)
- * denotes complex conjugate
- γ is the high frequency fall off rate on log-log (dimensionless)
- $c^\#$ is a constant that affects the "sharpness" of the corner (dimensionless)
- Model parameters for the Brune [1970, 1971] source spectral shape
  - $\gamma = 2$ and $c^\# = 1$

2.2   The Static (or Scalar) Seismic Moment

The static seismic moment (M_0), hereafter the seismic moment, is a representation of the body forces associated with a shear dislocation (fault slip event). The seismic moment is expressed in Equation (2.4), after Keilis-Borok [1959], as the product between the shear modulus (μ), average slip ($\bar{u}$) and fault slip area (A).

Equation 2.4	$$M_0 = \mu A \bar{u}$$

Equation for Physically Estimating the Static (or Scalar) Seismic Moment
- μ is the modulus of rigidity, or shear modulus, of a material and is a measure of the resistance to shearing of the material (N / m^2 or Pa)
- A is the area of shear rupture (m^2)
- $\bar{u}$ is the seismic slip spatially averaged over the rupture area (m)

The average slip can only be estimated directly from earthquakes with faults that have expressions at the surface, where the amount of slip can be inferred from the relative displacement of objects on either side of an exposed fault. The total rupture area can be approximated by relocating the hypocenters of aftershocks after an earthquake, assuming that these events represent the process of equilibrating the original faulted area. Except for large events, where these features may potentially be observed, it is often impossible to *quantitatively* estimate the area of rupture or the average amount of displacement caused by an earthquake. Keilis-Borok [1960] identified that the seismic moment is proportional to Ω_0, the zero-frequency

displacement amplitude (i.e. the amplitude in the long-period limit of the Fourier displacement amplitude spectrum) corrected for the geometrical spreading factor (R). After Keilis-Borok [1960], the seismic moment can be estimated from the Fourier amplitude spectrum of the displacement ground motion using Equation (2.5). For far-field ground motion that is recorded in three mutually orthogonal directions, the zero-frequency displacement amplitude is estimated by computing the L^2-norm (or vector norm) of the three low-frequency estimates from each individual component.

Equation 2.5	$$M_0 = \frac{4\pi\rho\upsilon^3 R\sqrt{\Omega_0(Z)^2 + \Omega_0(H_1)^2 + \Omega_0(H_2)^2}}{\mathcal{R}_{\phi\theta}}$$

Source Parameters Seismic Moment (M_0) after Keilis-Borok [1960]
- ρ is the density (kg/m^3)
- υ is the P-wave velocity (α) or S-wave velocity (β) in (m/s)
- R is the Geometrical Spreading Factor and taken here to be the source-receiver distance
- Ω_0(comp) is the zero-frequency displacement amplitude for a single component (m/Hz)
- $\mathcal{R}_{\phi\theta}$ is the far-field the radiation pattern value (dimensionless)
- $<\mathcal{R}_{\phi\theta}>$ is the Root-Mean-Squared (RMS) P- or S-wave radiation pattern value
  Focal Mechanisms are unknown for this study, therefore we assume $\mathcal{R}_{\phi\theta} = <\mathcal{R}_{\phi\theta}>$
  - $<\mathcal{R}_{\phi\theta}> = 2/\sqrt{15}$ P-wave (after Aki and Richards [2002], pg. 115)
  - $<\mathcal{R}_{\phi\theta}> = \sqrt{(2/5)}$ S-wave (after Aki and Richards [2002], pg. 115)

2.3   The Brune Stress Drop

The stress drop in the context of the Brune model, hereafter the Brune Stress Drop (σ_B), is based on the Static Stress Drop ($\Delta\sigma$), after Eshelby [1957] and Keilis-Borok [1959], where the static stress drop represents the difference between the initial stress (σ_0) prior to faulting and the final stress (σ_1) following rupture. The static stress drop ($\Delta\sigma$), the seismic moment (M_0), and the radius of a circular rupture (r) are related, in the context of a circular dislocation, through Equation (2.6):

Equation 2.6	$$\Delta\sigma = \sigma_0 - \sigma_1 = \frac{7\pi}{16r}\mu\bar{u} = \frac{7\pi}{16r}\frac{M_0}{A} = \frac{7 \cdot M_0}{16}\left(\frac{1}{r}\right)^3$$

Static Stress Drop ($\Delta\sigma$) for a Circular Fault after Keilis-Borok [1959]
- σ_0 is the initial shear stress before rupture (N / m^2 or Pa)
- σ_1 is the final shear stress after rupture (N / m^2 or Pa)
- r is the radius of the circular rupture (m), where the area (A) of shear rupture is assumed to equal πr^2 (m^2)

Brune [1970, 1971] put forth a relationship between the radius of a circular fault and the corner frequency by comparing the relationship between the far-field shear-wave radiation for a double-couple event, after Keilis-Borok [1960], and the average far-field shear-wave radiation spectrum in the long-period limit of the Fourier displacement amplitude spectrum. In the context of the Brune model, the radius of an instantaneous circular fault rupture is related to the corner frequency of the far-field shear wave amplitude spectrum through Equation (2.7):

Equation 2.7	$$r = \left(\frac{\beta}{2\pi f_c}\right)\sqrt{\frac{7\pi}{4}}F \cong \left(\frac{\beta}{2\pi f_c}\right)\sqrt{\frac{7\pi}{4}}$$

Equation for the Radius of a Circular Fault, after Brune [1970, 1971]
- F is a factor related to another factor (S) by the expression $F = \sqrt{S/0.8}$, where (S) is a factor that accounts for the conversion of S-waves to P-waves. Brune [1970, 1971] stated that the factor (F) is sufficiently approximated by unity, which requires the factor (S) to equal 0.8.

Equations (2.6) and (2.7) lead to the expression in Equation (2.8), which relates the Brune stress drop, the seismic moment and the corner frequency in the context of the Brune model:

Equation 2.8	$$\sigma_B = \left(\frac{7 \cdot M_0}{16}\right)\left(\frac{2\pi f_c}{\beta\sqrt{7\pi/4}}\right)^3$$

Brune Stress Drop for a Circular Fault, after Brune [1970, 1971]

The model introduced by Brune [1970, 1971] was developed specifically for the ground motion associated with shear waves. Brune [1970, 1971] constrained the relationship between the corner frequency and the radius of the circular crack by assuming the final stress was equal to the frictional stress (i.e. overshoot equals zero in Equation 2.28). Boatwright [1984] notes that the Brune [1970, 1971] relation between the corner frequency and the radius of the circular crack must be *exact* in order to interpret the Brune stress drop as the average static stress drop. Brune [1971] corrected equations corresponding to the approximate solution to the near-field displacement and to the expression involving the final dislocation associated with the stress drop, which were incorrect in Brune [1970]. In this study, we do not explicitly measure the Brune stress drop. Our assumption of the Brune model and our estimation techniques results in estimates of the Brune stress drop that is not independent from the apparent stress (discussed in Section 2.7). Appendix (4) shows that, under the assumed model and estimation techniques, estimates for the Brune stress drop are equal to ~4.3 times the apparent stress.

2.4   The Radiated Seismic Energy

The radiated seismic energy (E_s) represents the fraction of the total strain energy (E) released during the dislocation of a fault. Wyss and Brune [1968] introduced the total strain energy in terms of the average stress ($\overline{\sigma}$), averaged between the initial stress (σ_0) and the final stress (σ_1), acting during the dislocation of a fault with rupture area (A) over an average slip length ($\bar{u}$) and is given by Equation (2.9):

Equation 2.9	$$E = \frac{\sigma_0 + \sigma_1}{2} A\bar{u} = \overline{\sigma}A\bar{u} = \frac{\overline{\sigma}}{\mu} M_0$$
Total Strain Energy after Wyss and Brune [1968] • $\overline{\sigma}$ is the average between the initial and final shear stress (N / m^2 or Pa)	

The total strain energy released during shear dislocation is dissipated during slip through work done by the frictional forces acting within the fault (E_F) irreversibly transforming kinetic energy into thermal energy, by the loss of energy required to create new crack surfaces during rupture propagation (E_C), and by the loss of energy in generating seismic radiation (E_S) [e.g. Magariaga (1976, 1977); Andrews (1980), and Snoke *et al.* (1983)]. The total strain energy released during the dislocation of a fault can be re-written in terms of the three main sources of energy dissipation noted above. The energy balance for the total strain energy released during dislocation is given by Equation (2.10):

Equation 2.10	$$E = E_F + E_C + E_S$$
Energy Balance for Total Strain Energy Released • E is the total strain energy • E_F is the thermal energy created due to work done by frictional forces (J) • E_C is the energy lost in creating new crack surfaces during rupture propagation (J) • E_S is the energy lost in generating seismic radiation (J)	

The seismic efficiency factor (η), introduced by Wyss and Brune [1968], relates the fraction of the total strain energy released as seismic radiation (given by Equation 2.11):

Equation 2.11	$$E_S = \eta E = E - \left(E_F + E_C \right)$$
Relationship between the Radiated Seismic Energy (E_s), Total Elastic Energy (E) and Seismic Efficiency Factor (η) • η is the seismic efficiency factor (dimensionless)	

One can only fully quantify the radiated seismic energy in terms of the total elastic energy and the seismic efficiency factor in the laboratory environment where the total strain energy released and lost due to frictional heating and fracturing can be measured [e.g. Dieterich (1981); Lockner and Okubo (1983); McGarr (1999)]. Prior to the year 1980, the estimates of the radiated seismic energy were based on empirical relationships as a function of magnitude (i.e. the Gutenberg and Richter [1956] magnitude and energy relationships). The work of Boatwright [1980] and Snoke *et al.* [1983] were the first studies to take advantage of the fact that the body-wave contribution to the total radiated seismic energy is proportional to the integral of the square of the ground velocity. Following Boatwright and Fletcher [1984], the radiated seismic energy can then be estimated using Equation (2.12):

Equation 2.12	$$E_s = \frac{4\pi\rho\upsilon R^2 \left\langle \mathcal{R}_{\phi\theta} \right\rangle^2}{\mathcal{R}_{\phi\theta}{}^2} \left[I_{V^2}(Z) + I_{V^2}(H_1) + I_{V^2}(H_2) \right]$$
Radiated Seismic Energy (E_s) after Boatwright and Fletcher [1984] • $I_{V^2}(comp)$ is the Integral of the square of the ground velocity for a single component (m^2/s^2)	

2.5 Integrals of the Square of the Ground Motion

Andrews [1986] and Snoke [1987] noted that calculation of the Brune stress drop requires the estimates of two spectral observables, Ω_0 and f_c. They also noted that errors in estimating the corner frequency leads to errors in estimating σ_B (of Equation 2.8) that are proportional to the errors in estimating the corner frequency, cubed. Andrews [1986] introduced a method for objectively determining Ω_0 and f_c by developing relationships between the integrals of the square of the ground motion. Snoke [1987] introduced a similar method for objectively determining f_c by developing a relationship between the integral of the square of the ground velocity and Ω_0, which was found by Snoke [1987] to offer more stable estimates of f_c than the

parameterizations offered by Andrews [1986]. Snoke [1987] explained that the fractional variance in σ_B is significantly less if the integral of the square of the ground velocity replaces f_c as the spectral observable, which explains why patterns in stress drop are apparent unless measures of stress drop are used that does not depend on the corner frequency directly [Snoke *et al.*, 1983]. In the context of Andrews' [1986] parameterizations, the integral of the square of the ground motion can be computed in either the time domain or in the frequency domain by Parseval's Relation (Equation 2.13):

Equation 2.13	$I_{M^2} = \int\limits_{-\infty}^{+\infty} [m(t)]^2\, dt = \int\limits_{-\infty}^{+\infty} M(f)[M(f)]^*\, df = 2 \cdot \int\limits_{0}^{+\infty} M(f)[M(f)]^*\, df$

Parseval's Relation for Continuous Data
- I_{M^2} is the integral of the square of the ground motion
- $m(t)$ is the ground motion amplitude in the time domain (real)
- $M(f)$ is the ground motion amplitude in the frequency domain (complex)
- * denotes the complex conjugate, where we use the fact that $M(f) = [M(-f)]^*$ when $m(t)$ is real.

In this study, the integral of the square of the ground motion is computed in the frequency domain for the following reasons:

- We wish to compute the integral of the square of the ground motion assuming the Brune model and one additional source model. With the exception of the Brune model, the analytic representation of the additional source model is only available in the frequency domain (i.e. the time domain pulse for the source model is not physically significant).

- Correction of the recorded data to account for the limitations imposed by finite bandwidth necessitates analysis in the frequency domain.

- Correction of the recorded data for instrument response, correction of the recorded data for the propagation effects (i.e. anelastic attenuation, intrinsic scattering and geometrical spreading), and computation of derivatives are much more readily accomplished in the frequency domain.

- In addition, Andrews [1986] and Snoke [1987] point out that the calculation of the Brune stress drop requires the estimates of spectral observables that, in the context of the methods outlined by Snoke [1987], necessitate analysis in the frequency domain.

The data are transformed into the frequency domain by computing the forward Fourier transform of the data in the time domain using Equation (2.14):

Equation 2.14	$(a)\ \ G(f)=\int_{-\infty}^{+\infty}g(t)\cdot e^{-i2\pi ft}dt$ $(b)\ \ G(v\cdot\Delta f)=\Delta t\cdot\sum_{\theta=0}^{N-1}g(\theta\cdot\Delta t)\cdot e^{\frac{-i2\pi v\theta}{N}}$

Equation for Computing the Forward Fourier Transform of a Time-series
- (a) Continuous Data
- (b) Discrete Data
    - N is the number of sampled points in the time domain
    - θ is the discrete time sample (where $\theta \cdot \Delta t = t$)
        - Δt is the time interval and is equal to (Sample Rate)$^{-1}$
    - v is the discrete frequency sample (where $v \cdot \Delta f = f$)
        - Δf is the frequency interval and is equal to $(N \cdot \Delta t)^{-1}$
    - The highest recoverable frequency is equal to the Nyquist Frequency
        - Nyquist = (Sample Rate)/2

Estimation of the radiated seismic energy, the seismic moment, and the stress drop involves the correction of observed data for the effects of the propagation path and instrument limitations. The following sections describe the approach taken in this study to accomplish this objective.

2.5.1   Corrections for Propagation Effects

A general equation describing the energy loss due to anelastic attenuation and intrinsic scattering between the source and the receiver, after Anderson and Hough [1984] and Boatwright *et al.* [1991], can be written as Equation (2.15):

Equation 2.15	$$E_L(f,T^\star)=e^{\pi f T^*}=e^{\pi f\left(t^*+T\!/\!Q\right)}$$

General Equation for Accounting for Energy Loss due to
Wave Propagation Effects, after Anderson and Hough [1984] and
Boatwright *et al.* [1991]
- T^* represents the combination of the near-receiver attenuation and scattering (t^*) as well as the distance dependent attenuation and scattering (T/Q)
    - t^* represents the near-receiver attenuation and scattering, averaged over all recordings (sec)
    - T is the travel time (R / v) of the wave under consideration (sec)
    - Q is the frequency independent quality factor (unitless)

The product between the Fourier amplitude, $M(f)$, and $E_L(f, T^*)$ is computed at each frequency. By considering the hypocentral distance and the average wave-velocity between source and receiver constant, the appropriate estimate of the energy lost over the whole propagation path, in terms of T^*, may be obtained iteratively by choosing the value for the quality factor (Q) that results in the smallest misfit between the observed high-frequency displacement amplitude fall-off rate of the data and the theoretical fall-off rate of a Brune model. The Fourier amplitude spectra are assumed to be corrected for the energy lost during propagation after identifying the appropriate value of T^* that adjusts the high-frequency fall-off rate to conform to the Brune model.

2.5.2   Corrections for Finite Bandwidth

Snoke [1987] points out that in order to obtain an appropriate measure of the integral of the square of the ground motion, the power spectra must be assessed in order to determine where noise effects or signal processing effects have contaminated or limited the seismic event signal. Snoke [1987] explained that these effects often lead to underestimates of the integral of the square of the ground motion unless appropriately accounted for. As discussed below, Snoke [1987] developed correction factors to account for the contaminated and the bandlimited amplitudes in order to constrain better estimates of the integrals of the square of the ground motion.

Limitations in bandwidth arise due to the finite number of recorded samples (N), finite sample rate (Δt), noise contamination, and propagation effects [e.g. $f_{\max}$ after Hanks (1982)], etc. The number of recorded samples and the sample rate immediately constrain the observed frequency range between zero and the Nyquist frequency ($[2 \cdot \Delta t]^{-1}$), hereafter the bandlimited frequency range. Poor constraint on the low-frequency amplitudes and severe propagation effects observed in the high-frequency amplitudes, such as $f_{\max}$, often require the selection of a window within the bandlimited frequency range between frequency samples (v_1) and (v_2), such that $0 \leq v_1 \cdot \Delta f < v_2 \cdot \Delta f \leq (2 \cdot \Delta t)^{-1}$.

The first step in correcting the observed data involves estimation of the pre-signal background noise level in the frequency domain. A signal/noise amplitude ratio of at least 5 is used throughout this study. If this criterion is not met, the minimum and maximum frequency limits of the spectral data ($v_1 \cdot \Delta f$ and $v_2 \cdot \Delta f$, respectively) are adjusted.

We estimate, to a first approximation, the zero-frequency displacement amplitude by calculating the geometric mean of the displacement spectral amplitudes in a window between $v_1 \cdot \Delta f$ and $v_\Omega \cdot \Delta f$, where (v_Ω) represents the frequency sample of the displacement amplitude *before* the beginning of the high-frequency fall-off. In a similar manner, we estimate the zero-period (or infinite-frequency) acceleration amplitude (Ψ_0) by calculating the geometric mean of the acceleration spectral amplitudes (corrected for T^*) in a window between $v_\Psi \cdot \Delta f$ and $v_2 \cdot \Delta f$, where (v_Ψ) represents the frequency sample of the acceleration amplitude *after* the end of the low-frequency rise. In the context of the Brune model, the zero-period acceleration amplitude is equivalent to $\Omega_0 \cdot (2\pi f_c)^2$. However, at this point in the analysis the corner frequency has yet to be determined. Estimation of Ψ_0 is needed under circumstances where the high-frequency amplitudes of ground motion are not well enough constrained (i.e. in comparison to the Brune model) to select a single amplitude to base the high-frequency correction factor offered by Snoke

[1987]. This is especially the case in the underground mining environment where the noise generated during mining operations significantly affect the high frequency content of ground motion. For this reason, calculating the zero-period acceleration amplitude should provide a better constraint on the estimate of the correction factor for the high-frequency amplitudes of the ground motion power spectra.

The Hanks and Thatcher [1972] source model, hereafter the Hanks and Thatcher model, represents a convenient approximation to the Fourier amplitude spectrum of the Brune model using straight lines (when plotted log amplitude versus log frequency), shown in Equation (2.16) and illustrated in Figure (2.2). The equivalent expression for the acceleration spectra in terms of the zero-period acceleration amplitude is shown in Equation (2.17)

Equation 2.16	$$\left|U(f)\right| = \sqrt{U(f)[U(f)]^*} = \begin{cases} \Omega_0 & \text{if } f \leq f_c \\ \Omega_0 \left(\dfrac{f_c}{f}\right)^2 & \text{if } f > f_c \end{cases}$$
The Hanks and Thatcher [1972] approximation of the Brune [1970, 1971] model	

Equation 2.17	$$\left|\ddot{U}(f)\right| = \sqrt{\ddot{U}(f)\left[\ddot{U}(f)\right]^*} = \begin{cases} \Psi_0 \left(\dfrac{f}{f_c}\right)^2 & \text{if } f \leq f_c \\ \Psi_0 & \text{if } f > f_c \end{cases}$$
The Hanks and Thatcher [1972] model in terms of the Zero-Period Acceleration Amplitude (Ψ_0)	

Regardless of the actual omega-squared source model responsible for the observed data, our estimates of the bandwidth correction factors for the integrals of the velocity and displacement power spectra are determined by assuming that the amplitude spectra under ideal recording conditions would essentially correspond to the Hanks and Thatcher model for frequencies less than and greater than $v_1 \cdot \Delta f$ and $v_2 \cdot \Delta f$, respectively. For discrete data in the frequency domain that have been corrected for T^*, the integrals of the square of the ground velocity and of the square of the ground displacement become Equation (2.18) and Equation (2.19), respectively.

Equation 2.18	$I_{V^2} = \dfrac{8}{3}\pi^2(\Omega_0)^2(v_1 \cdot \Delta f)^3 + 2\Delta f \cdot \sum_{v=v_1}^{v_2}\dot{U}(v \cdot \Delta f)\left[\dot{U}(v \cdot \Delta f)\right]^* + \dfrac{(\Psi_0)^2}{2\pi^2(v_2 \cdot \Delta f)}$
	Integral I_{V^2} of the Velocity-Squared (Power) Spectra after Snoke [1987] Ω_0 is the zero-frequency displacement amplitude (m/Hz) Ψ_0 is the zero-period acceleration amplitude (m/s^2 / Hz) v_1 and v_2 are the low- and high-frequency sample point bandwidth limits Δf is the frequency interval (Hz) - The correction factors assume the Hanks and Thatcher model and contribute to the lack of low frequency and high frequency bandwidth outside of the integration limits v_1 and v_2.

Equation 2.19	$I_{D^2} = \dfrac{2}{3}(\Omega_0)^2(v_1 \cdot \Delta f) + 2\Delta f \cdot \sum_{v=v_1}^{v_2}U(v \cdot \Delta f)[U(v \cdot \Delta f)]^* + \dfrac{(\Psi_0)^2}{24\pi^4(v_2 \cdot \Delta f)^3}$
	Integral I_{D^2} of the Displacement-Squared (Power) Spectra after Snoke [1987]

The correction factors for the low-frequency spectral amplitudes have already been given by Snoke [1987]. The only things novel here are the correction factors for the high-frequency spectral amplitudes, which have applications for spectra with high-frequency amplitudes that are not well constrained. Appendix (2) contains the derivation of the correction terms in Equations (2.18) and (2.19) for the limitations imposed by finite bandwidth.

2.5.3   Integrals of Displacement and Velocity Power Spectra

In this section we compute the integrals of the square of the ground motion assuming the Brune model and the Hanks and Thatcher model. The Hanks and Thatcher model essentially represents the Brune model when $c^{\#}$ approaches infinity and $\gamma = 2$ in Equation (2.3). As shown below in Section (2.6), objective estimates of seismic source parameters through relationships between the integrals of the square of ground motion depend on the assumed source model. Since real ground motion spectra do not conform perfectly to any theoretical model, there is a need to assess the sensitivity of the integral estimation approach to the assumed source model. An important note here is that the Hanks and Thatcher model is not used in this section to describe a physically realizable source model. Instead, it is used, with the Brune model, to assess the sensitivity of the estimates of the integrals of the power spectra in addition to the sensitivity of the parameterizations in the context of Andrews [1986].

Equations (2.20) through (2.21) summarize the expressions of the integrals of the displacement and the velocity power spectra assuming ideal conditions (unlimited bandwidth and no propagation effects) for the Brune model and the Hanks and Thatcher model, respectively.

Equation 2.20	$I_{V^2} = 2\pi^3 (\Omega_0)^2 (f_c)^3 \approx 62.013 \cdot (\Omega_0)^2 (f_c)^3$ $I_{D^2} = \dfrac{\pi (\Omega_0)^2 (f_c)}{2} \approx 1.571 \cdot (\Omega_0)^2 (f_c)$
Integrals of the Displacement and Velocity Power Spectra assuming the Brune Model	

Equation 2.21	$I_{V^2} = \dfrac{32}{3}\pi^2 (\Omega_0)^2 (f_c)^3 \approx 105.276 \cdot (\Omega_0)^2 (f_c)^3$ $I_{D^2} = \dfrac{8}{3}(\Omega_0)^2 (f_c) \approx 2.667 \cdot (\Omega_0)^2 (f_c)$
Integrals of the Displacement and Velocity Power Spectra assuming the Hanks and Thatcher Model	

The integral result of the square of the ground motion assuming the Brune model (Equation 2.20) has already been given by Andrews [1986]. Appendix (1) contains a derivation of the results from each integral of squared ground motion in Equation (2.20).

2.6 Objective Estimation of the Zero-Frequency Displacement Amplitude and Corner Frequency

Andrews [1986] offered parameterizations of the integrals of the displacement and velocity power spectra, assuming the Brune model, for the purpose of objectively estimating the zero-frequency displacement amplitude and the corner frequency. Snoke [1987] chose to estimate the zero-frequency displacement amplitude by computing the geometrical mean of a window of low-frequency amplitudes, similar to the approach described in the above section. Snoke [1987] observed that more stable estimates of the corner frequency could be obtained through a parameterization of the integral of the square of the ground velocity, assuming the Brune model, and the independently estimated zero-frequency displacement amplitude [as opposed to the approach offered by Andrews (1986)]. In the current section, we present the parameterization for the Brune model offered by Andrews [1986], as well as a similar parameterization for the Hanks and Thatcher spectral model. We also offer a possible explanation for the instability observed by Snoke [1987] when using the estimation approaches offered by Andrews [1986].

Equations (2.20) and (2.21) demonstrate that the integrals of power spectra share a common form, given by Equation (2.22):

$$
\begin{array}{|c|c|}
\hline
\begin{array}{c} \text{Equation} \\ 2.22 \end{array} &
\begin{aligned}
I_{V^2} &= A \cdot \left(\Omega_0\right)^2 \left(f_c\right)^3 \\
I_{D^2} &= B \cdot \left(\Omega_0\right)^2 \left(f_c\right)
\end{aligned} \\
\hline
\end{array}
$$

The General Form of the Integrals of the Displacement and Velocity Power Spectra
- A is a constant depending on the assumed velocity-squared model
- B is a constant depending on the assumed displacement-squared model

The integrals of the velocity and displacement power spectra will follow Equation (2.22) for any model derived from Equation (2.3) for a high-frequency displacement-amplitude fall-off rate $\gamma \geq 2$ and a "sharpness" constant $c^{\#} \geq 1$. For source spectra wherein the form shown by Equation (2.22) holds, the zero frequency displacement amplitude and corner frequency can be parameterized in terms of the integrals of the power spectra following Equation (2.23).

$$
\begin{array}{|c|c|}
\hline
\begin{array}{c} \text{Equation} \\ 2.23 \end{array} &
\Omega_0 = \sqrt[4]{\frac{A}{B^3}} \cdot \sqrt[4]{\frac{\left(I_{D^2}\right)^3}{\left(I_{V^2}\right)}} \qquad\qquad
f_c = \sqrt{\frac{B}{A}} \cdot \sqrt{\frac{\left(I_{V^2}\right)}{\left(I_{D^2}\right)}} \\
\hline
\end{array}
$$

The General Form of the Parameterization of Ω_0 and f_c
- A is a constant depending on the assumed velocity-squared model
- B is a constant depending on the assumed displacement-squared model

Equations (2.24) and (2.25) give the theoretical estimates of the zero-frequency displacement amplitude and the corner frequency for each of the two source models considered, under ideal circumstances (infinite data bandwidth and no propagation effects).

$$
\begin{array}{|c|c|}
\hline
\begin{array}{c} \text{Equation} \\ 2.24 \end{array} &
\begin{aligned}
\Omega_0 &= \sqrt[4]{16} \cdot \sqrt[4]{\frac{\left(I_{D^2}\right)^3}{\left(I_{V^2}\right)}} = 2.000 \cdot \sqrt[4]{\frac{\left(I_{D^2}\right)^3}{\left(I_{V^2}\right)}} \\
f_c &= \frac{1}{2\pi} \cdot \sqrt{\frac{\left(I_{V^2}\right)}{\left(I_{D^2}\right)}} \approx 0.159 \cdot \sqrt{\frac{\left(I_{V^2}\right)}{\left(I_{D^2}\right)}}
\end{aligned} \\
\hline
\end{array}
$$

Parameterization of Ω_0 and f_c assuming the Brune Model

Equation 2.25	$\Omega_0 = \sqrt[4]{\dfrac{9\pi^2}{16}} \cdot \sqrt[4]{\dfrac{\left(I_{D^2}\right)^3}{\left(I_{V^2}\right)}} \approx 1.535 \cdot \sqrt[4]{\dfrac{\left(I_{D^2}\right)^3}{\left(I_{V^2}\right)}}$
	$f_c = \dfrac{1}{2\pi} \cdot \sqrt{\dfrac{\left(I_{V^2}\right)}{\left(I_{D^2}\right)}} \approx 0.159 \cdot \sqrt{\dfrac{\left(I_{V^2}\right)}{\left(I_{D^2}\right)}}$
Parameterization of Ω_0 and f_c assuming the Hanks and Thatcher Model	

The parameterizations offered by Andrews [1986] and Snoke [1987] assume the Brune model. It turns out that the parameterization of the corner frequency in terms of the integrals of the power spectra are the same regardless of the choice of the omega-squared Fourier displacement amplitude models presented in this study. However it can be shown that this consistency in the estimate of the corner frequency breaks down for models with high-frequency displacement amplitude spectral slopes greater than omega-squared (e.g. omega-cubed).

Snoke [1987] determined that the parameterizations offered by Andrews [1986] could lead to inconsistent estimates of the spectral parameters. Snoke [1987] considered synthetic tests on theoretical spectra with variable fall-off rates and found that the parameterizations offered by Andrews [1986] did not typically provide stable estimates. The lack of consistency or stability observed by Snoke [1987] is a result of the fact that the parameterization of the zero-frequency displacement amplitude and the corner frequency is dependent upon the choice of model and fall-off rate. We find that assessing the misfit between the assumed model and the observed Fourier amplitude spectra (both in shape and in high-frequency fall-off rate) should in principle be performed whenever one is using the integral approach to estimation of the zero-frequency displacement amplitude and corner frequency. This should be done in order to avoid estimating spectral parameters that are inconsistent with what a typical observer would pick. However, as explained in Chapters (4) and (5), the quality of data used in this study is such that any appreciable gains in finding the best fit source model are insignificant in comparison with the errors associated with the recording procedure. We therefore assume the Brune model for all computation.

2.7 The Apparent Stress

Wyss and Brune [1968] introduced the apparent stress, at least in concept, through the product between the average acting stress and the seismic efficiency factor (Equations 2.9 and 2.11 above). The apparent stress differs from the Brune stress drop because its measurement does not require the assumption of a specific model. The Brune stress drop assumes that the far-field shear-wave radiation is consistent with the Brune model, which requires that $\gamma = 2$ and $c^{\#} = 1$, in the context of Equation (2.3). Therefore, if the source of recorded events were pure implosions, the estimates of the Brune stress drop would theoretically be meaningless and would potentially

lead to estimates that may not be conducive to comparing the events in a relative sense. Apparent stress, on the other hand, is not a measure that requires specific assumptions and leads to estimates that are much more objective and potentially more reliable when comparing several events in a relative sense. However, *interpretation* of the apparent stress does require the assumption of a specific source model.

Multiplying the expression in Equation (2.9) through by the modulus of rigidity and the seismic efficiency factor and dividing through by the seismic moment yields Equation (2.26), which are all equivalent expressions for the apparent stress in the context of a shear dislocation.

Equation 2.26	$$\sigma_a = \eta\overline{\sigma} = \mu\frac{\eta E}{M_0} = \mu\frac{E_s}{M_0}$$
The Apparent Stress after Wyss and Brune [1968]	

The average shear stress, the seismic efficiency factor and the total strain energy are typically unknown or not well constrained for most seismic events, except in the laboratory environment [e.g. McGarr (1999)]. For this reason, the apparent stress is most commonly measured based on the product between the modulus of rigidity and the estimate of the E_s/M_0 ratio. As discussed in Section (2.4), the estimates of the radiated seismic energy, prior to the year 1980, were based on the empirical relationships as a function of magnitude (i.e. the Gutenberg and Richter [1956] magnitude and energy relationships) and led to extremely uncertain estimates of the apparent stress. However, the work of Boatwright [1980] and Snoke *et al.* [1983] led to much better constrained estimates of the apparent stress by computing the radiated seismic energy from the total energy flux directly from the body-waves, via the integration of the velocity-squared amplitudes in either the time domain or the frequency domain.

In the laboratory environment, the level of shear stress before and after slip are known quantities, as well as the frictional stress (σ_F) opposing motion [McGarr (1999)]. Multiplying Equation (2.11) by the ratio between the modulus of rigidity and the seismic moment yields Equation (2.27).

Equation 2.27	$$\sigma_a = \mu\frac{E_S}{M_0} = \mu\frac{E}{M_0} - \mu\frac{(E_F + E_C)}{M_0} = \overline{\sigma} - \sigma_F$$
Laboratory Estimates of the Apparent Stress after McGarr [1999] • σ_F is the frictional shear stress (N / m^2 or Pa)	

The estimate of the apparent stress for a seismogenic event associated with a shear dislocation can be interpreted as either one of two equivalent statements:

1. The fractional amount of the average acting stress that is consumed during the generation of seismic radiation
2. The difference between the average acting stress and the frictional stress resisting motion throughout the event duration

Snoke [1987] points out that if one were to assume that the P-wave contribution to the total radiated seismic energy is negligible and that the integrals of the power spectra have negligible angular dependence, then using the methods described by Andrews [1986] or Snoke [1987] will result in a constant value for the ratio between the apparent stress and the Brune stress drop. In the context of the Brune model, the ratio between the apparent stress and the Brune stress drop (σ_a/σ_B), which has already been shown by both Andrews [1986] and Snoke [1987], is a constant value of 0.2345, or $\sigma_B/\sigma_a = 4.265$ (see Appendix 4 for a derivation).

An additional note on the relationship between the apparent stress and Brune stress drop concerns the amount of over-shoot (Equation 2.28):

Equation 2.28	$$OS = \dfrac{\Delta\sigma - \sigma_D}{\Delta\sigma} = \dfrac{\sigma_F - \sigma_1}{\sigma_0 - \sigma_1}$$
Estimates of Over-Shoot after Savage and Wood [1971] • σ_D is the dynamic stress drop or effective stress (N / m^2 or Pa) ○ $\sigma_D = \sigma_0 - \sigma_F$	

The Brune stress drop assumes that the final shear stress is equal to the frictional shear stress on the fault (i.e. that the average static stress drop is equal to the dynamic stress drop), which leads to no over-shoot (OS = 0). Under this assumption, the expression for the apparent stress becomes Equation (2.29):

Equation 2.29	$$\sigma_a = \dfrac{\sigma_B}{4.265} = \dfrac{\sigma_0 + \sigma_{1,F}}{2} - \sigma_{1,F} = \dfrac{\sigma_0 - \sigma_{1,F}}{2} = \dfrac{\Delta\sigma}{2}$$
Estimates of the Apparent Stress where Final Stress equals Frictional Stress	

We expect to find that the Brune stress drop is equal to the static stress drop under the above assumptions, but instead find that that they are different by a factor of ~2. The fact that we neglect the P-wave energy in this study does not account for this inconsistency, as we assume

that the ratio between the P-wave radiated energy and the S-wave radiated energy is on the order of ~0.1 for a double-couple event. Further investigation is necessary to resolve this ambiguity.

Savage and Wood [1971] argued that if the frictional stress on the fault is greater than or equal to the final stress on the fault (i.e. no under-shoot or no negative over-shoot), then the apparent stress and the static stress drop will conform to the inequality expressed in Equation (2.30).

<table>
<tr>
<td>Equation
2.30</td>
<td>$$\sigma_a = \frac{\Delta\sigma}{2}(1 - 2 \cdot OS_+) \leq \frac{\Delta\sigma}{2}$$</td>
</tr>
<tr>
<td colspan="2">Estimates of the Apparent Stress where Final Stress is less than or equal to the Frictional Stress after Savage and Wood [1971]
• OS_+ is non-negative over-shoot</td>
</tr>
</table>

In the chapters to follow, we use the terms E_s/M_0 ratio and apparent stress interchangeably. In the context of the Brune model and the methods of estimation offered by both Andrews [1986] and Snoke [1987], the estimates for each of these terms are not independent from one another, varying only by a constant. In this thesis, we intend to use the term "E_s / M_0 ratio" when we are comparing the parameters we observe seismically and the terms related to the "apparent stress" or "stress drop" when we are considering the physical implications of our observed seismic parameters. For example, we show plots of only our seismic observables: seismic moment, radiated seismic energy and E_s / M_0 ratio. However, the trends that we *observe* in the E_s / M_0 ratio lead to *interpretations* of those trends in terms of the stress drop at the source.

2.8   Error Analysis

If all the errors in calculating the stress drop in Equation (2.8) are the result of the errors associated in determining the observed spectral parameters (Ω_0 and f_c) then, following Snoke [1987], the fractional variance in the stress drop is given by Equation (2.31):

<table>
<tr>
<td>Equation
2.31</td>
<td>$$\left[\frac{\delta\sigma}{\sigma}\right]^2 > \left[\frac{\delta\Omega_0}{\Omega_0}\right]^2 + 9\left[\frac{\delta f_c}{f_c}\right]^2 > 10\left[\frac{\delta\Omega_0}{\Omega_0}\right]^2$$</td>
</tr>
<tr>
<td colspan="2">Fractional Variance of the Stress Drop in the context of the Brune Stress Drop</td>
</tr>
</table>

The inequality on the right-hand-side (RHS) is associated with the assumption that errors in estimating the corner frequency are typically greater than the errors in estimating the zero-frequency displacement amplitude.

Snoke [1987] replaced the observed corner frequency with the observed integral of the square of the ground velocity when estimating the stress drop. The fractional variance in the stress drop (whether the Brune stress drop or the apparent stress), in which the stress drop is proportional to the ratio between the I_{V2} and Ω_0, is given by Equation (2.32):

$$
\begin{array}{|c|c|}
\hline
\text{Equation } 2.32 & \left[\dfrac{\delta\sigma}{\sigma}\right]^2 > \left[\dfrac{\delta\Omega_0}{\Omega_0}\right]^2 + \left[\dfrac{\delta I_{V^2}}{I_{V^2}}\right]^2 \cong 2\left[\dfrac{\delta\Omega_0}{\Omega_0}\right]^2 \\
\hline
\multicolumn{2}{|c|}{\text{Fractional Variance of the Stress Drop in the context of the Methods offered by}} \\
\multicolumn{2}{|c|}{\text{Snoke [1987]}} \\
\hline
\end{array}
$$

Here we assume that the errors associated in estimating the zero-frequency displacement amplitude are approximately the same as the errors associated in estimating the integral of the square of the ground motion.

This error analysis is repeated for the methods offered by Andrews [1986], in which the observed zero-frequency displacement amplitude and corner frequency are both replaced by a relationship between the integrals of the square of the ground motion. The fractional variance in the stress drop using this method, in which the stress drop is proportional to the ratio between $(I_{V2})^{5/4}$ and $(I_{D2})^{3/4}$, is given by Equation (2.33):

$$
\begin{array}{|c|c|}
\hline
\text{Equation } 2.33 & \left[\dfrac{\delta\sigma}{\sigma}\right]^2 = \dfrac{25}{16}\left[\dfrac{\delta I_{V^2}}{I_{V^2}}\right]^2 + \dfrac{9}{16}\left[\dfrac{\delta I_{D^2}}{I_{D^2}}\right]^2 > 2\left[\dfrac{\delta I_{V^2}}{I_{V^2}}\right]^2 \cong 2\left[\dfrac{\delta\Omega_0}{\Omega_0}\right]^2 \\
\hline
\multicolumn{2}{|c|}{\text{Fractional Variance of the Stress Drop in the context of the Methods offered by}} \\
\multicolumn{2}{|c|}{\text{Andrews [1986]}} \\
\hline
\end{array}
$$

The Andrews [1986] and the Snoke [1987] methods for calculating the stress drop significantly reduce the fractional variance in estimating this parameter.

The Brune Far-field Displacement Pulse

The Brune Far-field Displacement Pulse Shape

FIGURE 2.1: The Brune model for the far-field displacement pulse shape caused by the instantaneous shear dislocation of a circular fault due to double-couple forces. The shape, specifically the height and width, of the pulse is related to the slip velocity at the source and, therefore, the amount of energy radiated seismically (a measure of how dynamic or energetic the event is). The area under the pulse shape, on the other hand, is proportional to Ω_0 and, therefore, the static seismic moment (a measure of the static size of the event).
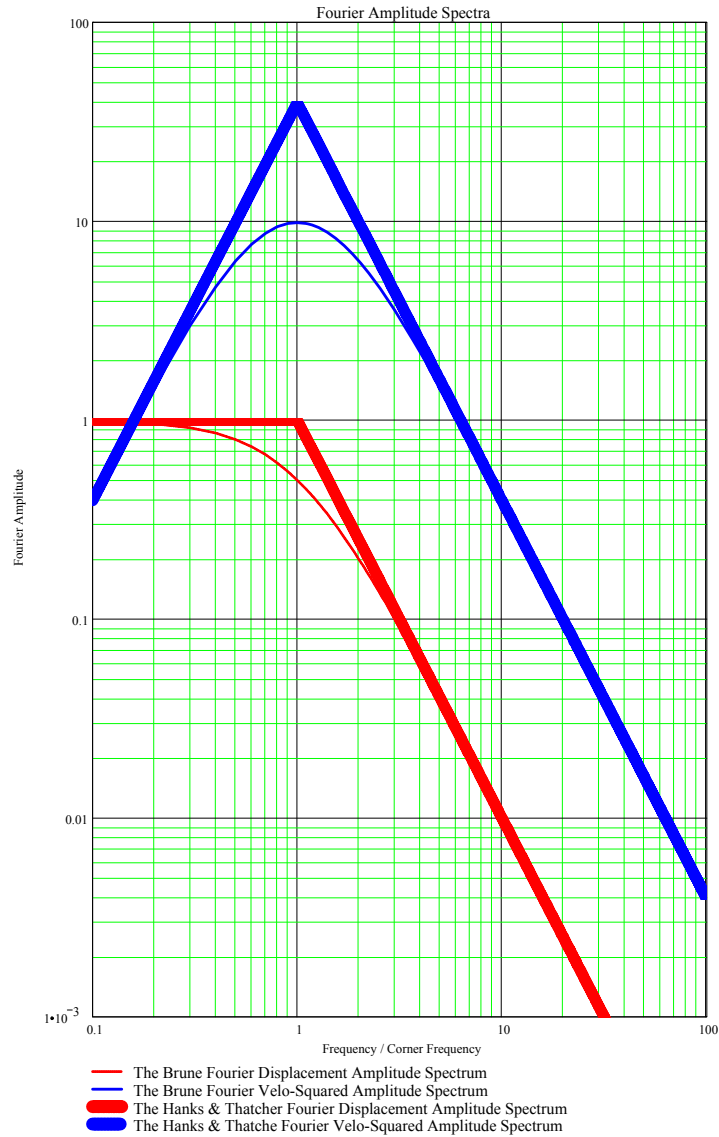
FIGURE 2.2: The Brune far-field displacement pulse of Figure (2.1) transforms from the time domain into the frequency domain as illustrated by the thin-red curve above. The Fourier velocity-squared amplitude spectrum that corresponds to the Brune model, in this example, is illustrated by the thin-blue curve above. A convenient approximation to the Brune model using straight-lines is given by Hanks and Thatcher [1972]. The Fourier displacement and velocity-squared amplitude spectra that correspond to the Hanks and Thatcher model are illustrated above as the thick-red curve and the thick-blue curve, respectively. Note that we normalize the horizontal axis to reflect where the ratio between the frequency and corner frequency is equal to unity.

Chapter 3: Limits on Estimation of Seismic Source Parameters

In this section we examine the problems and limitations imposed on the estimation of seismic source parameters caused by finite recording bandwidth (i.e. finite sample rate and instrument response) and propagation effects (i.e. attenuation and scattering). These issues have been previously addressed by several authors to various degrees [Abercrombie (1995); Anderson (1986); Anderson and Hough (1984); Boore (1986); Di Bona and Rovelli (1988); Frankel and Wennerberg (1989); Hanks (1987); Snoke (1987)]. To summarize, finite recording bandwidth and propagation effects can artificially bias the estimates of the seismic source parameters. We also consider the problem of distinguishing finite bandwidth and/or propagation effects from source-generated effects (e.g., a minimum source dimension, as proposed by Archuleta [1986].

We consider theoretical Fourier displacement amplitude spectra that conform to the Brune model of Equation (2.3). We estimate the spectra such that the zero-frequency displacement amplitude and corner frequency are parameterized in terms of the seismic moment (Equation 2.5) and the Brune stress drop (Equation 2.8), assuming a constant stress drop (1.0 MPa = 10 bar), constant hypocentral distance (1000 m), and constant material properties (S- wave velocity 3200 m/s, density 2700 kg/m^3). We use a range in seismic moment for the theoretical events that correspond to the moment magnitude range of $-4 \leq M_W \leq 4$.

3.1 Bandwidth and Propagation Effects

The Fourier displacement amplitude spectra of the theoretical events, based on the above criteria, are illustrated in Figure (3.1) over the frequency range between 10^{-1} and 10^5 Hz. The corresponding velocity-squared spectra of the theoretical events are illustrated in Figure (3.2). Initially, we assume that we have two sensors in the same location with different bandwidth properties, one with large bandwidth between 10^{-1} and 10^5 Hz and the other with small bandwidth between 10^1 and 10^3 Hz. The lower limit of the bandwidth limitation is primarily affected by the number of time samples transformed into the frequency domain. In this study, we find it is necessary to keep the time segment short because the S-wave arrival is closely followed by the arrival of the surface waves, which we do not want to include. The upper limit of the bandwidth limitation is primarily affected by the sample rate of the data in the time domain. The upper and lower limits of the bandwidth limitations are also affected by the instrument response of the sensor and by noise contamination. If we consider the limitations imposed by the sensor with smaller bandwidth on a purely hypothetical basis, as illustrated with the Blue shaded boxes in Figures (3.3) and (3.4), it is evident that the effects of finite bandwidth alone may lead to underestimates in the corner-frequency for the smaller events and underestimates of the zero-frequency displacement amplitude for the larger events. When the true corner frequency and zero-frequency displacement amplitude cannot be resolved, the estimates of the integrals of the square of the ground motion (I_{V2} and I_{D2}) will reduce due to the inability to estimate appropriate bandwidth corrections (shown later in this chapter).

We numerically introduce intrinsic attenuation and scattering into the original system such that the spectra can be corrected (back to the spectra in Figures 3.1 and 3.2) using Equation (2.15) for T^* equal to $6.25 \cdot 10^{-4}$ sec (equivalent to a frequency-independent quality factor Q of 500 with the assumed hypocentral distance and wave velocity). Theoretical spectral shapes of the events suffering from the artificial propagation effects are shown in Figures (3.5) and (3.6). The affect of the simulated propagation effects on the smaller events results in the appearance of a convergence toward a constant value of the corner frequency. The significant fall-off in amplitudes at frequencies greater than ~1000 Hz can, theoretically, be identified as an effect of propagation (attenuation and scattering) when we consider the sensor with the large bandwidth, since we can observe the exponentially decreasing amplitudes. However, when we consider the sensor with the smaller bandwidth, this distinction is not as obvious and the effect of attenuation may be incorrectly interpreted as a source effect by an observer. For example, an apparent constant corner frequency could, in principle, be misinterpreted as an effect of a minimum source dimension [Archuleta (1986)].

In the context of Fourier amplitude spectra that conform to the Brune model, the E_s/M_0 ratio is proportional to both the apparent stress and the Brune stress drop. The previous theoretical spectra were generated for events with identical stress drops and, therefore, conform to the idea of constant stress drop scaling. For that reason, the estimates of the E_s/M_0 ratio (and similarly the apparent stress and the Brune stress drop) will result in the same value independent of the seismic moment, as long as the energy of the theoretical events are not attenuated and/or scattered during propagation and were recorded using an instrument of adequate bandwidth.

Consider the estimates of the E_s/M_0 ratio for the Fourier amplitude spectra of Figures (3.5) and (3.6) using sensors of infinite bandwidth, 10^{-1} to 10^5 Hz bandwidth, 10^0 to 10^4 Hz bandwidth and 10^1 to 10^3 Hz bandwidth. If the effects of both the finite bandwidth and the propagation path are not corrected, the estimates of the E_s/M_0 ratio for the events will lead to trends illustrated in Figure (3.7a). In this case, these effects result in estimates of the E_s/M_0 ratio that are approximately the same regardless of the size of bandwidth. In addition, the sensors with an imposed lower bandwidth limit that is not adequately low enough to resolve the low-frequency amplitudes of the larger events (the sensor with the smallest bandwidth, in particular) results in reduced estimates of the seismic moment and the integrals of the square of the ground motion. The estimates of the radiated energy do not scale down proportionally, however, and lead to estimates of the E_s/M_0 ratio that are actually *larger* than the true value, as illustrated by the yellow line for large events in Figure (3.7a).

Corrections for the propagation effects, using Equation (2.15), significantly improve the estimates of the E_s/M_0 ratio for the sensors that have large bandwidth, as illustrated in Figure (3.7b). The estimates of the E_s/M_0 ratio for the sensors that have small bandwidth do not improve appreciably because significant portions of the velocity-squared spectrum are outside of the data bandwidth limits. Finally, corrections for the effects of finite bandwidth, using Equation (2.18), are computed for the theoretical spectra and the final estimates of the E_s/M_0 ratio are illustrated in Figure (3.7c). The estimates of the E_s/M_0 ratio from the sensors with small bandwidth improve by a marginal factor of 4, at best. The estimates of the E_s/M_0 ratio from the sensors with small bandwidth cannot fully recover the true estimates of the ratio because of the inability to resolve the Fourier amplitudes beyond the Nyquist frequency (without the aide of another sensor of

larger bandwidth to compare it to). Therefore, we can only "best" approximate the correction factors for these data by considering the Nyquist frequency as a *lower bound* on the estimate of the corner frequency. However, events with corner frequencies that are relatively close to the Nyquist frequency or appear to be greater than the Nyquist frequency (i.e. no observable spectra fall-off) should not be analyzed because of the possibility of introducing significant errors due to the uncertainty in this important spectral parameter.

We again consider the theoretical events that produced the spectra of Figures (3.1) and (3.2), and assume that the energy from these events, as illustrated, was not subjected to propagation effects. In Figure (3.8), we assume we have seven sensors with Nyquist frequencies that span three orders of magnitude and we compute the E_s/M_0 ratio for the theoretical events without correcting for the bandwidth. Here, we also assume that the observed frequency range for each sensor is not limited by a lower bandwidth limit, as we did in the previous analysis, which leads to the assumption that the zero-frequency displacement amplitude and corner frequency of the large events are adequately resolved (thus no over estimate in the E_s/M_0 ratio or stress drop). This figure demonstrates the importance of having at least some *a priori* knowledge about the approximate size of the events for a planned study to ensure that the instruments have adequately large sample rate.

In Figure (3.9), the fraction of the cumulative integral of the displacement- and velocity-squared spectrum is plotted against the ratio between the frequency and source corner frequency [after Ide and Beroza (2001)], where the vertical axis is linear and the horizontal axis is logarithmic. This plot demonstrates the significance of the effects of finite bandwidth. Under the assumption of the Brune model and no energy loss from propagation effects, nearly 90 percent of the total velocity-squared spectrum should theoretically be recovered through integration up to a Nyquist frequency equal to ten times the corner frequency, where nearly 70 percent of all the total integral lies within the decade greater than the corner frequency. The plot also shows that integration of the displacement-squared spectrum up to the corner frequency should yield over 80 % of the total spectrum. Approximate errors associated with estimating the integrals of the square of the ground motion can also be qualified here. Fourier displacement-squared amplitudes (Blue line) inside the range of $0.1 \leq f/f_c \leq 2$ make significant contributions to the total integral, whereas amplitudes outside of this range hold only minimal contribution. Fourier velocity-squared amplitudes (Red line) inside the range of $0.8 \leq f/f_c \leq 20$ make significant contributions to the total integral, whereas amplitudes outside of this range hold only minimal contribution.

In Figure (3.10), we assume that we have recorded events using the sensor with large bandwidth (Nyquist = 10^5 Hz). We vary the intensity of the propagation effects through T^*, which we prescribe to span eight orders of magnitude, and compute the E_s/M_0 ratio for the theoretical events without correcting for these effects. Figure (3.10) indicates that severe intrinsic attenuation and scattering may lead to severe underestimates in the E_s/M_0 ratio, and similarly the apparent stress, which in some cases may be underestimated by several orders of magnitude if the effects are not properly accounted for.

In Figure (3.11), we consider theoretical events with stress drops that span two orders of magnitude that are recorded with a sensor with a Nyquist frequency of 1000 Hz. The thin lines in Figure (3.11) represent the estimates of the E_s/M_0 ratio for the events that have not been corrected for the simulated propagation effects ($T^* = 10^{-3}$ sec). The thick lines in this figure can

be interpreted as estimates of the E_s/M_0 ratio that either have been appropriately corrected for the propagation effects or for events that were not subjected to propagation effects (i.e. $T^* = 0.0$ sec). The effects of finite bandwidth clearly reduce the resolution of the E_s/M_0 ratio (and hence the stress drop) for smaller events in this range. In Figure (3.12), the inability to resolve the differences in the E_s/M_0 ratio and stress drop for the small magnitude events is attributed to the inability to resolve the differences in the high-frequency spectral amplitudes and the corner frequency at frequencies beyond the Nyquist.

3.2   Source Effects

The previous section considers how the effects of finite bandwidth and the propagation path may lead to the *appearance* of a breakdown in constant stress drop scaling. However, it is also important to consider the case where the observed breakdown in constant stress drop scaling actually reflects the true nature of the source. In Figure (3.13), we consider the effects of a minimum source dimension on our estimates of the E_s/M_0 ratio by varying the minimum source dimension over three orders of magnitude. We allow the source dimension to scale with seismic moment over a variety of ranges in seismic moment. We assume that the source is circular (after the Brune model), which leads to fault area dimensions that are proportional to the radius-squared. We scale the radius of the circular fault with the seismic moment until the prescribed minimum source radius, *r*(min), is met for each model. Once the minimum source radius is met, we hold the radius of the theoretical circular fault constant through any further decrease in seismic moment. In the context of the Brune model, a constant source dimension is consistent with the spectral observation of a constant corner frequency. Archuleta [1986] estimated a minimum source dimension of approximately 100 meters for the events associated with the aftershock sequence at Mammoth Lakes, California. A minimum source dimension of 100 m corresponds to a seismic event with a moment magnitude of approximately 3. A number of studies have found an apparent breakdown in the self-similarity of earthquakes below moment magnitude ~3 and have attributed the breakdown to effects related to a minimum source dimension [e.g. Archuleta *et al.* (1982); Baken *et al.* (1976); Chouet *et al.* (1978); Fletcher (1980); Guo *et al.* (1992); Spottiswoode and McGarr (1975), and; Rydelek and Sacks (1989); Tucker and Brune (1973)].

Archuleta [1986] emphasizes the importance of observing the trends in the raw spectra to distinguish between effects that are potentially caused by the source and effects that are potentially caused artificially through propagation or the recording procedure. We have presented a straightforward model of attenuation similar to that presented by Anderson [1986], which explains how the propagation effects might lead an observer to confuse the true corner frequency of an event with, essentially, an effect of an attenuation induced f_{max}. Archuleta [1986] explains that a critical, and often over-looked, observation is that the high-frequency displacement amplitude fall-off rate remains constant in the spectra for events that have source controlled effects. The exponential transfer function that controls the attenuation model, on the other hand, produces a continuously steeper curve when plotted log-amplitude versus log-frequency and, as Archuleta [1986] indicates, should theoretically be distinguished from events controlled by real source effects as long as there is adequate bandwidth beyond the corner frequency. For this reason, the nearly constant corner frequencies of the smaller events studied

by Archuleta *et al.* [1982] were interpreted to be the result of source effects rather than effects due to propagation.

There are also studies that have suggested analogies between the rock frictional models studied in the laboratory and the rocks related to the fault zone structure [i.e. Byerlee (1967); Byerlee and Brace (1968); Dietrich (1979, 1986)). These authors have suggested that the frictional characteristics of rocks are dependent on slip and time, which is especially the case in rocks that, before rupture, are either thoroughly intact or have pre-existing fractures that have not had enough time or enough slip to have developed thoroughly. Over the course of several slip events, the frictional characteristics along the fracture plane begin to gradually weaken through grinding. This is typically referred to as slip weakening and has been suggested, in association with the concept of a minimum source dimension, as the possible cause in the breakdown of self-similarity by many studies [i.e. Aki (1979); Dietrich (1979, 1986); Ida (1973); Papageorgiou and Aki (1983a, 1983b), and; Richardson and Jordan (2002)].

The study done by Richardson and Jordan [2002] offers significant evidence for a breakdown in constant stress drop scaling for seismic events induced by mining operations in a deep South African gold mine. They present evidence for two distinct types of seismic events that occurred at these mines, fracture-dominated events and friction-dominated events. Fracture-dominated seismic events (they call Type-A events), are composed of relatively small events (based on the estimated seismic moment) that were both spatially and temporally clustered within a location in the vicinity of blasting operations immediately following the blasting of material. Richardson and Jordan [2002] associated the "Type-A" events with the rupture of intact (competent) rock induced by dynamic stresses created by the blasting of material as well as the stress perturbations associated with the excavation and the closure of individual stopes. Friction-dominated seismic events (they call Type-B events), are composed of relatively larger events that were distributed throughout the mine and did not necessarily occur near active mining areas. Richardson and Jordan [2002] associate the "Type-B" events with the dislocation of material in existing shear zones such as dykes and faults, including older "Type-A" fractures. They observed that all of the friction-dominated events (Type-B) had virtually identical high-frequency spectral cut-offs at approximately 150 – 200 Hz. In testing whether the f_{max} was an artifact of the propagation path or a direct effect of the source, they discovered that the spectra corresponding to the fracture-dominated events (Type-A) had no observable evidence of a high-frequency spectral cut-off. This led to their conclusion that the high-frequency spectral cut-off observed in the friction-dominated events (Type-B) was *not* controlled by the propagation path. Instead they argued that the cut-off was controlled by the existence of a minimum earthquake at moment magnitude of ~ 0, which corresponded to events where the corner frequency was approximately equal to the observed f_{max}. The authors also argued that the sources of misinterpreting f_{max}, as outlined by Anderson [1986], were not an issue because of the fact that the events in their study were recorded only a few source radii away *and* that the observation of virtually no f_{max} in the spectra of the fracture-dominated seismic events meant that the f_{max} observed in the spectra of the friction-dominated events was not controlled by propagation effects.

In summary, we find that not properly accounting for the propagation effects contributes to the most significant source of underestimation in the radiated seismic energy and, similarly, the stress drop. Limitations due to the various effects associated with the recording and

processing procedure may also cause one to significantly underestimate these parameters. The underestimation may potentially be avoided by considering only those events with corner frequencies that appear to be well below the Nyquist frequency. If one were to only analyze events with corner frequencies that appear to be less than or equal to one-fifth the Nyquist frequency, as a rule of thumb, then in principle, there should be an adequate number of Fourier amplitudes beyond this frequency that would help identify the cause of its frequency location as either a source effect or a non-source effect [Abercrombie (1995)]. In addition to this distinction, it would also allow one to properly account for the limitations imposed by the recording and processing procedure. However, if one were not to take the above considerations into account, the estimates for each seismic parameter (M_0, E_s, etc.) and the trends made by comparing these parameters may lead one to make inappropriate interpretations concerning the physical processes associated with the recorded seismic events. In this study, for example, we examine whether there is a temporal relationship between the apparent stress of the seismic events and the roof falls that follow the seismic activity (discussed in Chapter 5). If all the events correspond to the idea of constant stress drop scaling, there would be no such relationship. However, if the seismic energy traveling through rock for the same events is significantly attenuated and is not corrected for during data processing, the resulting seismic parameter estimates may lead to an apparent divergence from constant stress drop scaling and, therefore, an incorrect hypotheses pertaining to the underlying physical processes associated with the seismic events.

Fourier Displacement Amplitude Spectra

Source-Receiver Distance = 1000 m ** S-wave Velocity = 3200 m/s

Density = 2700 kg/m^3 ** Radiation Pattern = $\sqrt{(2/5)}$ ** Stress Drop = 10 Bar = 1 MPa
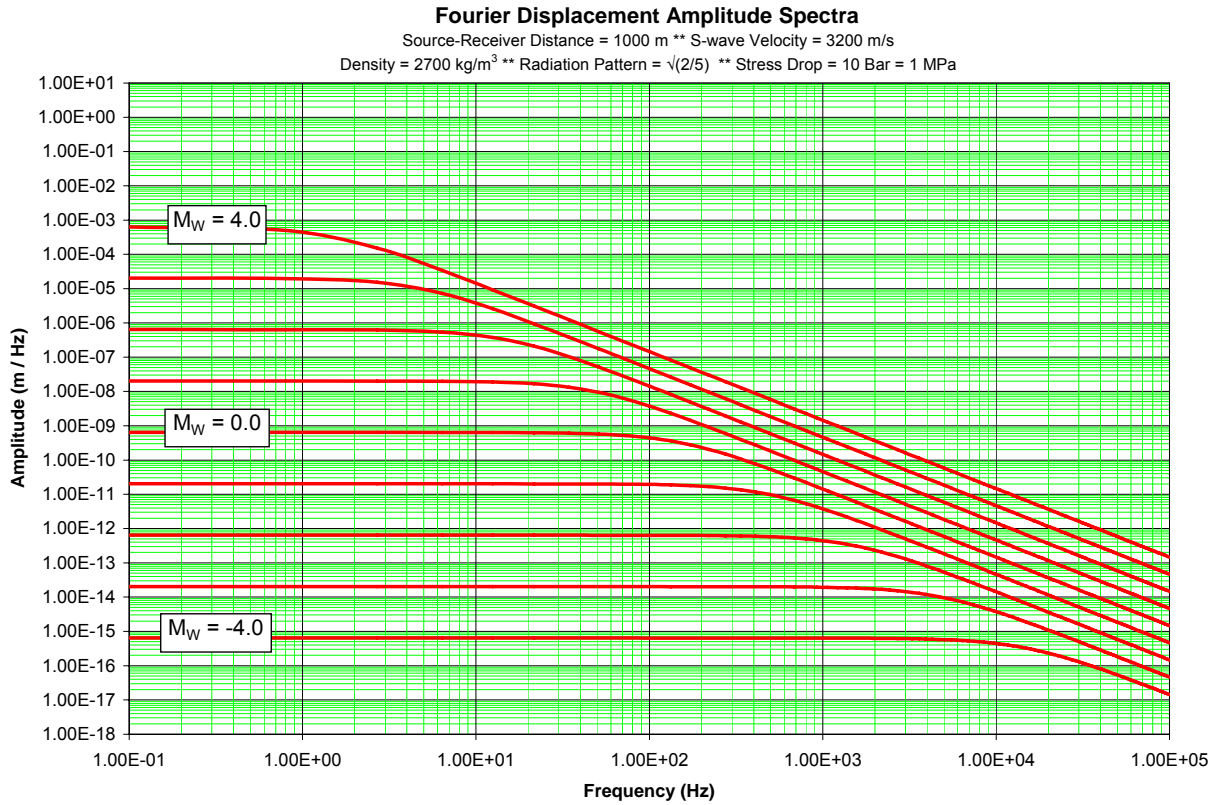
FIGURE 3.1: The Displacement Amplitude Spectra assume a Brune Spectral Shape (Equation 2.3), where the zero-frequency displacement amplitude and corner frequency for each of the nine theoretical events are parameterized in terms of the Seismic Moment (Equation 2.5) and a constant Brune stress drop (Equation 2.8) using the physical properties above.

Fourier Velocity-Squared Amplitude Spectra
Source-Receiver Distance = 1000 m ** S-wave Velocity = 3200 m/s
Density = 2700 kg/m^3 ** Radiation Pattern = $\sqrt{(2/5)}$ ** Stress Drop = 10 Bar = 1 MPa
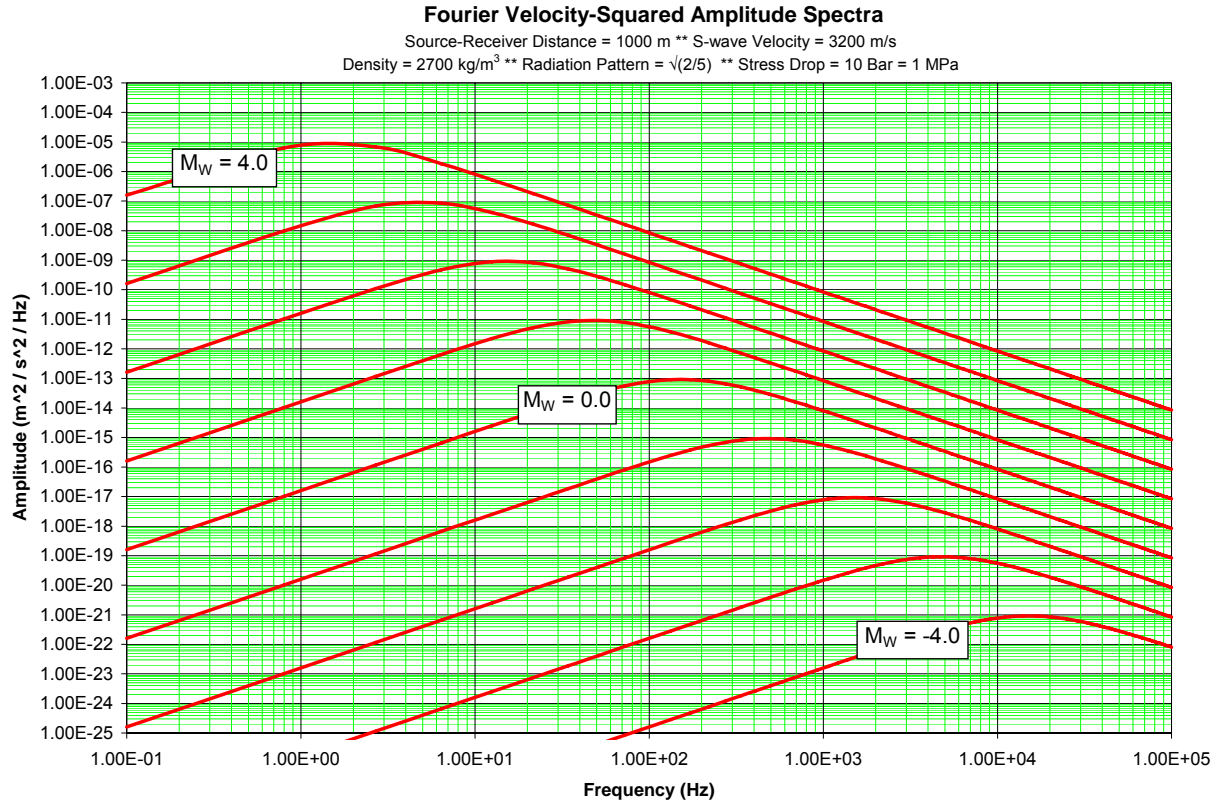
FIGURE 3.2: The Velocity-Squared Amplitude Spectra above correspond to the Displacement Amplitude Spectra of Figure (3.1).

Fourier Displacement Amplitude Spectra

Source-Receiver Distance = 1000 m ** S-wave Velocity = 3200 m/s

Density = 2700 kg/m^3 ** Radiation Pattern = √(2/5) ** Stress Drop = 10 Bar = 1 MPa
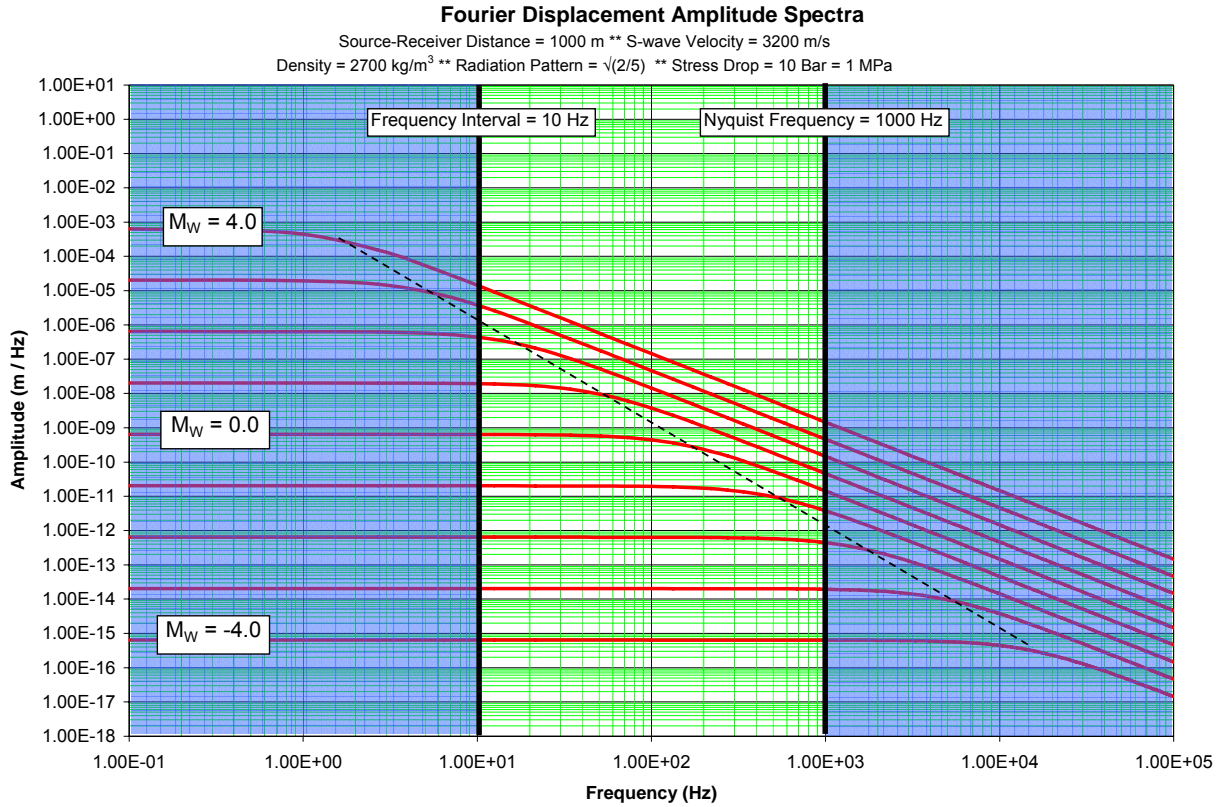
FIGURE 3.3: Idealized Fourier Displacement Amplitude spectra for events with a range in moment magnitude corresponding to -4.0 < Mw < 4.0. The central region of the plot, represents the smallest recording bandwidth (10 to 1000 Hz). Frequencies less than 10 Hz and greater than 1000 Hz (Blue regions) are taken to be outside the bandpass of the recording system. This limitation in the recording bandpass leads to uncertainties in determining the appropriate correction factors in Equations (2.17) and (2.18). The dashed line (slope = f^{-3}) indicates the location of the amplitudes in the theoretical spectra corresponding to $\Omega_0/2$, which are associated with the true corner frequencies of events with a constant stress drop of   1.0 MPa (10 bar) in the context of the Brune model.

Fourier Velocity-Squared Amplitude Spectra
Source-Receiver Distance = 1000 m ** S-wave Velocity = 3200 m/s
Density = 2700 kg/m³ ** Radiation Pattern = √(2/5) ** Stress Drop = 10 Bar = 1 MPa
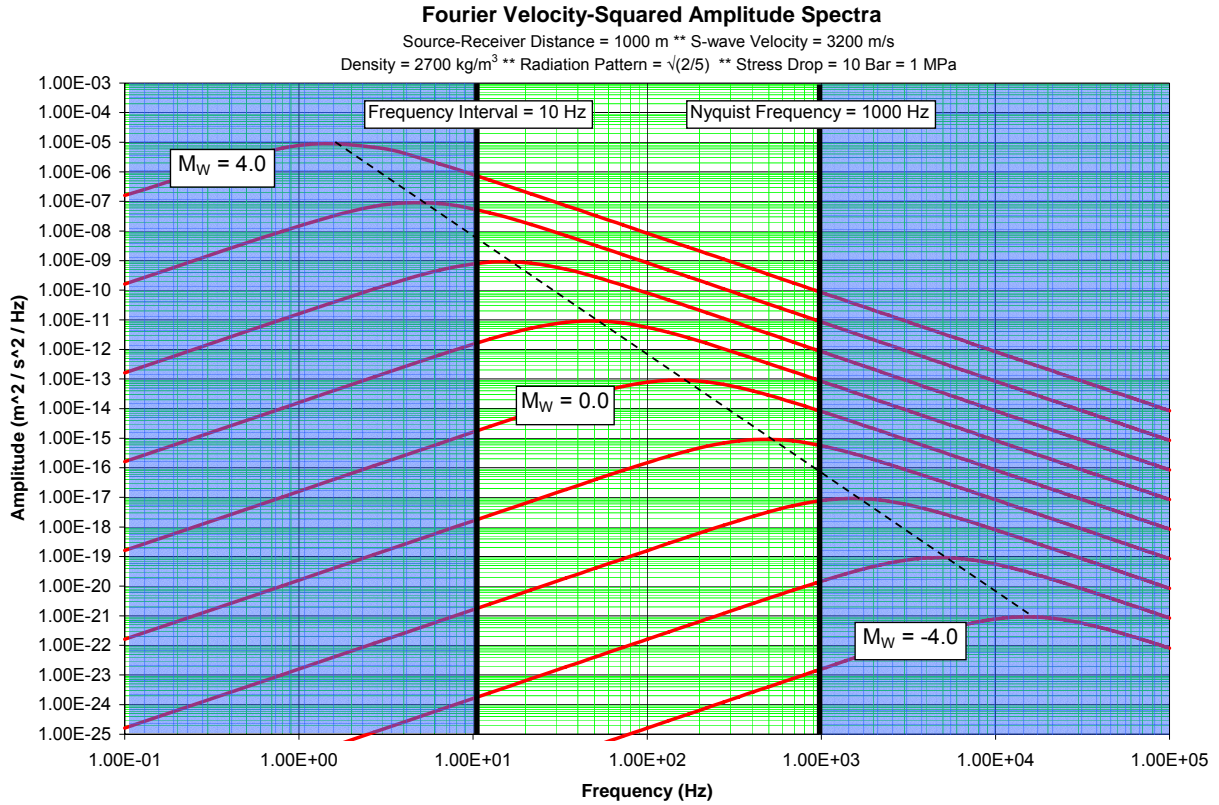
FIGURE 3.4: Idealized Fourier Velocity-Squared spectra for events with a range in moment magnitude corresponding to -4.0 < Mw < 4.0. The central region of the plot represents the smallest recording bandwidth (10 to 1000 Hz). The limitations imposed by the finite bandwidth affect the ability to estimate the Integral of the Velocity-Squared spectra, especially in the blue regions of the spectrum outside the recording band. The dashed line (slope = f^{-4}) indicates the location of the largest amplitudes in the theoretical spectra, which are associated with the true corner frequencies of events with a constant stress drop of 1.0 MPa (10 bar).
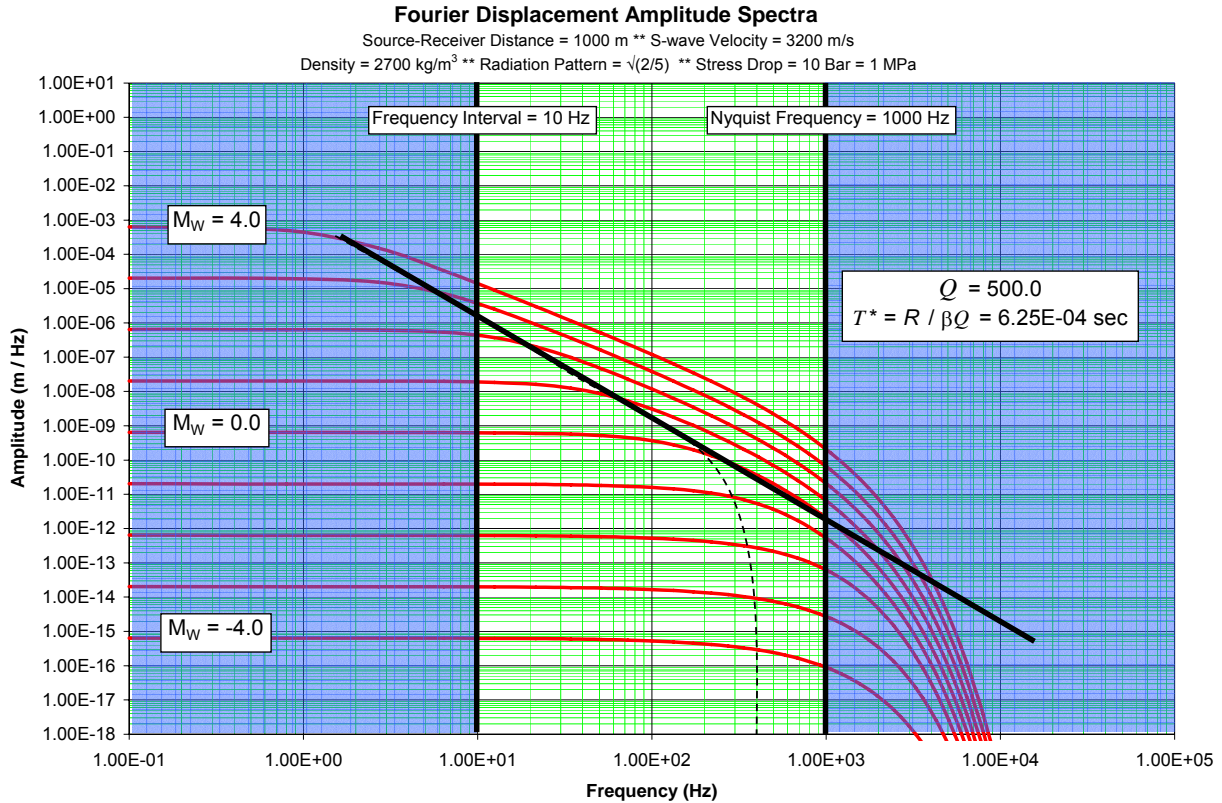
FIGURE 3.5: The result of propagation effects (T* > 0) on the Fourier Displacement Amplitude spectra. Regions shown in Blue are assumed to lie outside the recording bandwidth. The thick, solid line (slope = f^{-3}) indicates the theoretical location of the true corner frequencies for events with a constant stress drop of 1.0 MPa (10 bar). The dashed line indicates where the truncation of high-frequency amplitudes due to the propagation effects might lead an observer to misinterpret the locations of the corner frequency (based on the idea that the true corner frequency corresponds to the frequency associated with an amplitude of $\Omega_0/2$). The limitations imposed by both the Finite Bandwidth effects and the Propagation effects (i.e. Attenuation and Scattering) together impair estimation of the zero-frequency displacement amplitude and the corner frequency.

Fourier Velocity-Squared Amplitude Spectra

Source-Receiver Distance = 1000 m ** S-wave Velocity = 3200 m/s
Density = 2700 kg/m^3 ** Radiation Pattern = $\sqrt{(2/5)}$ ** Stress Drop = 10 Bar = 1 MPa
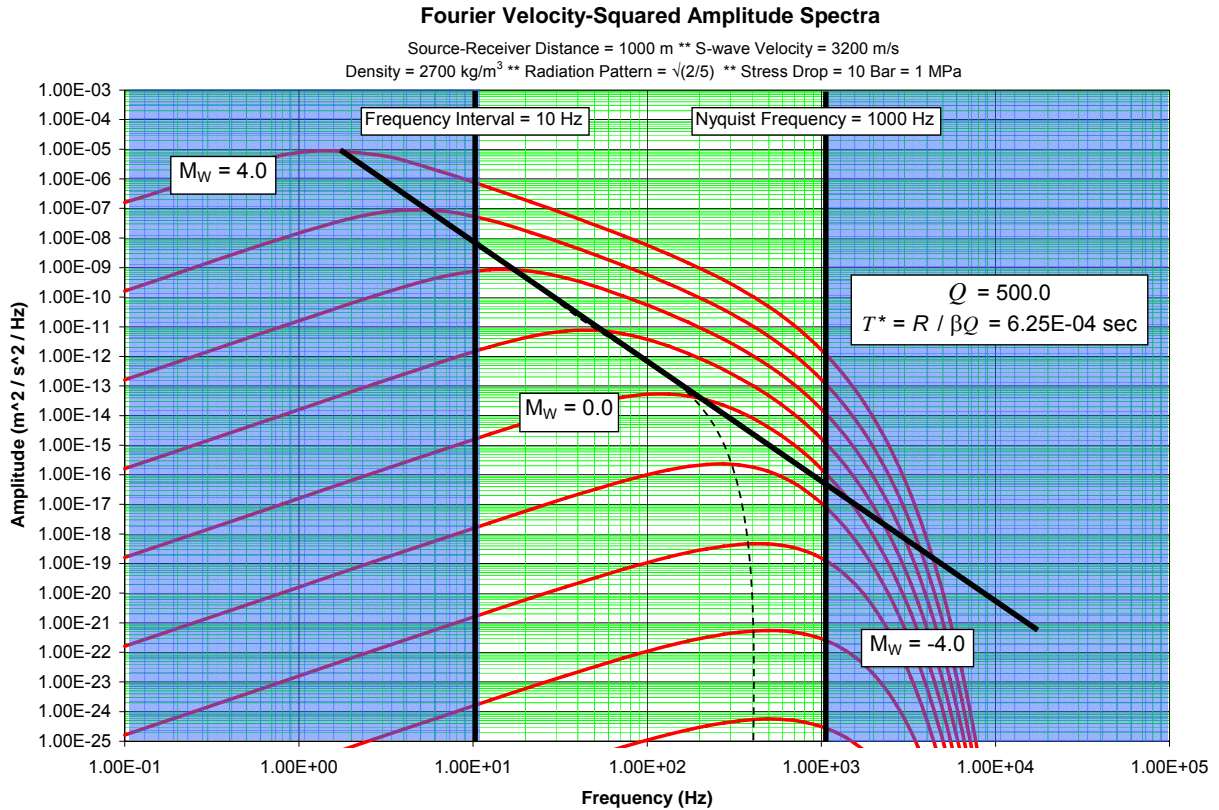
FIGURE 3.6: The result of propagation effects (anelastic absorption and/or intrinsic scattering) on the Fourier Velocity-Squared Amplitude spectra. The limitations imposed by both the finite bandwidth effects and the propagation effects (i.e. Attenuation and Scattering) further impair the ability to estimate the Integral of the Velocity-Squared Spectra. The thick, solid line (slope = f^{-4}) indicates the theoretical location of the true corner frequencies for events with a constant stress drop of 1.0 MPa (10 bar). The dashed line indicates where the truncation of high-frequency amplitudes might lead an observer to misinterpret the locations of the corner frequency (based on the idea that the true corner frequency corresponds to the frequency associated with the largest amplitude in the spectra).
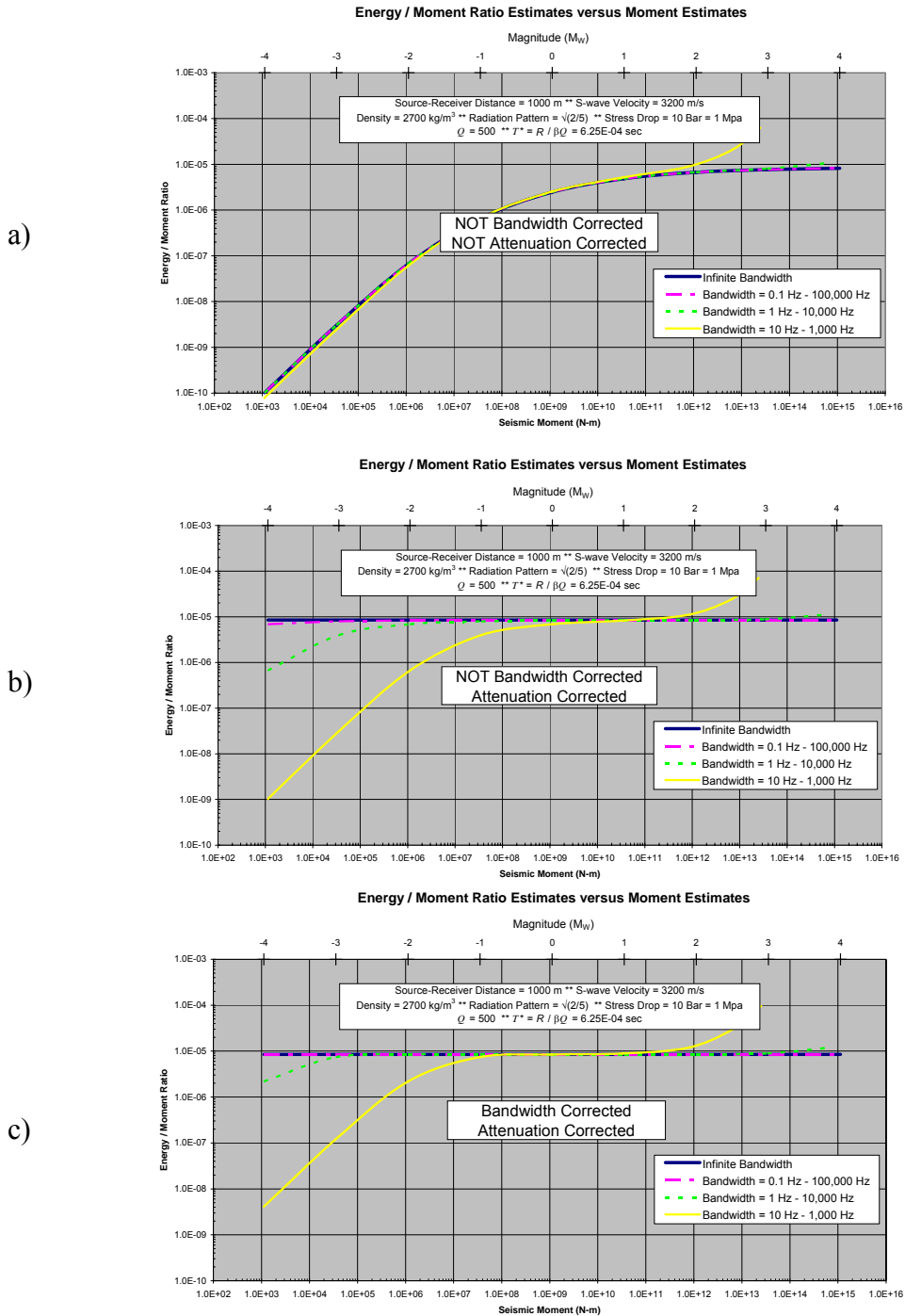
FIGURE 3.7: The result of estimating the ratio between the Radiated Seismic Energy and the Seismic Moment for the nine theoretical events (of Figures 3.5 and 3.6) with four ranges in bandwidth, where:

a) No corrections made for both limitations due to finite bandwidth and propagation effects
b) Propagation effects *are* corrected. Limitations due to finite bandwidth are *not* corrected.
c) Corrections are made for both limitations due to finite bandwidth and propagation effects.

For a constant stress drop, the E_s/M_0 ratio should be constant, independent of the seismic moment.

Energy / Moment Ratio Estimates versus Moment Estimates
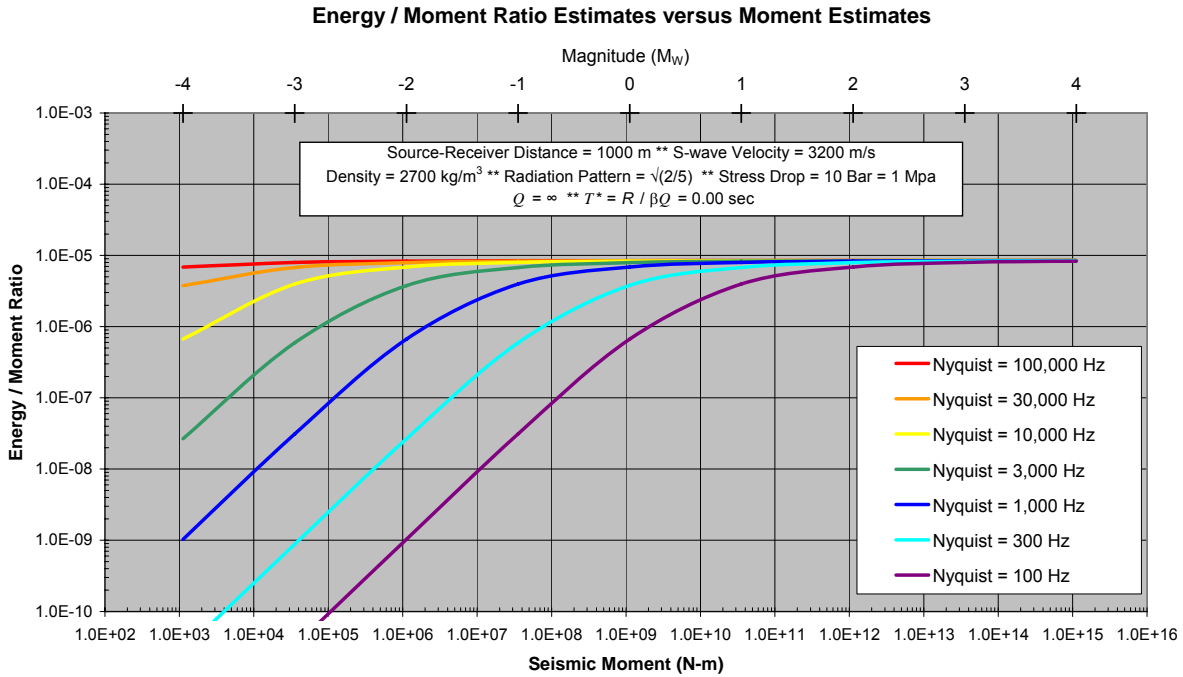
FIGURE 3.8: The result of estimating the ratio between the Radiated Seismic Energy and the Seismic Moment for the nine theoretical events (of Figures 3.1 through 3.2) without correcting for the limitations imposed by the Nyquist frequency (upper recording band limit) and assuming that the data are not affected by the Propagation Effects (i.e. Attenuation and Scattering). Here, the Nyquist frequency ranges over three orders of magnitude and there is no lower bandwidth limit to affect the estimates of the seismic moment.

The Integral of the Brune Velocity-Squared Model
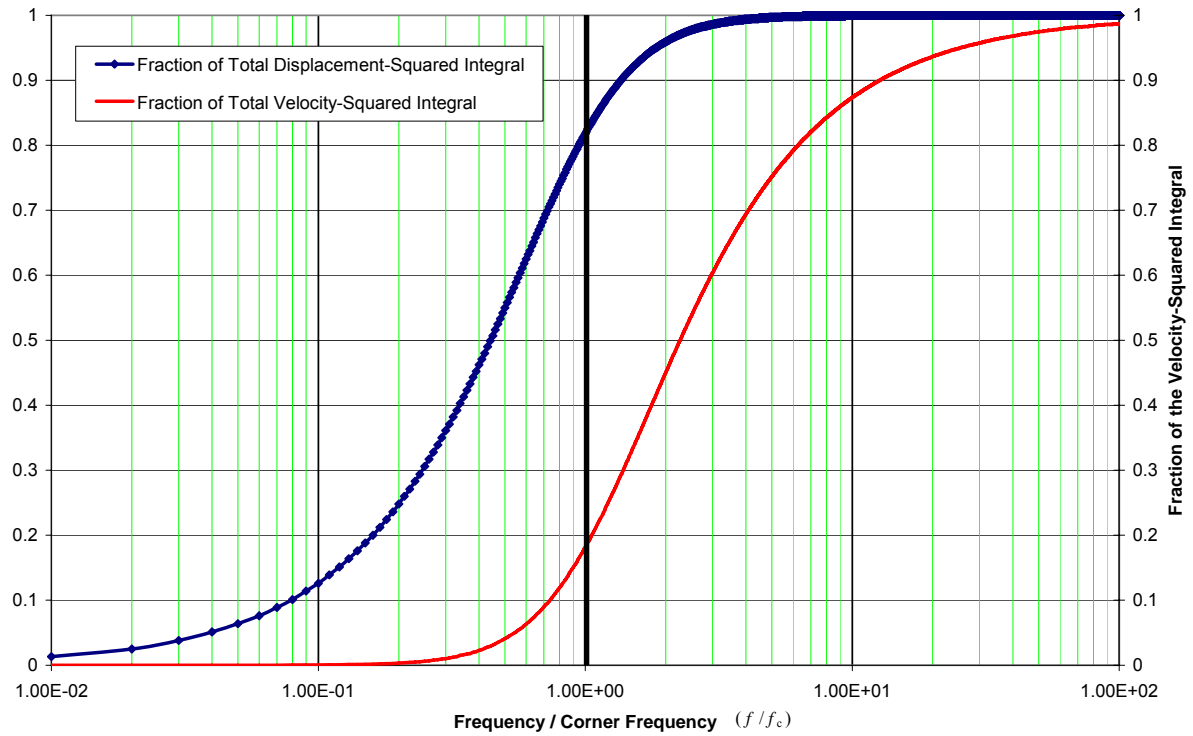
FIGURE 3.9: The Brune model is assumed when integrating both spectral shapes. The blue line represents the Fraction of the Integral of the Displacement-Squared Spectrum. The red line represents the Fraction of the Integral of the Velocity-Squared Spectrum [after Ide and Beroza (2001)].
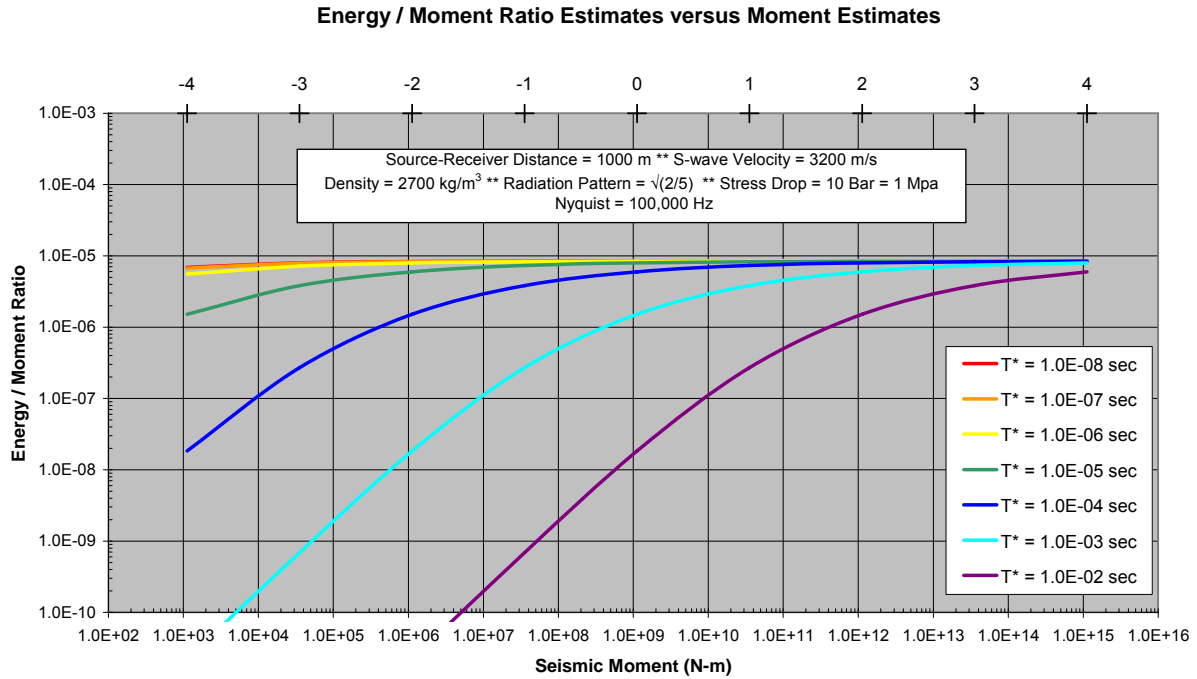
FIGURE 3.10: The result of estimating the ratio between the Radiated Seismic Energy and the Seismic Moment for the nine theoretical events (of Figures 3.1 through 3.2) that have been subjected to a large range in Propagation effects (i.e. Attenuation and Scattering). The single assumed Nyquist frequency is 10^5 Hz, which has a negligible effect on the ratio for events in this range. Considering the hypocentral distance and shear wave velocity constant leads to values of *T** that are equivalent to a range in the Quality Factor (*Q*) of approximately $3 \cdot 10^1$ (Purple Line) to $3 \cdot 10^7$ (Red Line).
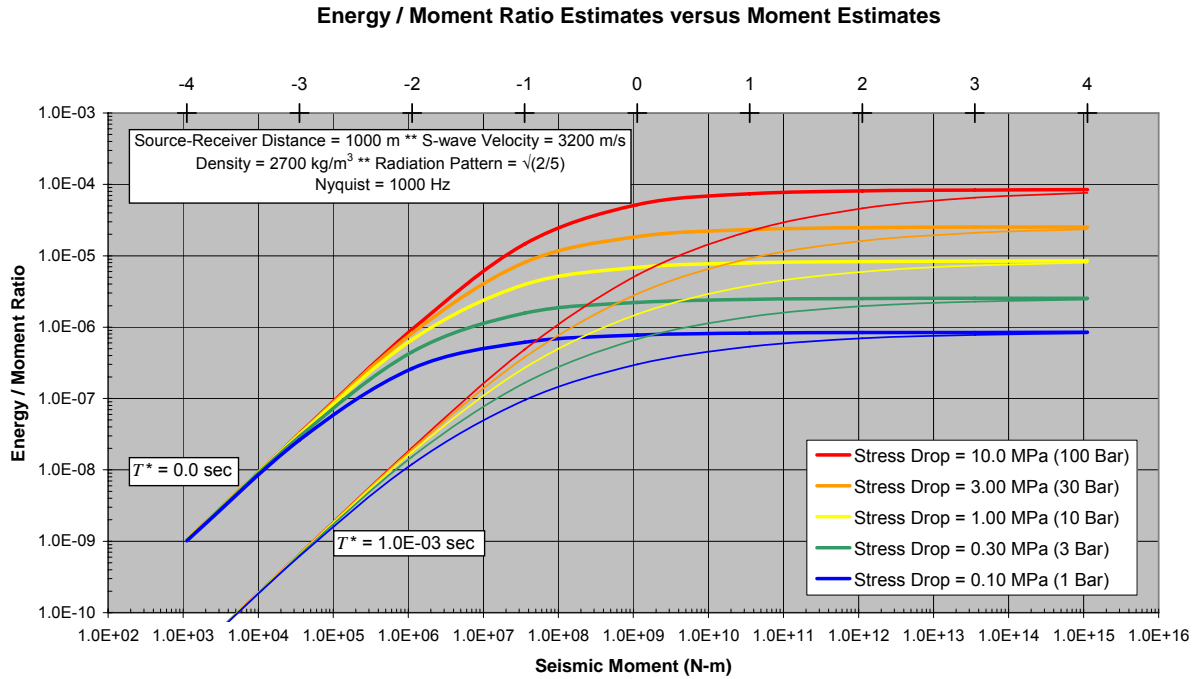
FIGURE 3.11: The result of estimating the ratio between the Radiated Seismic Energy and the Seismic Moment for bandlimited theoretical events that have stress drops that range over two orders of magnitude. The thick colored lines represent events that were not subjected to Propagation effects ($T^* = 0.0$ sec). The thin colored lines represent events with $T^* = 10^{-3}$ sec. The Nyquist frequency is 1000 Hz, in both cases, and the spectra are uncorrected for this finite upper band limit.

Fourier Velocity-Squared Amplitude Spectra

Source-Receiver Distance = 1000 m ** S-wave Velocity = 3200 m/s

Density = 2700 kg/m^3 ** Radiation Pattern = $\sqrt{(2/5)}$ ** T^* = 0.00
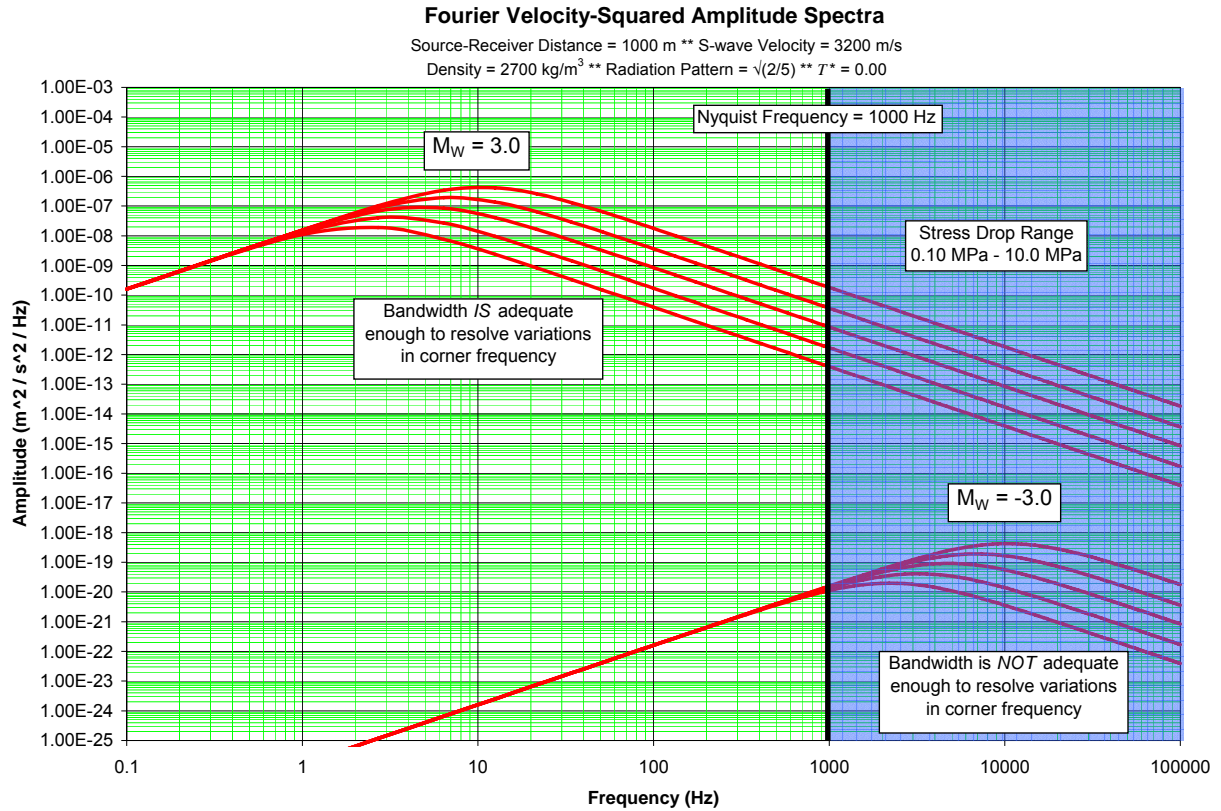
FIGURE 3.12: Illustration depicting the cause of the apparent convergence of the ratio between the Radiated Seismic Energy and the Seismic Moment as the Seismic Moment decreases in Figure (3.11). As shown above in the blue region of the plot for the spectra corresponding to Mw = -3, this apparent convergence is the result of the inability to resolve differences in the corner frequency and area under the theoretical spectra of the small events, regardless of stress drop. This is due to the bandwidth limitation imposed by the 1000 Hertz Nyquist frequency.

Energy / Moment Ratio Estimates versus Moment Estimates

Source-Receiver Distance = 1000 m ** S-wave Velocity = 3200 m/s
Density = 2700 kg/m^3 ** Radiation Pattern = √(2/5) ** T* = 0.0 sec ** Infinite Bandwidth
Events with Source Dimension > r(min) have Stress Drop = 10 Bar = 1 Mpa

Legend:
- r(min) = 0.1 m
- r(min) = 0.3 m
- r(min) = 1 m
- r(min) = 3 m
- r(min) = 10 m
- r(min) = 30 m
- r(min) = 100 m

X-axis: Seismic Moment (N-m)
Y-axis: Energy / Moment Ratio
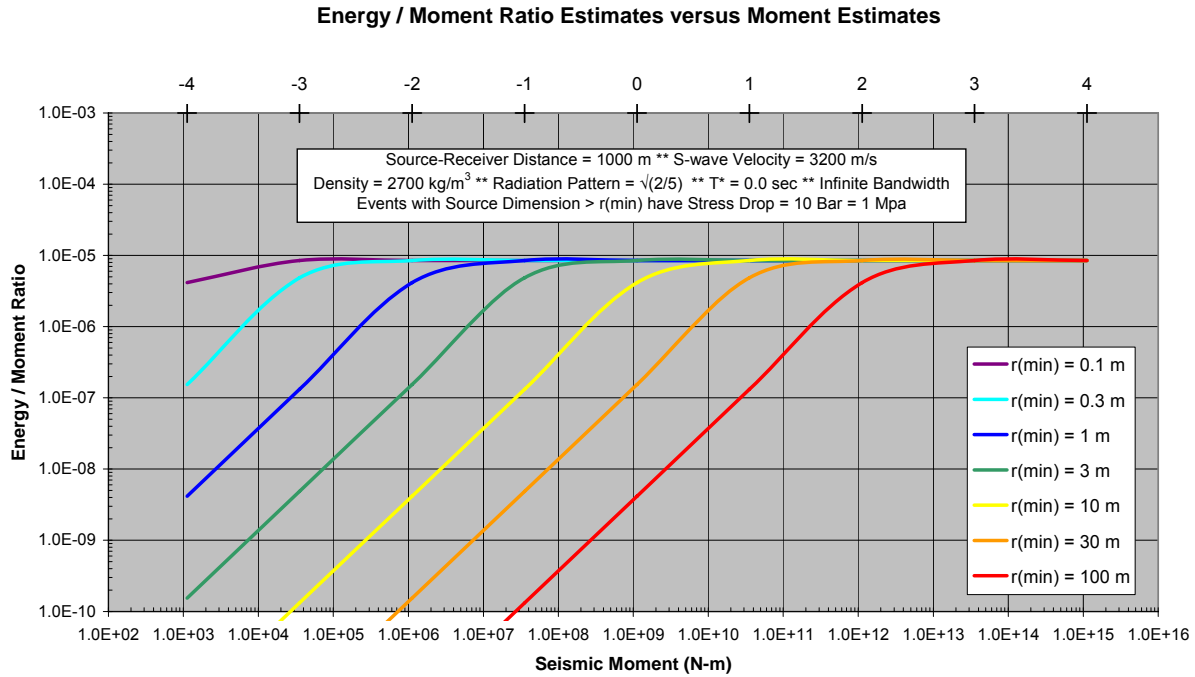
FIGURE 3.13: The result of estimating the ratio between the Radiated Seismic Energy and the Seismic Moment for theoretical events that have a minimum source dimension (i.e. the source dimension does not scale with seismic moment beyond a specific point). We assume the source is circular with fault area dimensions proportional to the radius-squared. The radius of the circular fault scales with seismic moment until the minimum source radius, *r*(min), is met, at which point *r*(min) is held constant. A constant source dimension is consistent with a constant corner frequency, in the context of the Brune model.

Chapter 4: Moonee Colliery Data Set

The Moonee Colliery data set used in this study (illustrated in Figure 4.1) consists of seismic events recorded by four stations (three-component sensors recording at 2000 samples per second) mounted underground, 10 meters into the roof strata (~30 meter thick conglomerate). The majority of the seismic events occurred within the layer of conglomerate and within 20 – 200 meters of the four stations. This study analyzes a small subset of a very large data set collected from this mine.

Extensive processing of these data was done by the underground monitoring system at Moonee, prior to this study. Data from the four stations were used to automatically locate the seismic events. The data were automatically processed and analyzed underground before transmission and recording to determine the dominate frequency content (essentially the corner frequency) of each event. If the dominant frequency of an event was not high enough to justify its recording with a high sample rate, the trace would be decimated by an appropriate factor between 2 and 25. This adaptive recording procedure was necessary because of limited telemetry bandwidth between the stations and the data storage unit. Unfortunately, the decimation factor was not recorded.

4.1   Data Processing Procedure (Part 1: Initial Estimates)

Estimation of the stress drop (apparent stress using the Andrews [1986] method of calculation) was carried out using a program developed in MathCAD. The data obtained from the underground system had been instrument corrected to velocity. Analysis for this study began by attempting to rotate the three-component data into the radial, transverse and vertical directions in order to help identify the P-wave and S-wave phase arrivals. The true orientation of the three-component sensors was, unfortunately, also uncertain. This unknown, as well as the uncertainty in the true sample rate, meant that errors in the automatic event locations are such that errors in estimated backazimuths from the nearest stations in some cases could approach 45 degrees (Figure 4.1). The rotation method is based on the idea that once the two horizontal components were rotated properly into the radial and transverse directions, the transverse component should not have any contribution from the P-wave. This assumes that the events occur approximately in the same horizontal plane containing the sensors, that lateral homogeneity exists, and that a significant portion of energy is not reflected back to the station from other directions within the selected time interval. The first point of seismic motion on the radial component (P_R) should be the P-wave and the first point of seismic motion on the transverse component (P_T) should be the S-wave under the assumed conditions. The maximum difference between the first motion sample points (P_T minus P_R) should theoretically occur when the two horizontal components are rotated properly. To find this difference, we calculated the signal-to-noise ratio of the two horizontal components after each rotation and determined the first point in each trace to rise above the noise by a factor equal to the signal-to-noise ratio threshold, which was 2.0 for our calculations. We assumed the angle of rotation (θ) that led to the largest number of time samples between the first radial sample point above the noise (P_R) and the first transverse sample point above the noise (P_T) to be the best estimate of rotation angle, Φ (Figure 4.2 describes the process in detail).

However, as mentioned earlier, the method described does not work properly if a significant portion of energy is reflected back to the station from directions other than the one back to the source OR when there are significant potions of P-wave energy converted to S-wave energy prior to reaching the station. Ray multi-pathing, and diffraction are expected to be important in the underground environment due to the existence of a variety of velocity contrasts (i.e. geology of roof strata, 3-dimensional free surfaces created by mine openings, etc.).

The next step involved quantifying the signal-to-noise ratio, Rectilinearity and Planarity of the three-component data after the work of Jepsen and Kennett [1990], Jurkevics [1988], McGarr *et al.* [1964] and White [1964]. The signal-to-noise ratio was computed to help identify the onset of the P-wave or S-wave phase arrival. Similar to the rotation process described in Figure (3.2), the signal-to-noise ratio was computed from the ratio between the average power within a moving window and the average power within a window of consistent noise. The polarization parameters Rectilinearity and Planarity were computed to establish how well the combined motion from all three components was polarized along a straight line (high linearity) or a plane (high planarity). The polarization analysis is illustrated in Figure (4.3). The polarization measures were determined by the eigenvalue decomposition of a matrix whose entries represent the sum of the product between the amplitudes within a moving window from all three components. Three eigenvalues are determined in this decomposition, and quantify the relative amplitude dominance, if any, of one (or two) component(s) over another. Jepsen and Kennett [1990] defined Rectilinearity such that its range in values (0.0 – 1.0) would quantify the level of linear polarization between all three components. A Rectilinearity value of 0.0 indicates equivalent amplitudes on all three components, whereas a value of 1.0 indicates that pure linear polarization is detected. Jepsen and Kennett [1990] defined Planarity such that its range in values (also 0.0 – 1.0) would quantify the level of planer polarization between all three components. A Planarity value of 0.0 also indicates equivalent amplitudes on all three components, whereas 1.0 indicates equivalent amplitudes on two components and virtually no motion on the third (motion confined to a plane).

The P-wave and S-wave arrival times were picked following the rotation of components as well as the determination of the signal-to-noise ratio and the polarization parameters (Figure 4.4). The phase arrival times were computed for two reasons: (1) to ensure the S-wave window contained minimal contribution from P-wave and Rayleigh wave motion, and (2) to ensure that the hypocentral distances that were automatically computed by the Moonee underground monitoring system were reasonable, based on S-wave minus P-wave arrival times and assuming average S-wave and P-wave velocities of 2600 m/s and 4500 m/s, respectively [Iannacchione *et al.* (2005b)].

After determining the phase arrival times, the Fourier transform of the S-wave window from the recordings of all three components were computed using the forward Fourier transform (Equation 2.14). The velocity amplitude spectra from all three components were then combined into one frequency domain plot. For each frequency, the square root of the sum of the velocity-squared amplitudes from all three components was calculated. This "total" velocity spectrum represents the L^2-norm of the radial, transverse and vertical amplitudes at each frequency. The equivalent single displacement spectrum (or single acceleration spectrum) was found by dividing

(or multiplying) the amplitudes at each frequency f from the single velocity spectrum by the circular frequency $\omega = 2\pi f$.

The displacement spectra were used to estimate the zero-frequency displacement amplitude (Ω_0), the corner frequency (f_c) and the approximate value of (T^*) needed to correct the high frequency amplitudes for propagation effects based on the assumption of the Brune model (Figure 4.5). Initial estimates of the zero-frequency displacement amplitude were made by selecting a window of low frequency amplitudes and computing the geometric mean amplitude within the window. This method of calculation was such that reasonable estimates of the low-frequency window, in terms of picking ν_1 and ν_Ω as outlined in Section (2.5.2), led to variance in the estimate for Ω_0 that did not exceed $\pm$ 10%. Initial estimates for the corner frequency and quality factor were made simultaneously by inspection, computing a theoretical Brune spectrum and then comparing the theoretical Brune spectrum with the observed spectrum for optimum fit. This process allowed the determination of an estimate of the quality factor (Q) by matching the slope of the observed high frequency spectrum to that of the Brune spectrum for various values of Q. These initial estimates, as well as the estimate for the integral of the velocity-squared spectrum (or velocity power spectrum), were used to make initial estimates of the seismic moment, the radiated seismic energy, and the apparent stress. The initial estimates were then refined by the procedure described below.

4.2 Data Processing Procedure (Part 2: Refined Estimates of the Seismic Moment, Radiated Seismic Energy and Stress Drop)

The various spectra were corrected for the effects of attenuation (Figure 4.6) by multiplying the amplitudes at each frequency by the expression in Equation (2.15). Once the various spectra were corrected for effects of T^*, the integral methods introduced by Andrews [1986] were used to compute the corner frequency and the zero-frequency displacement amplitude (listed in Equation 2.24). First, the T^*-corrected acceleration spectra (Figure 4.7) were analyzed to determine f_{max}, a term defined by Hanks [1982] as the highest frequency in the acceleration spectrum before the spectral plateau begins to break down. The smallest frequency, f_{min}, was determined next by identifying the smallest frequency that consistently conformed to the theoretical source model before beginning to breakdown due to noise contamination or too few sample points in the time domain to constrain the low-frequency amplitudes. Next, theoretical amplitudes of the Brune source spectra were added to the observed source spectra to correct for the absence of low-frequencies below f_{min} and the absence of high-frequencies above f_{max} in the band-limited observed data. The corrections that account for the limitations in the data bandwidth are described in Chapter (2) and (3) and were made using Equations (2.18) and (2.19).

The next step in the analysis procedure was the calculation of the T^*-and-bandwidth-corrected velocity and displacement power spectra in order to obtain improved estimates of the corner frequency and the zero-frequency displacement amplitude based on the relationship between the integrals of the square of the ground motion. The window lengths of the S-wave signal in the time domain were typically short. This resulted in poorly-constrained low-frequency amplitudes and, therefore, suboptimal estimates of the zero-frequency displacement amplitude. We use the Andrews [1986] method of calculation for this reason in an effort to constrain our estimates of the spectral parameters (Ω_0 and f_c). Theoretical Brune source spectra were computed

using the revised estimates of corner frequency and zero-frequency displacement. Final estimates of the seismic moment, the radiated seismic energy and the apparent stress were made based on the T^*-and-bandwidth-corrected source spectra and were compared with the initial estimates.

4.3   The Impact of an Uncertain Sample Rate

The telemetry system at Moonee used an adaptive sample rate but, unfortunately, did not record the decimated sample rate and thereby introduced uncertainty in the actual sample rate of the data. Only the maximum rate of 2000 samples/sec was known. This is a problem that has very important implications pertaining to various estimates such as the approximate hypocentral distance (based on the difference between the S-wave arrival time and the P-wave arrival time), zero-frequency displacement amplitude and corner frequency. As we show in Appendix (5), for this data set, the stress drop is independent of the decimation factor. In the following paragraph we outline our analysis procedure.

We assume that the raw data were corrected to velocity and that the data were sampled at the maximum rate of 2000 samples per second. However, if the data were decimated to $2000/\varepsilon$ samples per second, where ε is the decimation factor (ε =2,3,4,...,25) then the estimates of the zero-frequency displacement amplitude will decrease by a factor equal to ε^{-2}, the hypocentral distance will be reduced by a factor equal to ε^{-1} and the corner frequency will be increased by a factor equal to ε. As a consequence, if the sample rate of the data has been reduced by a factor ε (and is not accounted for) then the estimates of the radiated seismic energy will reduce by ε^{-3} and the seismic moment will reduce by ε^{-3}, leading to neither an increase nor a decrease in the estimate of the stress drop. Thus, estimates of the apparent stress are independent of sample rate under these assumptions (see Appendix 5 for derivation). It is fortuitous that the raw data represents the velocity of the ground motion. If the sensors had been recording either the displacement or acceleration of the ground motion, the estimates of the stress release would have been dependent upon the sample rate in the context of the analysis in Appendix (5). The estimates for seismic moment, however, *are* potentially biased. The seismic moment estimates made here are based on the maximum sample rate (2000 Hz) and therefore represent the lower bound on the possible values for the seismic moment for each event. It turns out that the uncertainties in the sample rate of this study will not *introduce* a non-zero slope to the relationship between the stress drop and seismic moment, if in fact the slope of the relationship under ideal recording conditions is equal to zero (i.e. zero-slope corresponds to constant stress drop scaling). However, if a non-zero linear correlation does exist, the uncertainties in the sample rate *will* affect the slope of the trend since the estimates of the seismic moment represent only a lower bound on the true seismic moment. Uncertainty in the actual decimation factor for this data set allows us to constrain an estimate of the stress drop but not a definitive relationship between the stress drop and the seismic moment (or radiated seismic energy).

4.4   Uncertainty due to Source Radiation Pattern Terms and Material Properties

Other uncertainties associated with this data set are the radiation patterns for the events as well as the velocity and density of the rock between each event and station. In principle, the radiation pattern could be estimated from the recorded data. However, as mentioned earlier, the estimates of the backazimuth angle were uncertain due to uncertainties in the sensor orientations,

uncertainty in the recording sample rate and the fact that only four stations at most were available for each event. The uncertainty in the radiation pattern led us to assume that it was equal to the root-mean-squared (RMS) radiation pattern term for all of our estimates. We chose an average density of 2500 kilograms per cubic meter for all of our calculations. Uncertainties in the average wave velocities in the roof led us to choose two sets of P-wave and S-wave velocities (α = 5000 [4000] and β = 2900 [2300]) that are approximately consistent with a Poisson solid (Poisson ratio = 0.25 and $\alpha / \beta = \sqrt{3}$). The estimates for the seismic moment and the radiated seismic energy using each velocity set were averaged to make the final results plotted in Figures (4.8) and (4.9). Errors associated with the material properties are systematic errors and, therefore, would not introduce non-zero trends into the data (e.g. when plotting the stress drop versus the seismic moment).

4.5   Discussion of the Results for the Moonee Colliery

The results obtained after processing 42 events from the Moonee data set are tabulated in Table (4.1), the relationship between the radiated seismic energy and seismic moment is illustrated in Figures (4.8) and (4.9). The uncorrected estimates (orange triangles) and corrected estimates (maroon triangles) of the radiated seismic energy are plotted against the estimates of the seismic moment in Figure (4.8). The estimates of the radiated seismic energy range between 2 and $3 \cdot 10^3$ J, while the estimates of the seismic moment range between $3 \cdot 10^7$ and $2 \cdot 10^9$ N·m. A least squares fitting scheme for logarithmic data was used to determine the overall trend of the uncorrected and corrected data (also plotted in Figure 4.8). The slope of the trend lines computed for the uncorrected data ($\log(E_S) = 1.48 \cdot \log(M_0) - 10.53$) and the corrected data ($\log(E_S) = 1.51 \cdot \log(M_0) - 10.59$) are very similar, and indicate that the uncorrected results shifted up by a nearly constant factor of ~2 after making the corrections for the propagation effects and the bandwidth limitations. Also plotted in Figure (4.8), are lines representing constant stress drop. The difference between the trend made by the corrected results and the trends of constant stress drop indicate that apparent stress is not constant for the events at Moonee. Instead the apparent stress of the Moonee events appears to increase with seismic moment in a manner similar to that reported by many previous studies. A consequence of computing the spectral parameters using the methods described by Andrews [1986] is that the ratio between the apparent stress and the Brune stress drop, equal to ~0.23, is the same for each event. The reason for this constant ratio is explained in Appendix (4) and is the same result obtained by both Andrews [1986] and Snoke [1987]. By using the Andrews [1986] method we really measure only one independent estimate of the stress drop and, for that reason, only display our estimates of the apparent stress.

The estimated E_s/M_0 ratio for the events at Moonee and the events associated with eight earlier data sets are plotted in Figure (4.9). The estimates for the seismic moment of these events span approximately 10^3 to 10^{15} N·m, which correspond to a range in moment magnitude between -4.0 and 4.0. The estimates of the E_s/M_0 ratio for the majority of these events are contained between the ratios of 10^{-7} and 10^{-4}. This indicates that over twelve orders of magnitude of seismic moment that the stress drop varies between only three orders of magnitude. The seismic events in this compilation occurred in very diverse geologic and stress environments, and suggest that the stress drop for all of the events of each study on average are independent of the seismic

moment. However, a close look at individual studies suggests that the stress drop is not independent of the seismic moment. In fact each study, with the exception of one [Yamada *et al.* (2005a, 2005b)] due to an extremely small data set, indicates a trend of increasing stress drop with increasing seismic moment. As shown in Figure (4.8), we found that *T**-and-bandwidth corrections had little or no effect on the observed trend of increasing E_s/M_0 ratio with increasing seismic moment for the Moonee results (See the maroon and orange triangles in Figure 4.9). The *T**-and-bandwidth corrections generally resulted in an increase in E_s/M_0 ratio no larger than a factor of 2.

Prior to performing any corrections to the initial estimates of the E_s/M_0 ratio for the Moonee data, our hypothesis was that the trend of increasing E_s/M_0 ratio with increasing moment would change significantly after accounting for the propagation and bandwidth effects. The theoretical work in the previous section (Chapter 3) explained that there are three independent potential causes for our observation of increasing E_s/M_0 ratio with increasing moment. The first cause would be an analysis error: failure to correct for propagation effects (i.e. anelastic attenuation and intrinsic scattering) or recording effects (i.e. bandwidth). The second cause would be one of misinterpretation: a failure to distinguish a site effect from a true source effect. Such a case could occur when the material that the station is founded upon acts as a natural low-pass filter. In this case, the corner frequency may be truncated to a value smaller than the true value due to severe propagation effects at the site. The third cause would be a true source effect, due to the dynamics of the rupture or the rock properties in the vicinity of the rupture. We have corrected for propagation and bandwidth effects as best we can and have concluded that despite our inability to resolve the exact sample rate for each record, a trend of increasing E_s/M_0 ratio with increasing seismic moment still remains. The issue of whether the site effects in the vicinity of each of the four stations has naturally contributed to our inability to detect events with corner frequencies above some site induced f_{max} does not seem like a valid argument. In this study the majority of the events occurred within the same layer of conglomerate containing the stations and also occurred within relatively small hypocentral distances (20 to 200 meters) of the stations. This suggests that it is more likely that the trend we interpret as a divergence from constant stress drop scaling is due to physics of the source.

Event (yyyyMMMddhhmmss.ssssss)	M_w	f_c (Hz)	Q	R (m)	M_0 (N·m)	Uncorrected E_s (J)	Corrected E_s (J)	E_s / M_0	σ_a (Pa)
1998MAR26000841378600	-1.	111	50	55	3.8E+07	7.4E+00	1.3E+01	3.6E-07	6.1E+03
1998MAR26010333376200	-0.4	50	50	67	3.2E+08	5.4E+01	8.7E+01	2.8E-07	4.7E+03
1998MAR26010713458400	-0.0	36	170	122	1.0E+09	2.8E+02	3.5E+02	3.4E-07	5.8E+03
1998MAR26010714530900	-0.9	71	50	34	5.4E+07	5.1E+00	7.4E+00	1.4E-07	2.3E+03
1998MAR26024600669300	-0.6	60	50	61	1.4E+08	1.8E+01	2.9E+01	2.1E-07	3.5E+03
1998MAR26025641537600	-0.9	92	50	76	4.7E+07	7.1E+00	1.2E+01	2.5E-07	4.3E+03
1998MAR26025738770700	-0.6	73	100	86	1.2E+08	1.6E+01	3.7E+01	3.2E-07	5.4E+03
1998MAR26025740944500	-0.6	80	50	92	1.6E+08	4.5E+01	8.5E+01	5.5E-07	9.3E+03
1998MAR26042858924800	-0.5	78	50	55	1.8E+08	6.6E+01	1.1E+02	6.0E-07	1.0E+04
1998MAR26050248569600	-0.9	93	50	46	5.4E+07	9.4E+00	1.6E+01	3.0E-07	5.1E+03
1998MAR26050336364100	-0.4	53	50	61	2.8E+08	5.1E+01	8.5E+01	3.0E-07	5.1E+03
1998MAR26054150230300	-0.4	78	70	92	3.1E+08	1.6E+02	3.2E+02	1.0E-06	1.7E+04
1998MAR26061532231200	-0.5	79	50	86	2.1E+08	8.0E+01	1.6E+02	7.4E-07	1.3E+04
1998MAR26120638347200	-0.6	66	100	76	1.6E+08	3.8E+01	4.8E+01	3.1E-07	5.3E+03
1998MAR26120639979700	-0.5	77	50	46	1.7E+08	6.1E+01	9.2E+01	5.4E-07	9.1E+03
1998MAR26120644831300	-1.0	83	50	34	3.1E+07	2.9E+00	3.9E+00	1.3E-07	2.1E+03
1998MAR26125941299200	-0.4	59	50	55	3.2E+08	8.4E+01	1.5E+02	4.7E-07	8.0E+03
1998MAR26132817159400	-0.3	48	50	70	3.4E+08	6.6E+01	9.4E+01	2.8E-07	4.7E+03
1998MAR26150408648400	-0.7	80	85	104	1.0E+08	2.2E+01	3.8E+01	3.7E-07	6.2E+03
1998MAR26162640328000	-0.4	75	50	83	2.8E+08	1.2E+02	2.3E+02	8.2E-07	1.4E+04
1998MAR26162734354300	-0.6	67	30	31	1.1E+08	1.5E+01	2.6E+01	2.3E-07	3.9E+03
1998MAR26175324377600	-0.2	35	100	76	5.6E+08	7.4E+01	9.9E+01	1.8E-07	3.0E+03
1998MAR26181625404200	-0.5	76	50	46	1.8E+08	7.5E+01	1.1E+02	5.8E-07	9.8E+03
1998MAR26184914525500	-0.4	85	50	92	2.7E+08	1.3E+02	3.1E+02	1.1E-06	1.9E+04
1998MAR27095655471200	-0.2	88	50	76	5.4E+08	5.7E+02	1.4E+03	2.6E-06	4.4E+04
1998MAR27103238223100	-0.3	86	50	64	3.9E+08	2.7E+02	6.7E+02	1.7E-06	2.9E+04

TABLE 4.1: Source parameters for 42 mining induced seismic events at the Moonee Colliery. The source parameter estimates that are highlighted yellow are uncertain due to the uncertain recording sample rate. The estimates of the E_s/M_0 ratio and apparent stress are not affected by an uncertain recording sample rate (as discussed in the text). The estimates for the apparent stress were calculated using source parameter estimates based on the techniques offered by Andrews [1986]. Under the assumed technique, estimates for σ_B can be found by multiplying σ_a by ~4.265. (Note: Read 5.00E-05 as 5.00·10^{-5}).

Event (yyyyMMMddhhmmss.ssssss)	M_w	f_c (Hz)	Q	R (m)	M_0 (N·m)	Uncorrected E_s (J)	Corrected E_s (J)	E_s / M_0	σ_a (Pa)
1998MAR27111129919300	-0.2	57	70	64	5.6E+08	2.9E+02	4.2E+02	7.4E-07	1.3E+04
1998MAR27111132743500	-0.5	89	50	46	2.1E+08	1.5E+02	2.1E+02	1.0E-06	1.7E+04
1998MAR27112207037100	-0.1	64	100	177	8.7E+08	6.5E+02	1.4E+03	1.6E-06	2.7E+04
1998MAR27141258971300	-0.6	79	100	61	1.3E+08	4.5E+01	5.4E+01	4.3E-07	7.3E+03
1998MAR27145454606300	-0.1	74	50	76	8.7E+08	8.8E+02	2.1E+03	2.5E-06	4.2E+04
1998MAR27211435052400	-0.4	47	150	138	3.2E+08	5.0E+01	7.8E+01	2.4E-07	4.1E+03
1998MAR28051813895400	-0.8	83	50	92	6.4E+07	8.5E+00	1.6E+01	2.6E-07	4.3E+03
1998MAR30165753560900	-0.6	51	50	31	1.4E+08	1.4E+01	1.8E+01	1.3E-07	2.2E+03
1998MAR30172230084100	-0.3	48	50	61	3.7E+08	6.7E+01	1.0E+02	2.9E-07	4.8E+03
1998MAR30185027599900	-0.8	128	50	34	6.7E+07	3.7E+01	6.5E+01	9.7E-07	1.7E+04
1998MAR30191247136100	-0.8	87	50	40	6.4E+07	1.4E+01	1.8E+01	2.9E-07	4.9E+03
1998MAR30211500538400	-0.5	75	50	64	1.8E+08	5.5E+01	8.9E+01	5.1E-07	8.6E+03
1998MAR31082407160700	-0.8	51	50	31	6.4E+07	2.9E+00	3.9E+00	6.0E-08	1.0E+03
1998MAR31192713539700	-0.9	77	50	61	4.6E+07	3.7E+00	6.7E+00	1.5E-07	2.5E+03
1998MAR31195006216400	0.0	56	50	89	1.1E+09	7.1E+02	1.5E+03	1.4E-06	2.4E+04
1998MAR31212159282300	-0.7	94	50	95	1.1E+08	2.9E+01	7.2E+01	6.4E-07	1.1E+04

TABLE 4.1: [Continued] Source parameters for 42 mining induced seismic events at the Moonee Colliery. The source parameter estimates that are highlighted yellow are uncertain due to the uncertain recording sample rate. The estimates of the E_s/M_0 ratio and apparent stress are not affected by an uncertain recording sample rate (as discussed in the text). The estimates for the apparent stress were calculated using source parameter estimates based on the techniques offered by Andrews [1986]. Under the assumed technique, estimates for σ_B can be found by multiplying σ_a by ~4.265. (Note: Read 5.00E-05 as $5.00 \cdot 10^{-5}$).
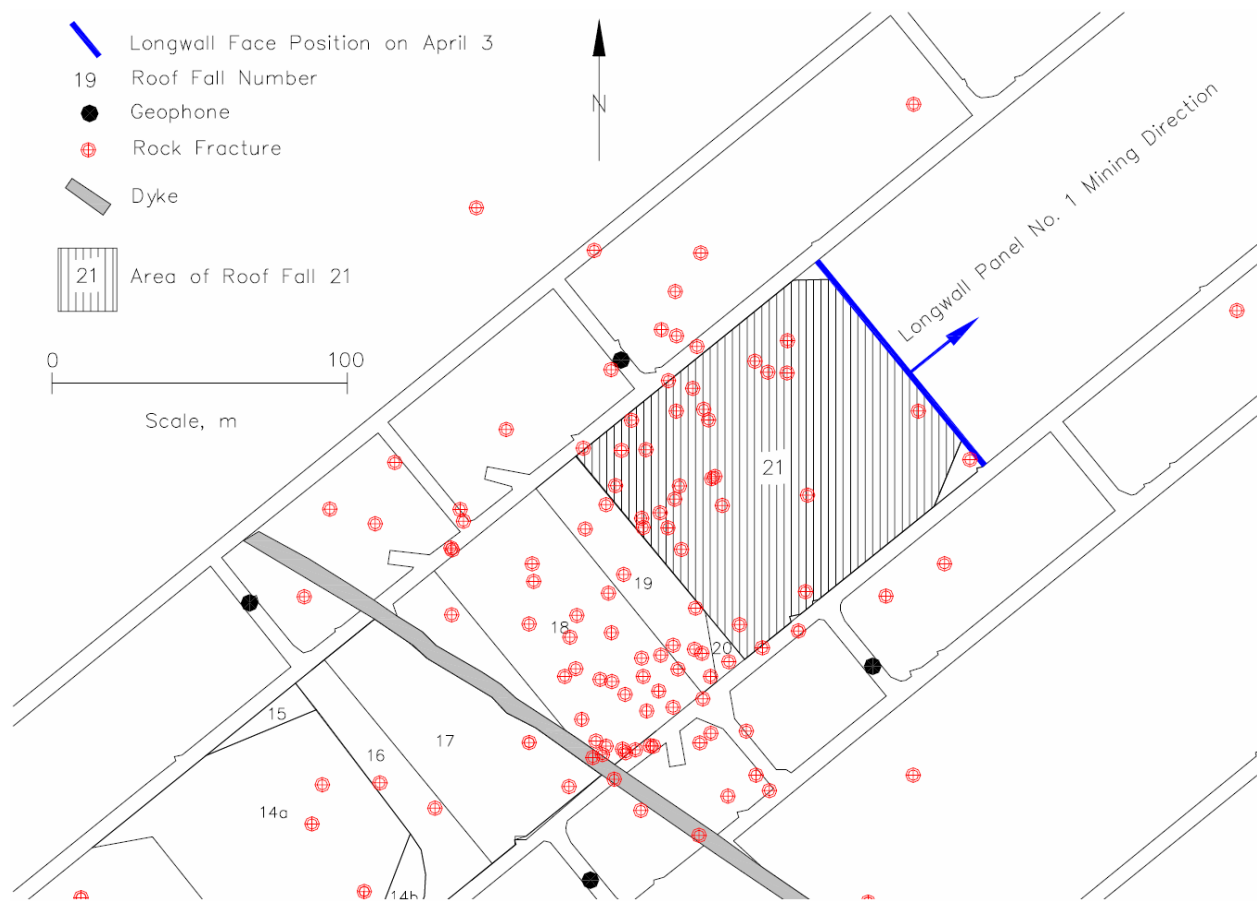
FIGURE 4.1: Location of the 4 three-component geophones (Black Dots) with respect to the location of the rock fracture events (Red Crosshairs) that were automatically located by the monitoring system at Moonee. This data set is composed of the events that led up to Roof Fall No. 21, indicated in the hashed area [from Iannacchione *et al.* (2005), used with permission].

Start (define):
- First Horizontal Component Array = H1
- Second Horizontal Component Array = H2
- Noise Window Begin Sample Point = NWB
- Noise Window End Sample Point = NWE
- Moving Window Length = MWL
- Signal to Noise Ratio Threshold = SNRT

- MAX = $-\infty$
- Angle Increment = $\Delta\theta$

- Rotation Angle (θ) = -45°

- **ROTATE** the 2 horizontal components by θ:

$$Radial_j = H1_j \cdot \cos(\theta) + H2_j \cdot \sin(\theta)$$
$$Transverse_j = H1_j \cdot (-\sin(\theta)) + H2_j \cdot \cos(\theta)$$

Where 'j' denotes the j'th sample point in the time series

- **COMPUTE** the average spectral power for the new Radial and Transverse components between the specified noise window range:
NWB ≤ j ≤ NWE

- **DETERMINE** the average spectral power within a moving window (of specified length MWL) that is applied over all possible locations inside the new Radial and Transverse time series. The locations of the moving window mid-points may be selected between the range:

MWL ≤ j ≤ (Last Sample Point in Series) – MWL
 2 2

such that there are an equal number of sample points on either side of the moving window mid-point.
- **COMPUTE** the ratio of the average spectral power between each moving window location and the fixed window for both components.
- **DEFINE** two arrays (SNrad and SNtrans) to store all the signal-to-noise ratio values for all possible sample points.
- **SAVE** each signal-to-noise ratio value at the sample point that corresponds to the mid-point of the moving window within each time series. For simplicity, the sample points that are outside of the above range may be defined as zero.

STOP (return):
Final Rotation Angle (Φ)

- **IF** the rotation angle is greater than 45°
  - **THEN** stop loop.
- **ELSE** continue loop.

- **INCREMENT** the Rotation Angle:
$$\theta = \theta + \Delta\theta$$

- **IF** the D is greater than the current value for MAX:
  - **THEN** MAX is equal to D and the final rotation angle to be used (Φ) is equal to the current rotation angle (θ).
- **ELSE** continue loop.

- **COMPUTE** the difference (D):
$$D = P_T - P_R$$

- **DETERMINE** the first sample point within the two arrays SNrad and SNtrans that exceeds the specified signal-to-noise ratio threshold (SNRT).
- **SAVE** the first radial and transverse sample point to exceed SNRT as P_R and P_T, respectively.

FIGURE 4.2: Flow-chart describing the process used to rotate the data into radial and transverse components.

Start (define):
- First Horizontal Component Array = H1
- Second Horizontal Component Array = H2
- Moving Window Length = MWL

• **DETERMINE** the amplitudes within a moving window (of specified length MWL) that is applied over all possible locations inside the Radial, Transverse and Vertical time series. The locations of the moving window mid-points may be selected between the range:

$$\frac{MWL}{2} \leq j \leq (\text{Last Sample Point in Series}) - \frac{MWL}{2}$$

such that there are an equal number of sample points on either side of the moving window mid-point.

• **COMPUTE** the eigenvalues of the matrix **M** for each moving window location within the above specified range in 'j' (where λ_0, λ_1 and λ_2 represent the smallest, intermediate and largest eigenvalue of **M**):

$$\mathbf{M}^{<j>} = \sum_{k=j-\frac{MWL}{2}}^{j+\frac{MWL}{2}} \begin{bmatrix} radial_k \cdot radial_k & radial_k \cdot transverse_k & radial_k \cdot vertical_k \\ transverse_k \cdot radial_k & transverse_k \cdot transverse_k & transverse_k \cdot vertical_k \\ vertical_k \cdot radial_k & vertical_i \cdot transverse_k & vertical_k \cdot vertical_k \end{bmatrix}$$

$$\text{Eigenvalues}(\mathbf{M}^{<j>}) = \begin{pmatrix} \lambda_0^{<j>} & \lambda_1^{<j>} & \lambda_2^{<j>} \end{pmatrix}$$

• **COMPUTE** the Rectilinearity and Planarity at each mid-point in 'j' based on the eigenvalues computed at each mid-point in 'j':

$$\text{Rectilinearity}_j = \frac{(\lambda_0^{<j>} + \lambda_1^{<j>})}{2 \cdot \lambda_2^{<j>}}$$

$$\text{Planarity}_j = \frac{(\lambda_2^{<j>} - \lambda_1^{<j>})}{(\lambda_2^{<j>} - \lambda_0^{<j>})}$$

• **SAVE** all sample points outside of the range in 'j' as zero, for simplicity.

STOP (return):
Rectilinearity
And
Planarity

FIGURE 4.3:   Flow Chart describing the process for determining the Rectilinearity and Planarity of the radial, transverse and vertical time series.

FIGURE 4.4: Examples of a rotated time series (Radial = red, Transverse = blue and Vertical = green) plotted against the individual signal-to-noise ratio for each component (light blue) as well as the polarization parameters (Rectilinearity = pink and Planarity = brown). All of the parameters provided various characteristics that were used to pick the P-wave arrival time (Top) and the S-wave arrival time (Bottom) based one maximizing the P-wave on the radial component.
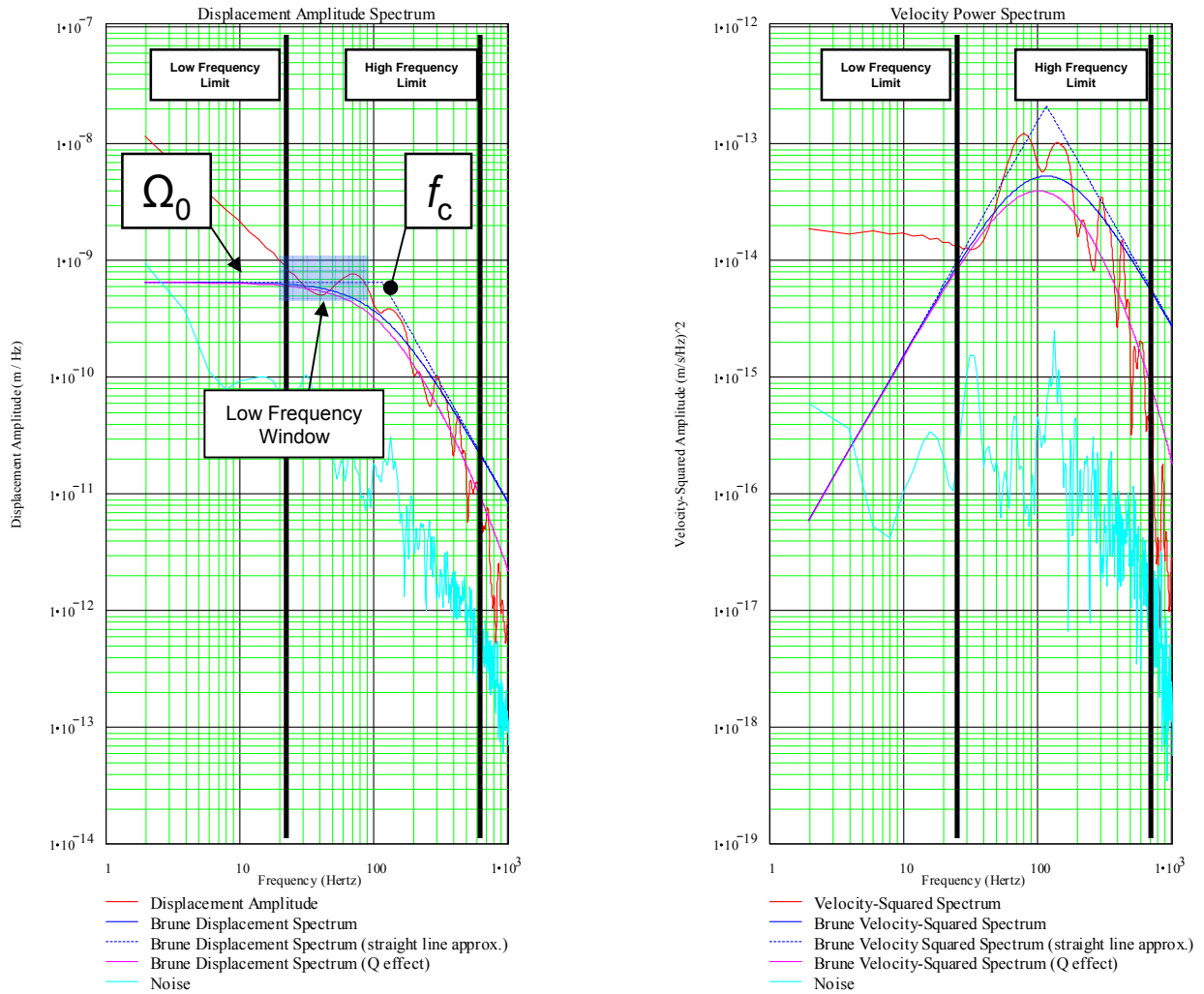
FIGURE 4.5: Displacement Spectra (Left) and Velocity-Squared Spectra (Right) used to visually confirm the initial estimates of Zero-Frequency Displacement Amplitude (Ω_0), Corner Frequency (f_c), and Quality Factor (Q). The solid (and dashed) blue lines represent the theoretical Brune source spectra (and the Hanks and Thatcher spectral approximation) based on the estimates of Ω_0 and f_c. The solid pink line also represents the theoretical Brune source spectra based on the estimates of Ω_0 and f_c, while also taking into account the effect of T^* ($= R / (\beta \cdot Q)$). In addition, the low frequency and high frequency bandwidth limits were estimated for future integral calculations (the methods for finding these limits are explained in the text).
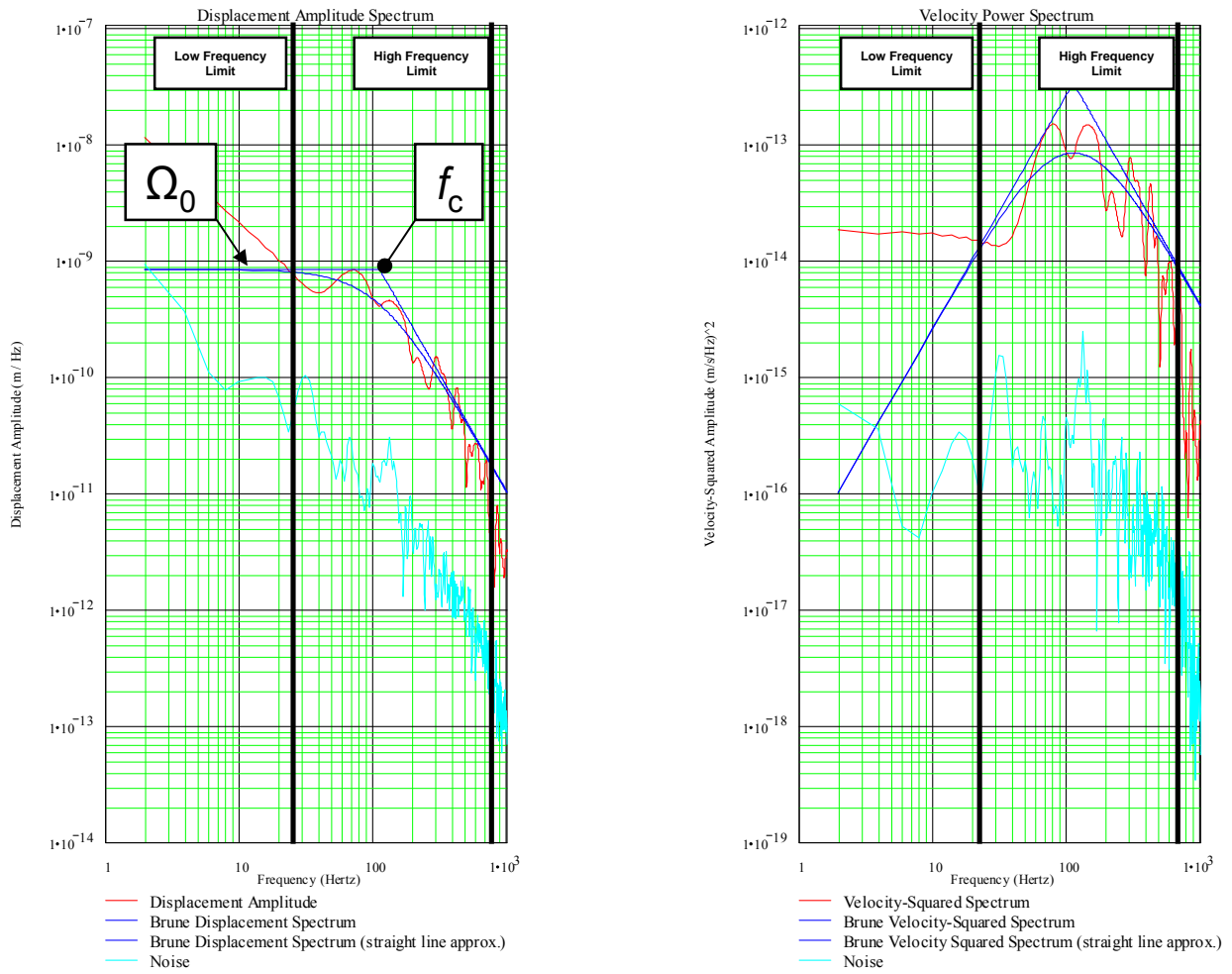
FIGURE 4.6: The result of correcting the spectra from Figure (4.5) for the effects of T^*. It should be noted that there is now a better fit between the various source spectra and the Brune theoretical source spectra between f_{min} and f_{max}.
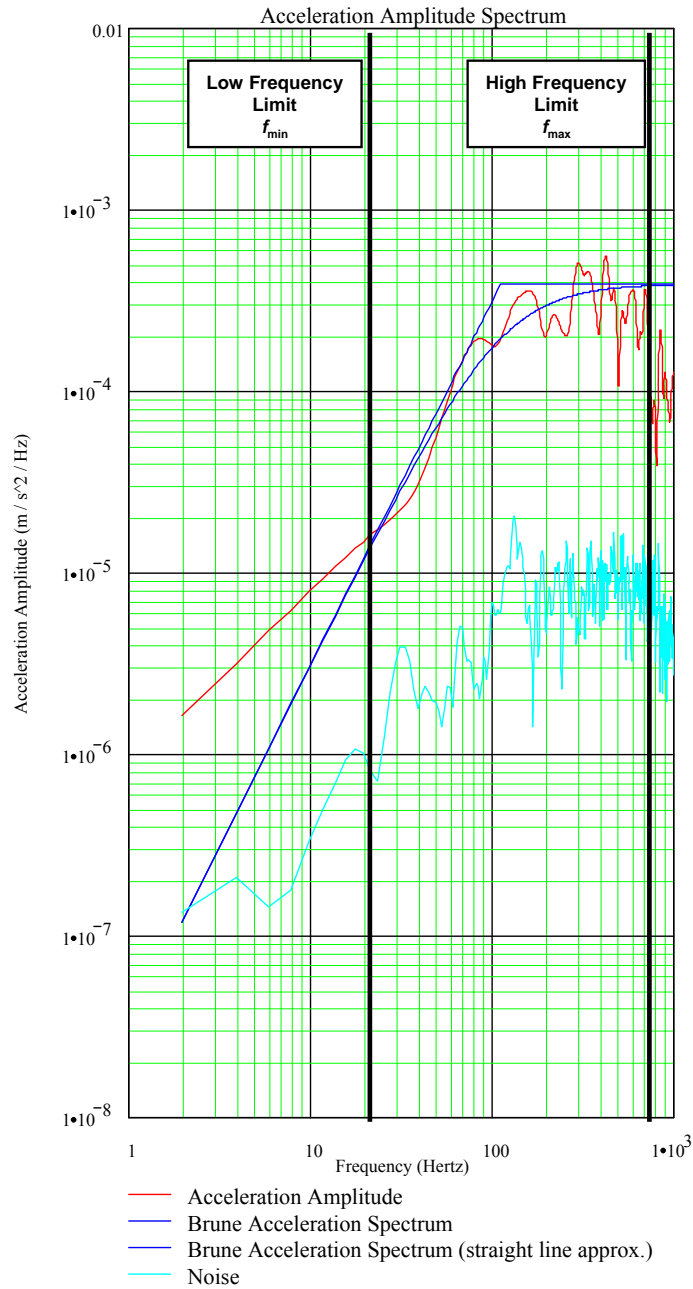
FIGURE 4.7: Acceleration Amplitude Spectra after correcting for the Attenuation and the Bandwidth Limitations. The Acceleration Spectra aids in identifying the high frequency limit of the signal (f_{max}) and the low frequency limit of the signal (f_{min}) by visual inspection. The observed f_{max} for the Moonee events were typically between 500 and 700 Hertz.

Comparison Between Radiated Seismic Energy and Seismic Moment Estimates
(Final Results Uncorrected and Corrected for Attenuation and Limitations in Bandwidth)
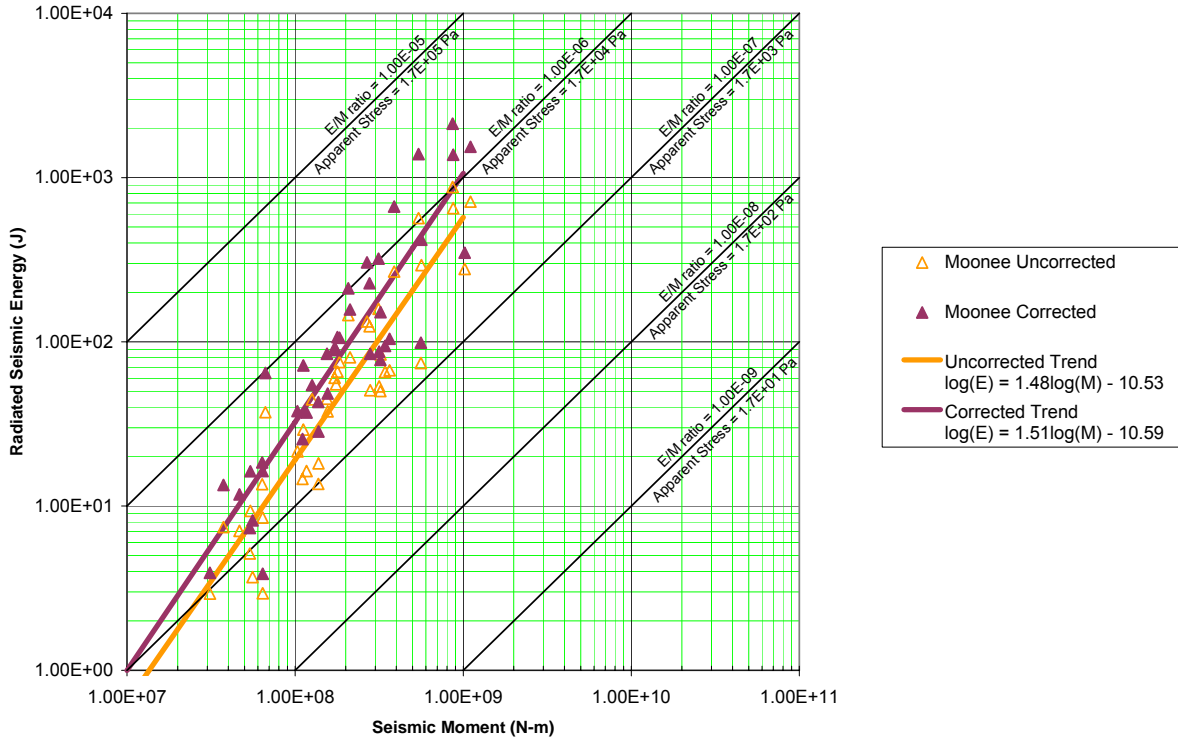
FIGURE 4.8: Uncorrected values (orange triangles) and corrected values (maroon triangles) of the Radiated Seismic Energy versus the Seismic Moment for 42 events from the Moonee Data Set. The results for this data set correspond to estimates in the Seismic Moment and the Radiated Seismic Energy that range from $3 \cdot 10^7 - 1 \cdot 10^9$ N·m and $3.0 - 2 \cdot 10^3$ J, respectively. Equivalently, the Moment Magnitude range lies between -1.0 and 0.0. Lines of constant Apparent Stress and constant Energy to Moment ratio are also plotted, where our assumed material properties lead to a value of $1.7 \cdot 10^{10}$ Pa for rigidity (μ).
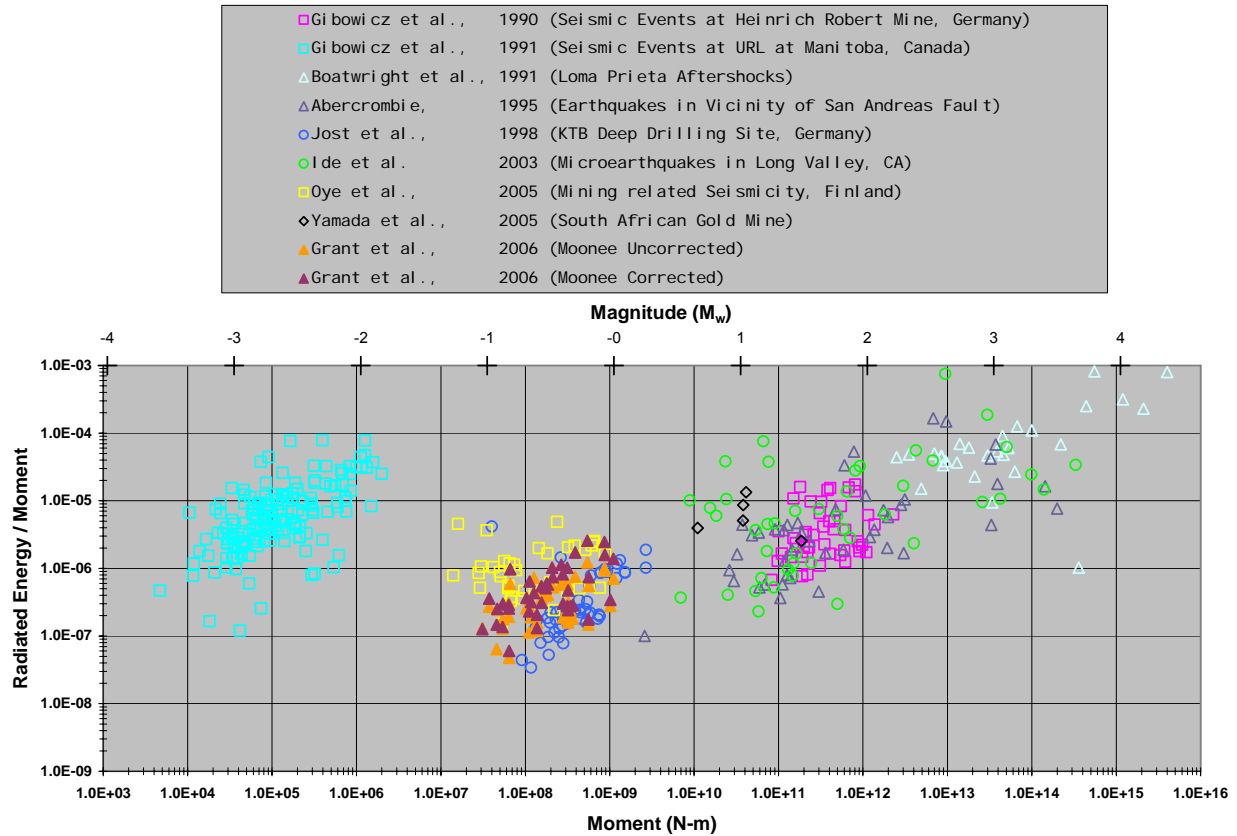
FIGURE 4.9: Final estimates of the ratio between the Radiated Seismic Energy and the Seismic Moment versus the Seismic Moment. An important note regards the relative insignificance in correcting our data for the effects of the bandwidth limitations and propagation path.

Chapter 5: Springfield Pike Quarry Data Set

Data obtained from the Springfield Pike Underground Limestone Quarry (Figure 5.1 and 5.2) consist of seismic events that occurred within 35 to 580 meters of twelve stations (three-component sensors recording in single-component configuration at 1926 samples per second) that made up a portion of the seismic monitoring system at Springfield Pike . The sensors were mounted (strapped) underground to the surface of the roof, which consisted of approximately 2 meters of limestone overlain by alternating layers of weak shales and sandstones. The single component recorded motion that was horizontally polarized in the North-South direction. The hypocentral locations of the seismic events were determined by NIOSH researchers in work conducted prior to this study.

5.1   Mining Operations and Roof Failure Process at Springfield Pike

Underground mining operations at Springfield Pike take place within the Loyalhanna Limestone, which is approximately horizontal and is ~10.0 meters thick in the vicinity of the mining operations. The mining method at Springfield Pike is room-and-pillar, where over 50% of the limestone layer is left in place as either vertical support or roof support (Figure 5.3). The orientation of the regional tectonic stresses and the geological location of the mine have contributed to produce an anomalously large horizontal stress field measured between 15 and 55 MPa [Iannacchione *et al.* (2005b)]. Figure (5.1) shows the mine workings in plan view along with the orientation of the horizontal compressive stress. To mitigate the effects of the high horizontal stress field, ~2.0 meters of the limestone layer is typically left in place to support the roof spanned between each column. In general, the roof and column design is such that stability is maintained throughout the underground mine. Only in very rare circumstances do the stress concentrations become large enough to induce failure in the roof strata.

The roof failure process at Springfield Pike is classified as "progressive" by Iannacchione *et al.* [2005b], where the occurrence of a single roof collapse would often lead to the progressive failure of adjacent roof strata. The differences in material strength between the limestone layer and the overlying weaker strata in the roof may have also had a significant influence on the failure process.

Figure (5.4) outlines the idealized failure process at Springfield Pike. Here, the horizontal stress field that was originally distributed through out the entire ~10 meters of limestone (Figure 5.4a) becomes significantly concentrated in the ~2 meters thick limestone in the immediate roof after the excavation of material (Figure 5.4b). In Figure (5.4c), we idealize the horizontal layer of limestone as a beam. Under this assumption, the application of a compressive load along the longitudinal axis of the beam initiates a shear crack along the bottom of the beam (Cartoon: Figure 5.4c *green line in top beam*; Real Example: illustrated in Figure 5.5). As the beam compresses, it accumulates strain and the shear crack propagates at a low angle through the beam. If a significant amount of residual compression exists or if the beam is re-loaded from the failure of adjacent strata, the low-angle shear will grow until it spans the idealized beam. Further loading of the beam will cause the beam to dislocate along the shear face (Figure 5.4c *solid green line*). This causes a change in the idealized view of this problem from one fixed beam to

two cantilevering beams. Once the beams begin to cantilever, a tensile crack initiates (Figure 5.4c *red line in middle beam*) and propagates due to loads that cannot be supported. These loads come from the combined effects of the overburden pressure, level of deformation in the material directly above the beam, and potentially from the moment about the tensile crack induced by the dislocation between the two beams along the shear face. These loads ultimately contribute to the total effective bending moment about the tensile crack. Once the tensile crack spans the beam, we assume that the beam completely detaches from the rest of the roof and the failure process associated with the individual beam is concluded. Note in Figure (5.4c) that as the beam accumulates strain and begins to deform, the residual amount of compressive stresses begin to reduce (i.e. the stresses associated with this beam reduce unless failure of adjacent strata redistribute loads onto this beam). Progressive failure of this kind continues until the roof reduces to a sufficient state of static equilibrium. This typically results in a roof cavity that takes the shape of the inside of a half-paraboloid (Figure 5.6). A roof failure less than a few percent of the size illustrated in Figure (5.6) poses a significant health risk. There is motivation (for at least part of this study) to determine whether it is possible to forecast episodes of roof failure by seismically monitoring rock fracture seismic emissions and determining whether the events are indicative of an imminent roof collapse.

5.2   Data Processing Procedure

Estimation of the apparent stress was carried out using a program developed in MathCAD. The data obtained from the underground system were not instrument corrected. Therefore, the instrument response was removed prior to any analysis. Rotation and Polarization analysis [similar to Jepsen and Kennett (1990)] of the velocity data were not possible due to the lack of three-component recordings for each station. Instead, only the signal-to-noise ratio and earlier estimates of the hypocentral distances from each station were used to aid in estimating the P-wave and S-wave phase arrival times. An appropriate window size, depending on the duration of the signal, was used to extract the S-wave portion of the signal.

The analysis procedure for these events was similar to that used for the Moonee data set. The forward Fourier transform (using Equation 2.14) of the S-wave window (Figure 5.9) within the velocity time series was computed. The displacement and acceleration amplitude spectra were subsequently determined by dividing or multiplying, respectively, each amplitude from the velocity spectrum by omega ($\omega = 2\pi f$). The displacement spectra (Figure 5.10) were used to estimate the zero-frequency displacement amplitude (Ω_0), the corner frequency (f_c) and the approximate value of (T^*) needed to correct the high frequency amplitudes for propagation effects based on the assumption of the Brune model (the corrected spectra are illustrated in Figure 5.11). The majority of the seismic events analyzed for Springfield Pike did not have spectral shapes that *consistently* conformed well to the Brune model. The overall shape was typically in agreement, but in most circumstances there were significant gaps in the Fourier amplitude spectra in the vicinity of the corner frequency. Therefore, since we did not use a spectral smoothing tool, it did not seem appropriate to use the techniques offered by Andrews [1986] to estimate the spectral parameters (Ω_0 and f_c), because the basis for his estimates assumed that the Fourier amplitude spectra were *consistently* well constrained by the Brune model over the entire data bandwidth. The occasional gaps in the spectral amplitudes would lead

to estimates of the spectral parameters that would be inconsistent with what an analyst would pick. Initial and final estimates of the zero-frequency displacement amplitude, corner frequency and quality factor were made by visually determining the best fit Brune spectrum for the parts of the spectrum that did appear to conform to the Brune model. As mentioned in the previous chapter, the method of calculating Ω_0 was such that reasonable estimates of the low-frequency window, in terms of picking ν_1 and ν_Ω as outlined in Section (2.5.2), led to variance in the estimate for Ω_0 that did not exceed $\pm 10\%$.

The upper and lower frequency limits of integration were identified after correcting the various source spectra using Equation (2.15), where the upper limit was typically identified by examining the acceleration spectra (Figure 5.12). Although the majority of the source spectra for the events at Springfield Pike did not conform well to the Brune model, we still used the same correction factors for the integral of the velocity-squared spectrum explained in Equation (2.18) to account for the limitations in bandwidth. It was assumed that using these correction factors for this data set would offer an upper bound on the integral of the velocity-power spectra, since these correction factors assume the source spectra conform well to Brune's theoretical spectra.

5.3 Uncertainty due to Single-Component Recordings, Source Radiation Pattern Terms and Material Properties

Uncertainties in this data set include the effects of single component recordings vs. three-component recordings, radiation patterns for the events, and the average velocity / density of the rock between each event and station. It is less favorable to base the estimates of the radiated seismic energy and the seismic moment on single component recordings. However, these estimates (at the very least) provide a lower bound approximation to the estimates made had there been three-component recordings. Figure (5.13) illustrates an empirical comparison of the source parameter estimates made using a single component of motion versus using all three components of motion for the Moonee data of Chapter (4). The results from the Moonee data set suggest that the estimates of the radiated seismic energy and seismic moment based on a single component of horizontal motion were smaller than the estimates made by three component recordings by a factor that did not exceed 5.0. In addition, the estimates of the E_s/M_0 ratio based on a single component of horizontal motion were smaller than the estimates made by three component recordings by a factor that did not exceed 2.0. We are led to assume that the single component based estimates at Springfield Pike may not be significantly in error because of the empirical relationships between single component and three component based estimates from the Moonee data set. It might be possible to determine an appropriate scaling factor for each of the estimates if the radiation pattern of the events were well constrained. However, we did not feel that the data were of good enough quality, with regard to polarity picks, to estimate the radiation pattern term for each event. Instead we assumed the radiation pattern terms were equal to the RMS radiation pattern terms, after Aki and Richards [2002], pg. 115. We assume a density of 2650 kilograms per cubic meter and, similar to the Moonee data, two sets of P-wave and S-wave velocities ($\alpha = 5500$ [4900] and $\beta = 3200$ [2900]) that are approximately consistent with a Poisson solid (Poisson ratio = 0.25 and $\alpha / \beta = \sqrt{3}$). The estimates for the seismic moment and the radiated seismic energy using each velocity set were averaged to make the final results plotted in Figures (5.15) and (5.16).

5.4   Effect of the Recording Conditions on the Estimates of the Seismic Moment and Radiated Seismic Energy

Mounting the instruments directly to the surface of the roof (or any free surface) is not a practical means of recording seismic events with the intent in performing the type of analysis done in this study because of the high potential for the direct body-wave energy to be contaminated with surface wave energy shortly after the direct S-wave arrival. It is very important that the surface wave energy is not included in calculations of the seismic moment and radiated seismic energy. For one, the spectral shape of the signal in the frequency domain may not be well fit by a Brune spectral shape and two, the estimates of the seismic moment and radiated seismic energy for the event may be significantly in error. For the stations that are located relatively close to the seismic events, the Rayleigh wave arrival occurs just after the S-wave arrival. For example, if an instrument (recording at 1926 samples per second) is mounted to the surface of the roof and located 50 meters from a seismic event, the time difference between the Rayleigh wave and S-wave arrival is ~2 milliseconds (corresponding to ~4 samples). This is hardly enough signal to characterize the seismic moment and radiated seismic energy of a seismic event using the type of spectral analysis done in this study. Another disadvantage pertains to the composition of the roof. If the roof is composed of a variety of layered strata, which is the case at Springfield Pike, there is a significant potential for scattering to occur.

The first arrivals of energy from each event consisted of P-waves that do not appear to suffer from scattering or any contamination from the slower surface waves. For the purposes of this study, this allowed for sufficient estimates of the event hypocenter based on the first arrival times. Shortly after the direct P-wave arrivals, however, the motion recorded by the stations was often contaminated with back-scattered body wave energy as well as the direct surface wave energy and reflections of the surface wave energy from the various contacts between the roof and pillars. However, for nearly all the roof fracture and roof failure events, station GN04 (circled in Figure 4.2) provided clean P- and initial S-wave signals while showing little or no evidence of any contribution from either the surface wave energy or the roof-failure-induced air-blasts (evident in Figure 5.7). For this reason we used the data from station GN04 for all the source estimate calculations (i.e. radiated seismic energy, seismic moment, and apparent stress).

Spectral peaks similar to those illustrated in Figure (5.14), at approximately 400 and 625 Hertz, were observed for nearly all the stations (including GN04). Our interpretation of these curious spectral peaks involves possible resonant frequencies associated with the 2.0 meter thick layer of limestone. The P-wave and S-wave velocities of the limestone were estimated in a prior study [Iannacchione *et al.* (2005b)] to be approximately 5000 and 3200 meters per second, respectively. If we simply view the motion as due to vertically propagating plane waves within a horizontally layered roof, the velocity and thickness of limestone produces a fundamental resonant frequency that closely matches the spectral peaks illustrated in Figure (5.14), and to some degree Figures (5.10 − 5.12). Here we assume for simplicity vertical P- and S-wave propagation within the layered roof: in that case, the fundamental resonance (F_r) of the limestone layer is given by $F_r = \upsilon/4h$, where υ is P or S velocity and *h* is layer thickness.

Figure (5.14) shows the largest spectral peaks of any record in this data set (other events showed peaks at approximately the same frequencies, but with smaller amplitudes). We speculate that the signal amplitude may be related to the proximity of the fracture event with respect to the 2.0 meter thick layer of limestone that comprises the immediate roof. Deconvolution of the assumed source spectral shape (i.e. the best fit Brune model) from the observed Fourier amplitude spectra results in virtually no change in the wave form of the signal in the time domain (when scaled properly). This result suggests that the "ringy" nature of the signal may potentially be an artifact of the wave propagation effects, instead of a source effect (e.g. tremor-like source function). The reason why this energy essentially remained trapped within the layer of limestone remains unclear. Significant impedance contrasts either above or below the layer of limestone provide some physical credibility for this hypothesis. The contact between the air and the face of the layer of limestone creates a large impedance contrast. Above the 2.0 meter thick layer of limestone, however, alternating layers of weak claystones, shales, siltstones and thin sandstones do not offer the same level of contrast. In normal conditions, where there are no anomalously high levels of stress acting parallel to the layers of strata, the impedance contrast between the limestone and the other possible varieties of layered rock might not be significant enough to trap energy within the limestone layer. However, conditions where high levels of lateral stress do exist present the opportunity for the contacts between the limestone layer and the layer of rock immediately above to detach enough that high impedance contrasts may exist both above and below the limestone layer.

Another interesting observation is the high-frequency limit (f_{max}) in the signal. In addition to the observation of the spectral peaks, the spectral amplitudes for the majority of the events also display a tendency to decrease abruptly at frequencies greater than the first resonance peak, 400 Hertz. We conjecture that the fundamental mode in the layer of limestone is excited and somehow de-couples the instrument, thereby filtering out source-generated high frequencies.

5.5 Discussion of the Results for Springfield Pike

The results obtained after processing 64 events from the Springfield Pike data set are tabulated in Table (5.1). The relationship between the radiated seismic energy and seismic moment is illustrated in Figures (5.15) and (5.16). The uncorrected estimates (orange triangles) and the corrected estimates (maroon triangles) of the radiated seismic energy are plotted against the estimates of the seismic moment in Figure (5.15). The estimates of the radiated seismic energy range between $2 \cdot 10^{-3}$ and 30 J, while the estimates of the seismic moment range between $3 \cdot 10^{5}$ and $1 \cdot 10^{8}$ N·m. A least squares fitting scheme for logarithmic data was used to determine the overall trend of the uncorrected and corrected data (also plotted in Figure 5.15). The least-squares fits computed for the uncorrected data ($\log(E_S) = 1.39 \cdot \log(M_0) - 10.60$) and the corrected data ($\log(E_S) = 1.34 \cdot \log(M_0) - 9.87$) are very similar, and indicate that the uncorrected results shifted up by a nearly constant factor of ~2 after making the corrections for the propagation effects and the bandwidth limitations. Also plotted in Figure (5.15), are lines representing constant E_s/M_0 ratio. The difference between the trend made by the corrected results and the trends of constant E_s/M_0 ratio indicates that the apparent stress is not constant for the events at Springfield Pike. Instead the apparent stress appears to increase with seismic moment in a manner similar to that found by our Moonee results and that reported by many previous studies.

The estimated E_s/M_0 ratio for the events at Springfield Pike and the events associated with eight other data sets are plotted in Figure (5.16). As indicated in Figure (5.15), we found that T^*-and-bandwidth corrections had little or no effect on the observed trend of increasing E_s/M_0 ratio with increasing seismic moment for the Springfield Pike results (See the maroon and orange triangles in Figure 5.16). The T^*-and-bandwidth corrections generally resulted in a constant increase in E_s/M_0 ratio no larger than a factor of 2. These results are similar to the results obtained from the Moonee data set.

5.6   Possible Temporal Changes in the Seismic Moment and Apparent Stress Prior to Roof Falls

This particular data set consists of ~13 inferred roof fall events that took place during a three-hour time period. The 13 roof fall events were inferred on the basis of recorded air blast signals. The air blast signals feature significantly different move-outs across the Springfield Pike seismic network compared to move-outs of the seismic signals that traveled through rock (see Figure 5.7 and 5.8). We believe the air blasts are due to the displacement of air throughout the mine void caused by the release of material from the roof. The inferred roof falls and the large number of seismically observed (and analyzed) rock fracture events associated with the roof falls offers the opportunity to study the seismic moment and apparent stress relationship in the time interval leading up to a roof fall. This is a potentially important area of research.

Figure (5.17) plots the radiated seismic energy, seismic moment, and E_s/M_0 ratio (which is proportional to apparent stress) of the rock fracture events along with the inferred occurrence of roof falls. The estimate of the relative size of each roof fall is based on the peak air-blast-induced velocity recorded by the nearest roof-mounted station (Green dashed line in Figure 5.7). The estimate of the duration of the air-blast coda recorded for each air-blast event is shown as the solid Red line in Figure (5.7), where the observed amplitude decay shape is a function of the volume of material involved in the fall. It is possible that an initial collapse of material could be followed through time by a progressively smaller amount of collapsed material, further increasing the duration of the air blast signal.

Figure (5.17) appears to indicate that both the E_s/M_0 ratio of the seismic events and the seismic moment increase in the time interval leading up to several inferred roof fall events. The time intervals in some cases span tens of minutes, whereas others only appear to span a few seconds. Figures (5.18) and (5.19) show examples of events just before a roof collapse that demonstrate an increase in the E_s/M_0 ratio and seismic moment leading up to roof collapse events through time intervals that apparently last only a few seconds.We hypothesize that the variability in the amount of time required for the failure process to evolve to the point of a roof fall depends upon the rate at which the roof strata are loaded. This rate could also depend upon the amount of pre-fractured or pre-failed strata in the rock mass, in which a larger percentage of pre-fractured or pre-failed strata may, in principle, lead to a significantly smaller time interval necessary to initiate and complete the roof failure process.

The observation of increasing apparent stress and seismic moment with time prior to the roof fall is equivocal, because only a few examples are available and the trends in the data suggesting a time dependent pattern are only marginally significant. However, if the data are

representative of a consistent pattern of behavior, the observation has important implications for the failure process. This will be discussed further in following chapter (Chapter 6).

| Event	Relative Time (min)	M_W	f_c (Hz)	Q	R (m)	M_0 (N·m)	Uncorrected E_S (J)	Corrected E_S (J)	E_S / M_0	σ_a (Pa)
00022090	0	-1.8	90	100	135	2.6E+06	5.0E-03	1.2E-02	4.5E-09	1.1E+02
00022093.A	4.45	-1.1	80	100	191	2.5E+07	6.9E-01	1.2E+00	4.6E-08	1.1E+03
00022093.B	4.55	-1.2	70	100	191	2.1E+07	3.0E-01	6.5E-01	3.1E-08	7.6E+02
00022096	4.977	-1.4	63	100	153	9.6E+06	3.8E-02	5.6E-02	5.8E-09	1.4E+02
00022098.A	7.078	-1.4	63	100	173	9.1E+06	3.5E-02	5.3E-02	5.8E-09	1.4E+02
00022098.B	7.178	-1.0	67	100	193	3.1E+07	2.1E-01	5.7E-01	1.9E-08	4.6E+02
00022099	8.347	-1.8	180	100	173	2.0E+06	1.7E-02	7.1E-02	3.6E-08	8.9E+02
0002209D	18.805	-1.1	50	500	194	3.0E+07	2.7E-01	3.0E-01	9.9E-09	2.5E+02
0002209J	27.396	-1.2	90	100	191	2.0E+07	2.9E-01	4.9E-01	2.5E-08	6.1E+02
0002209N	31.899	-1.6	200	100	203	3.8E+06	1.1E-01	5.0E-01	1.3E-07	3.2E+03
0002209O	34.885	-1.8	200	100	202	2.3E+06	1.3E-02	5.3E-02	2.3E-08	5.7E+02
0002209T	35.867	-1.9	200	300	206	1.8E+06	4.1E-02	1.2E-01	6.5E-08	1.6E+03
000220A6	39.62	-1.5	200	500	194	7.4E+06	6.7E-01	1.7E+00	2.3E-07	5.7E+03
000220AN	49.536	-1.3	120	100	207	1.2E+07	1.6E-01	4.8E-01	4.1E-08	1.0E+03
000220AU	55.353	-1.6	120	200	193	4.6E+06	5.1E-02	1.0E-01	2.2E-08	5.4E+02
000220AV	56.132	-1.2	120	150	173	1.5E+07	3.8E-01	9.3E-01	6.0E-08	1.5E+03
000220AW	57.203	-1.6	120	150	192	4.2E+06	3.3E-02	1.2E-01	2.8E-08	7.0E+02
000220AX	58.145	-1.0	80	50	180	4.0E+07	7.4E-01	3.1E+00	7.6E-08	1.9E+03
000220B5	69.708	-1.3	85	100	174	1.5E+07	1.6E+00	4.6E-01	3.1E-08	7.6E+02
000220B6.A	70.396	-2.2	145	200	167	6.8E+05	4.8E-03	8.7E-03	1.3E-08	3.2E+02
000220B6.B	70.39	-1.9	125	200	167	1.7E+06	3.6E-03	6.3E-03	3.6E-09	8.9E+01
000220B6.C	70.41	-1.7	200	200	167	2.8E+06	5.6E-02	7.9E-02	2.9E-08	7.0E+02
000220B6.D	70.51	-1.3	180	150	167	1.2E+07	4.0E-01	1.3E+00	1.0E-07	2.5E+03
000220B6.E	70.55	-1.7	130	150	167	3.0E+06	2.2E-02	4.1E-02	1.4E-08	3.4E+02
000220BB.A	72.61	-0.9	80	100	170	4.3E+07	8.1E-01	2.9E+00	6.7E-08	1.7E+03
000220BB.B	72.71	-0.8	70	100	170	6.8E+07	4.3E+00	6.4E+00	9.4E-08	2.3E+03
000220BF.A	73.367	-1.7	90	500	153	3.5E+06	1.1E-02	2.2E-02	6.3E-09	1.6E+02
000220BF.B	73.467	-1.6	110	500	153	5.2E+06	3.6E-02	6.9E-02	1.3E-08	3.3E+02
00022100	79.498	-1.7	180	100	177	2.9E+06	3.1E-02	1.7E-01	5.8E-08	1.4E+03
00022103.A	80.807	-1.4	60	100	148	9.4E+06	4.9E-02	8.6E-02	9.2E-09	2.3E+02
00022103.B	80.85	-1.1	90	100	148	2.3E+07	5.5E-01	1.4E+00	6.0E-08	1.5E+03
00022103.C	80.893	-0.9	70	100	148	4.7E+07	1.4E+00	3.4E+00	7.3E-08	1.8E+03
00022103.D	80.936	-1.0	80	100	148	3.5E+07	9.0E-01	2.6E+00	7.5E-08	1.9E+03

TABLE 5.1: Source parameters for 64 mining induced seismic events at Springfield Pike.
Read 5.00E-05 as $5.00 \cdot 10^{-5}$.

| Event	Relative Time (min)	M_W	f_c (Hz)	Q	R (m)	M_0 (N·m)	Uncorrected E_S (J)	Corrected E_S (J)	E_S / M_0	σ_a (Pa)
00022106	81.679	-1.6	220	100	148	4.2E+06	1.1E-01	2.9E-01	6.9E-08	1.7E+03
0002210E.A	83.767	-2.2	230	300	161	6.7E+05	4.3E-03	1.9E-02	2.8E-08	7.0E+02
0002210E.B	83.867	-2.2	150	500	161	5.3E+05	2.6E-03	4.9E-03	9.3E-09	2.3E+02
0002210E.C	83.967	-2.0	160	100	161	1.1E+06	8.7E-03	2.2E-02	1.9E-08	4.8E+02
0002210I	85.651	-1.8	92	150	187	2.0E+06	5.6E-03	1.1E-02	5.6E-09	1.4E+02
0002210T	90.168	-1.4	85	500	196	9.5E+06	1.5E-01	2.1E-01	2.2E-08	5.4E+02
0002210X	92.588	-1.5	120	500	188	6.0E+06	8.0E-02	1.5E-01	2.5E-08	6.1E+02
0002210Y	93.601	-1.6	150	150	203	4.0E+06	2.4E-02	7.6E-02	1.9E-08	4.7E+02
00022115	98.953	-1.7	73	100	194	2.9E+06	6.8E-03	1.7E-02	5.7E-09	1.4E+02
0002211F.A	103.6105	-1.6	120	50	173	4.6E+06	5.1E-02	1.8E-01	3.9E-08	9.6E+02
0002211F.B	103.6164	-1.4	125	50	173	8.6E+06	1.2E-01	4.8E-01	5.6E-08	1.4E+03
0002211F.C	103.6814	-1.5	70	50	173	7.3E+06	7.1E-02	2.0E-01	2.7E-08	6.7E+02
0002211F.D	103.7214	-1.5	100	50	173	6.4E+06	4.0E-02	1.2E-01	1.8E-08	4.5E+02
0002211F.E	103.7297	-1.2	100	50	173	1.7E+07	2.3E-01	1.0E+00	6.1E-08	1.5E+03
0002211F.F	103.7422	-1.2	100	50	173	1.9E+07	3.5E-01	1.1E+00	5.6E-08	1.4E+03
0002211F.G	103.748	-1.2	100	200	173	1.7E+07	7.9E-01	1.1E+00	6.4E-08	1.6E+03
0002211F.H	103.7564	-1.3	110	200	173	1.2E+07	3.2E-01	1.0E+00	8.3E-08	2.1E+03
0002211H	103.899	-0.7	100	150	222	9.2E+07	7.1E+00	2.4E+01	2.6E-07	6.4E+03
0002211O	106.403	-2.0	230	500	172	1.1E+06	1.9E-02	4.8E-02	4.2E-08	1.1E+03
0002211S.A	108.699	-1.1	90	500	210	2.3E+07	3.3E-01	8.6E-01	3.7E-08	9.0E+02
0002211S.B	108.8	-1.7	90	500	210	3.8E+06	9.2E-03	1.4E-02	3.6E-09	8.9E+01
0002211S.C	108.901	-1.8	150	500	210	2.0E+06	9.9E-03	1.8E-02	8.7E-09	2.1E+02
0002211Y	111.64	-1.1	60	200	200	2.6E+07	3.7E-01	6.3E-01	2.4E-08	5.9E+02
00022128	116.604	-1.6	100	1000	183	5.0E+06	7.6E-02	1.4E-01	2.8E-08	6.9E+02
0002212B	120.333	-1.5	100	200	187	6.8E+06	1.8E-01	2.9E-01	4.2E-08	1.0E+03
0002212H	125.053	-1.1	130	100	181	2.2E+07	1.8E+00	4.1E+00	1.9E-07	4.6E+03
0002212R	133.02	-1.4	110	100	161	7.7E+06	6.3E-02	1.6E-01	2.1E-08	5.3E+02
0002212Z	141.275	-1.1	80	100	159	2.9E+07	7.8E-01	2.1E+00	7.3E-08	1.8E+03
0002213E	163.504	-1.4	90	100	168	8.1E+06	1.1E-01	2.6E-01	3.2E-08	7.9E+02
0002213F.A	163.743	-1.5	80	500	168	6.7E+06	4.2E-02	7.9E-02	1.2E-08	2.9E+02
0002213F.B	163.763	-1.6	200	500	168	4.0E+06	6.5E-02	2.5E-01	6.2E-08	1.5E+03

TABLE 5.1: [Continued] Source parameters for 64 mining induced seismic events at Springfield Pike. Read 5.00E-05 as $5.00 \cdot 10^{-5}$.
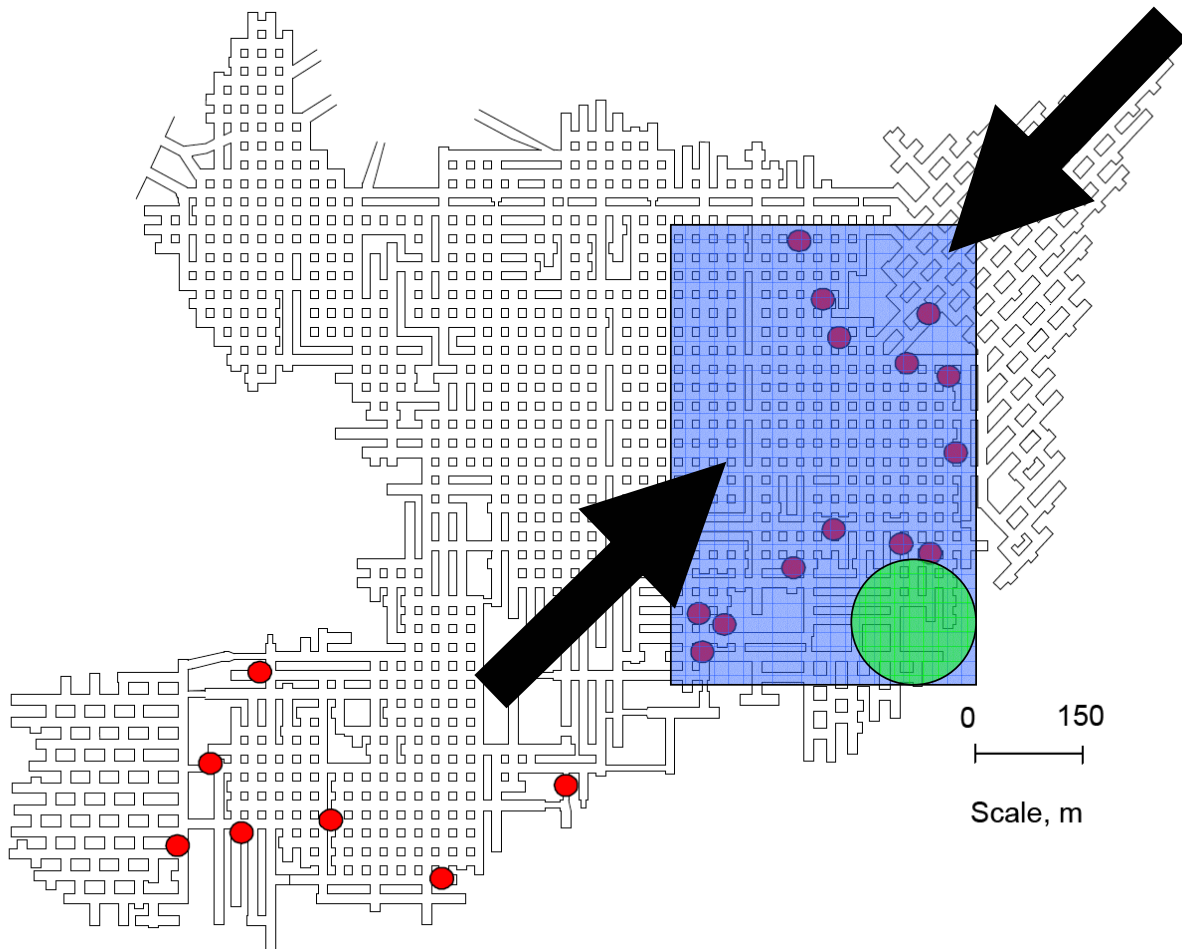
FIGURE 5.1: The plan-view layout of the Springfield Pike underground limestone quarry, where the red dots represent the locations of the geophone stations that made up the Springfield Pike Seismic Monitoring System. The Green Circle highlights the location of a majority of the seismic events (in this data set) that lead to numerous episodes of roof failure, where the Blue Rectangle highlights the locations of the stations that recorded the data examined in this study, which included recordings from 12 of the 14 stations highlighted. The large Black arrows denote the approximate orientation of the regional horizontal stress field. This figure was modified from Iannacchione *et al.* [2005b], with permission.
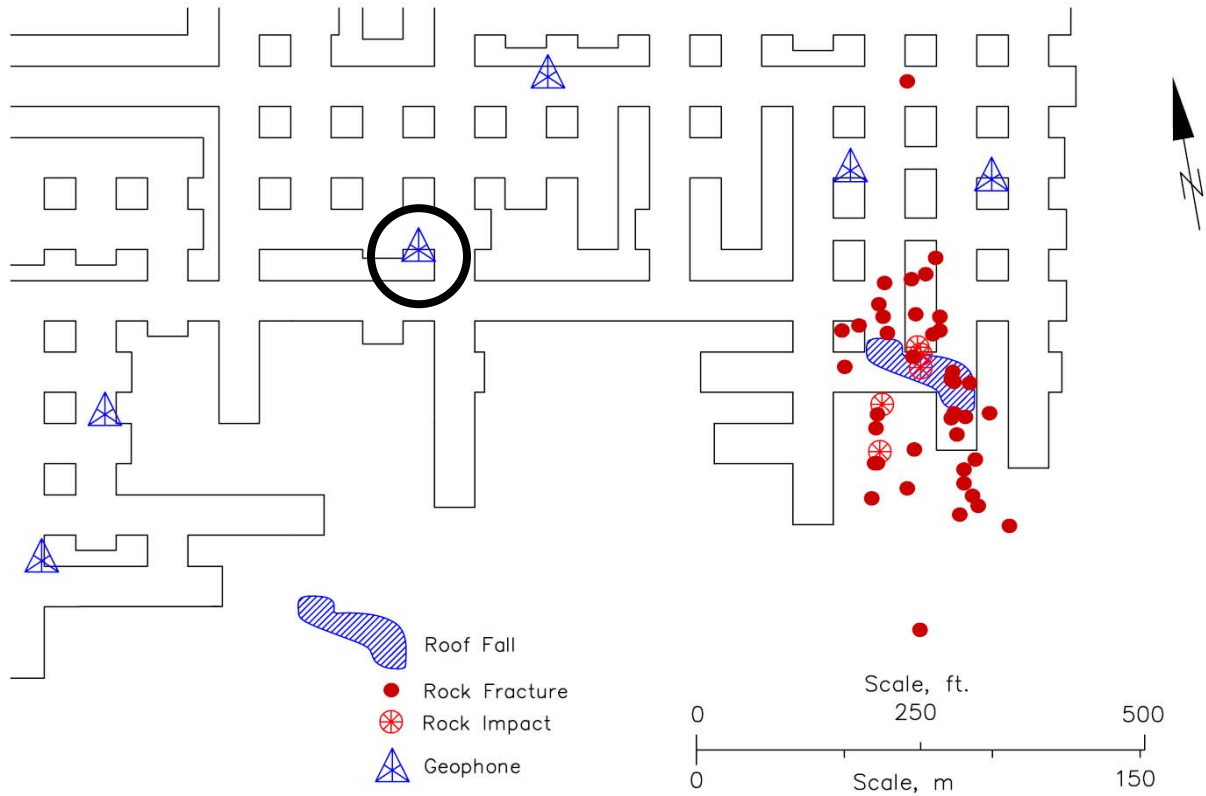
Figure 5.2: Blue Triangles show seismic stations. Solid red circles show seismic events located by NIOSH researchers in an earlier study. This data set is composed of seismic events that led to numerous roof falls. The area of roof failure during this time period is indicated by the Blue Hashed area in the figure, where the "wagon-wheel" symbols denote location estimates of five rock impact events. The geophone circled in Black denotes the location of the station (GN04) that collected the data that was used to estimate the seismic source parameters. This figure was modified from Iannacchione *et al.* [2005b], with permission.
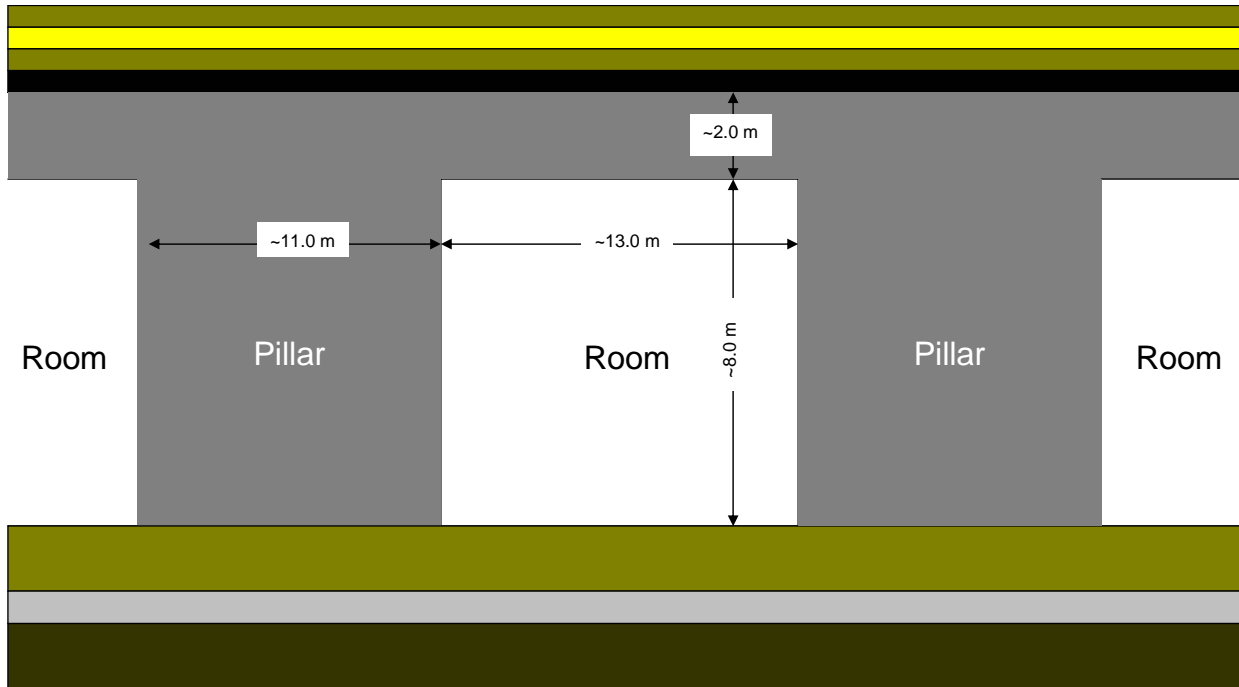
FIGURE 5.3: Illustration depicting the basic geometry of the limestone layer (Dark Grey) after mining. The room-and-pillar design at Springfield Pike requires a significant portion of the limestone layer to remain in place as vertical and lateral support (> 50 percent). To mitigate the effects of a high horizontal stress field, 2.0 meters of the limestone layer is left in place to support the roof spanning between each pillar.
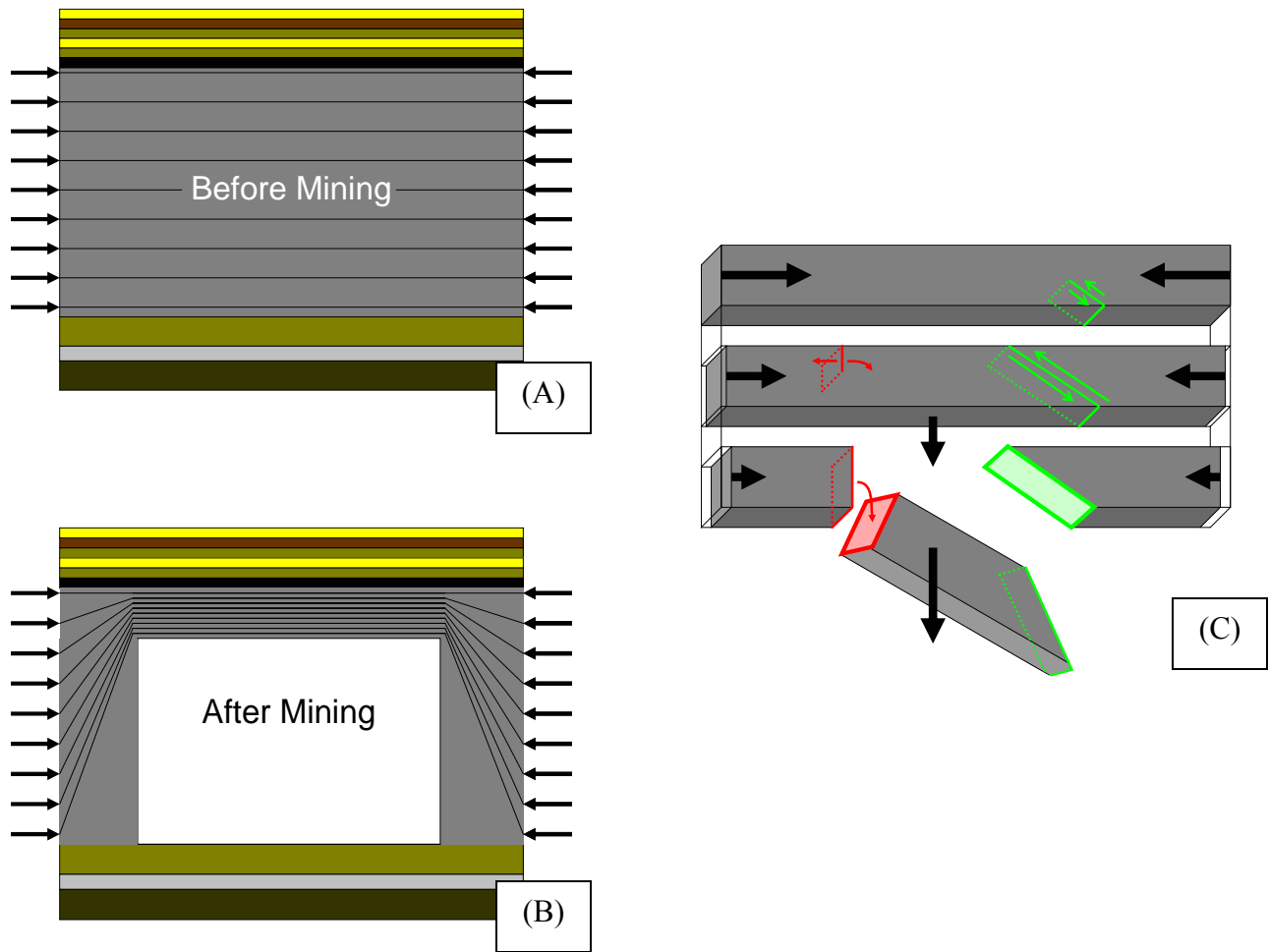
FIGURE 5.4: Possible roof failure process at Springfield Pike. (a) Horizontal stress field evenly distributed in limestone layer; (b) Horizontal stress field concentrated through smaller limestone layer in roof; (c) Failure process initiates as Shear crack (green), ends after Tensile Crack Fails (red).
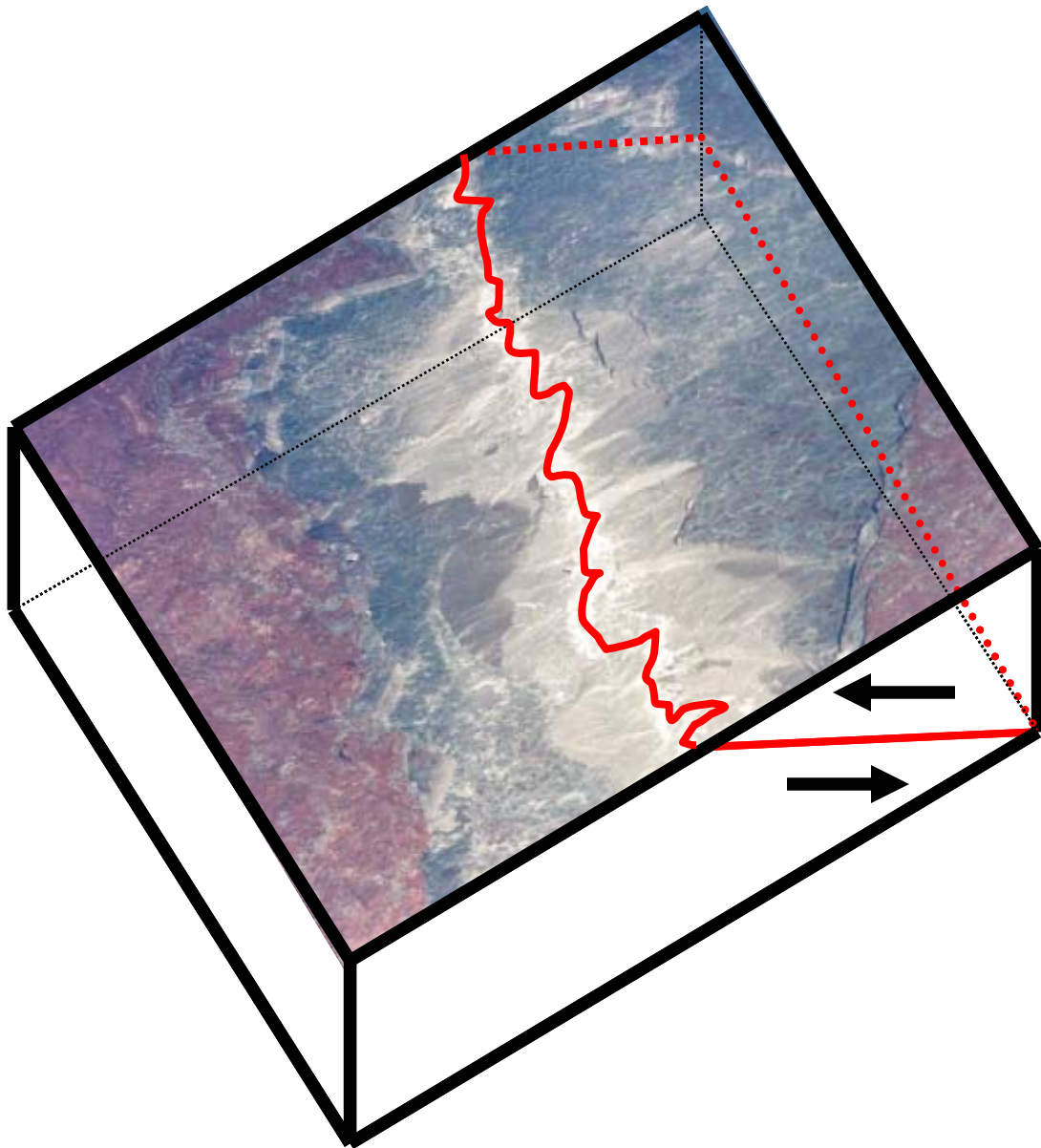
FIGURE 5.5: This is a modified photo (courtesy of A.T. Iannacchione at NIOSH) of the surface expression of a low-angle shear crack. This figure is meant to illustrate the relationship between the surface expression of the shear crack and a possible orientation of a shear plane within the layer of rock, where the Red solid and dashed lines outline the fault plane.

FIGURE 5.6: This photo (courtesy of A.T. Iannacchione at NIOSH) illustrates the result of a major roof failure at Springfield Pike. The elliptical shaped dome is a typical feature of roof failures at Springfield Pike, where the longitudinal axis (longest) of the ellipse is typically perpendicular to the direction of the maximum horizontal stress field. The low-angle shear crack at the top of the dome indicates the possibility that the layers of rock previously below it, suffered from the same failure mechanism before collapsing. The roof-bolts (one circled in the upper-left corner) are installed in order to reduce or eliminate the displacement (or sagging) of the roof, which can typically delay a roof collapse for many weeks or even stop the failure process completely.
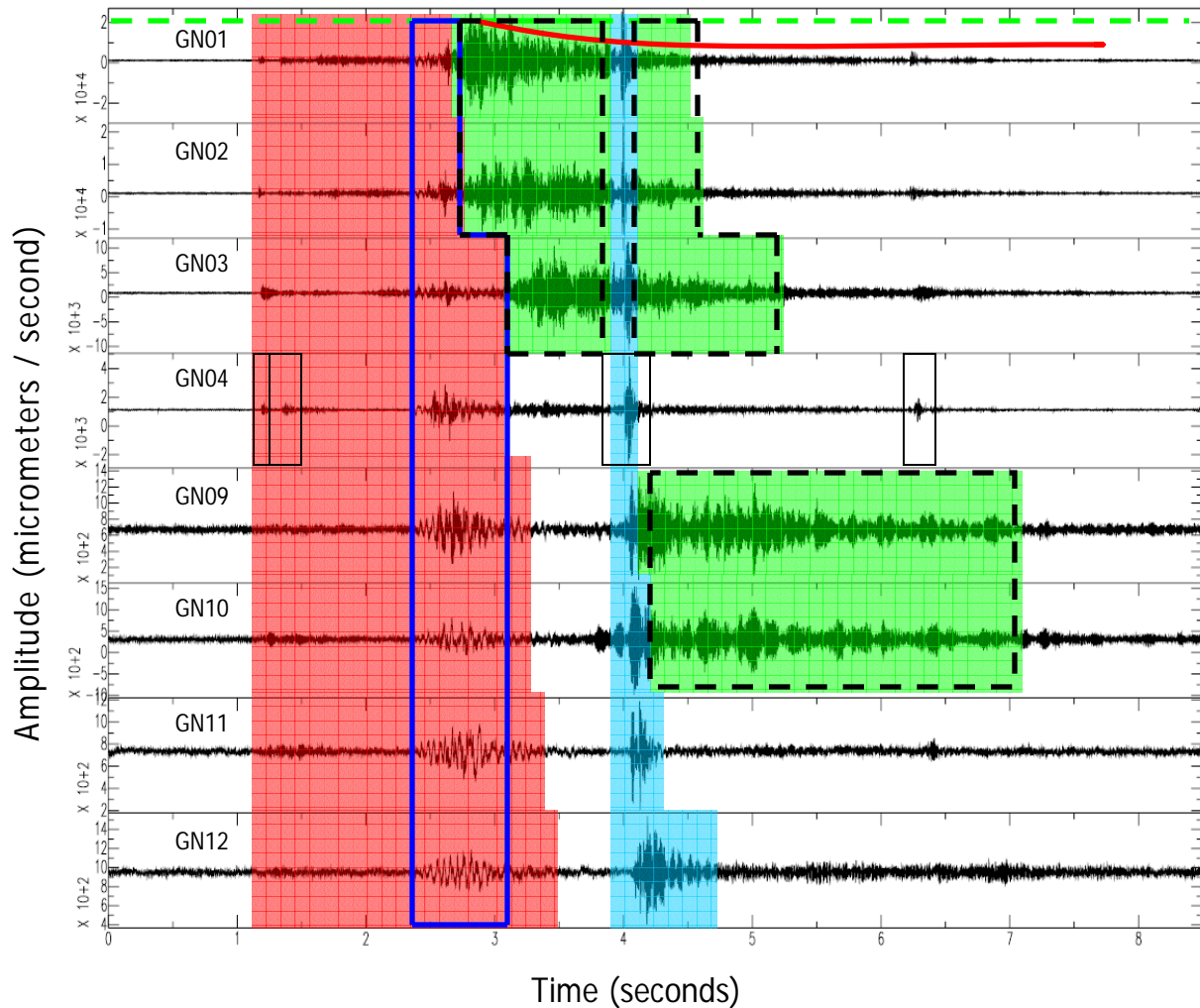
FIGURE 5.7: Example time series of events associated with a roof fall. Signals indicated by the dashed box filled green exhibit a significant delay between its arrival at all the stations and indicate an acoustic transmission through air. Signals in the red and blue regions exhibit move-out's (arrival time versus distance) behavior indicative of seismic transmission through rock. Analysis of the signals in green (see Figure 5.8) indicates that they may have been related to an air blast, which is a displacement in air due to the collapse of roof material. The difference between the pressure wave velocity in air and in rock is consistent with the move-out seen in this data (See Figure 5.8). The approximate peak ground velocity induced by the air blast is indicated by the Green dashed line. The decay curve of the peak air-blast-induced velocity is indicated by the Red solid line, and is assumed to be due to a large initial failure in the roof followed by an asymptotical decay representing a progressively smaller amount of material falling from the roof. The thick-solid-blue boxes indicate the signal that was most likely generated by roof material impacting the mine floor. These station records are associated with file 000220B6, which was triggered at 23:50:54.651 on February 20, 2000.

Distance versus Arrival Time (Relative to first station)
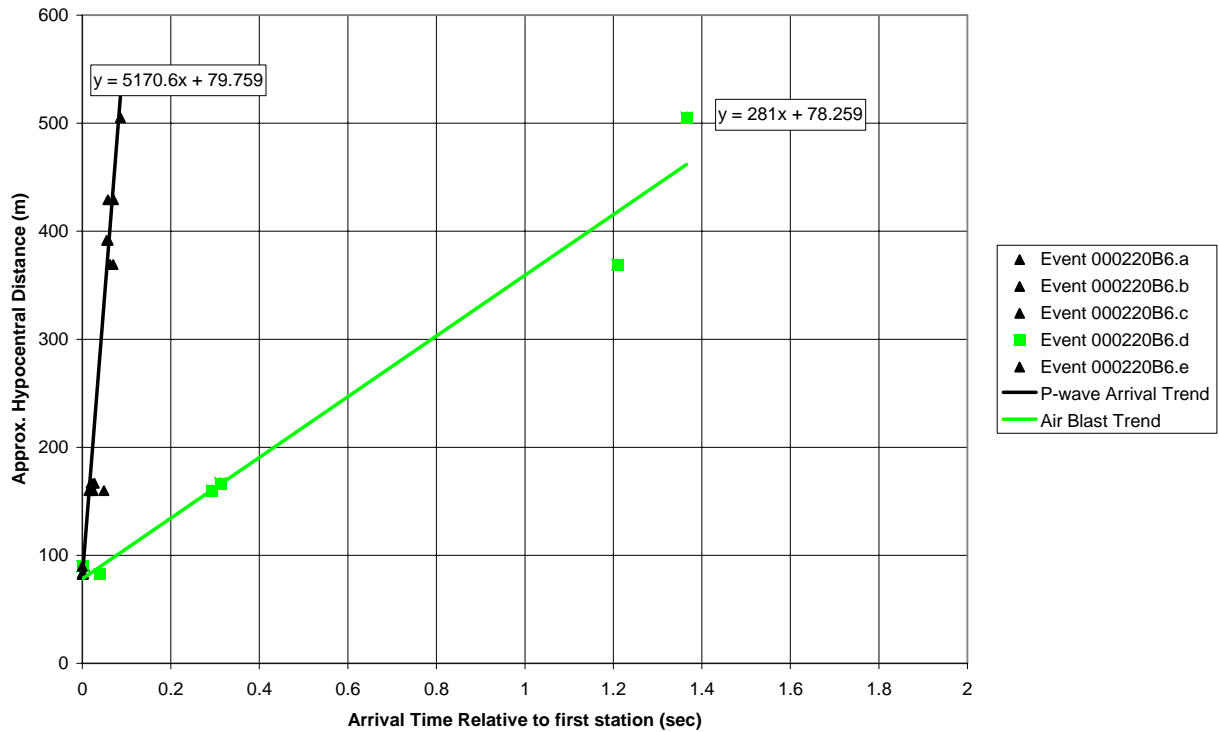

FIGURE 5.8: Distance versus Arrival times for the 000220B6 events. The Green squares and the Green trend line correspond to the distance versus arrival time of the assumed air blast event highlighted Green in Figure (5.7). The Black triangles and Black trend line correspond to the distance versus P-wave arrival time of the events boxed Black in Figure (5.7).
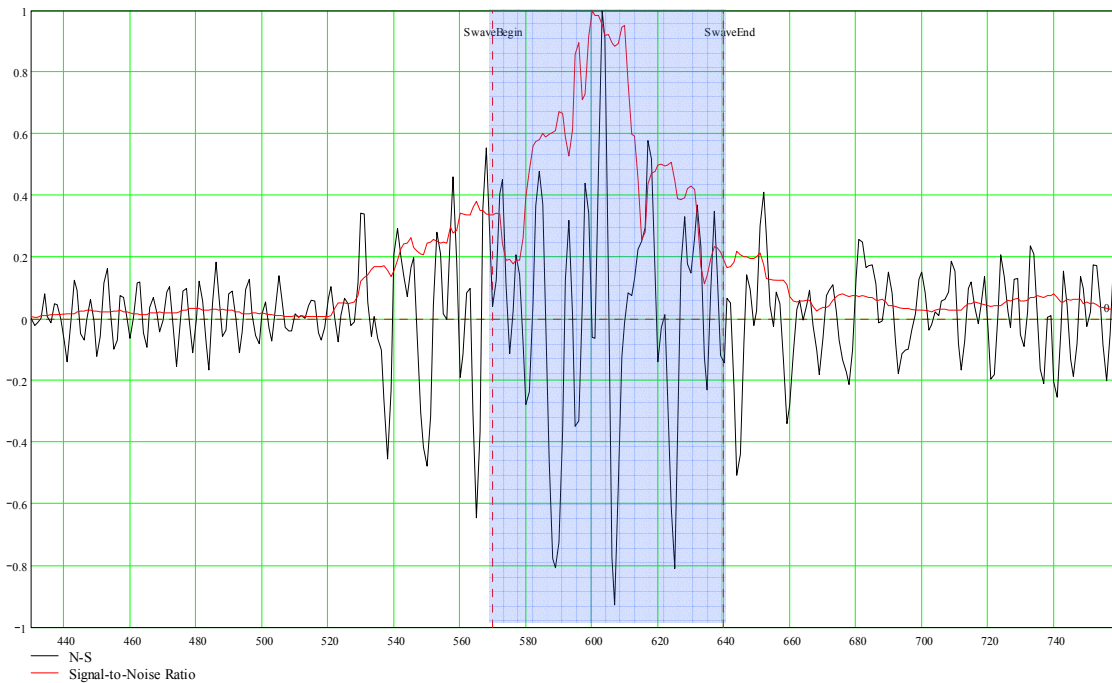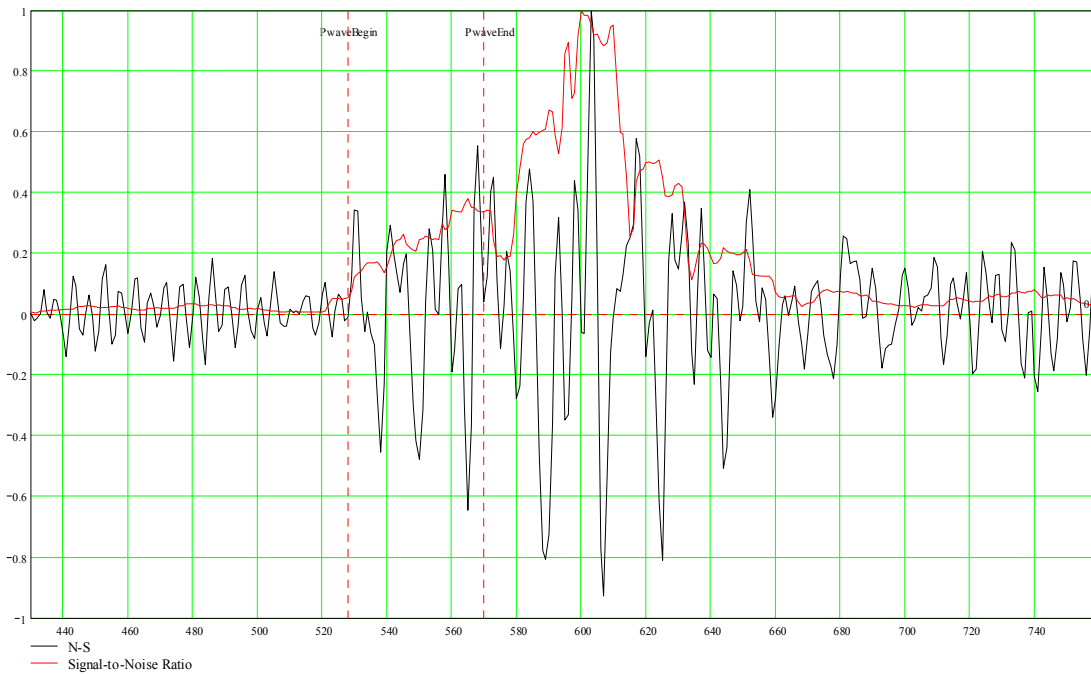
FIGURE 5.9: This figure illustrates the event highlighted in Blue for station GN04 from Figure (5.7). The time-series (Black) is superimposed on the signal-to-noise ratio (Red). The signal-to-noise ratio was typically used to improve the identification of the P-wave phase arrival. The hypocentral distance from the approximate location of the event, which was determined prior to this investigation, was used to improve the identification of the S-wave phase arrival. The Blue area highlights the portion of the time series that was used in calculating the Fourier transform of the S-wave signal for spectral analysis.
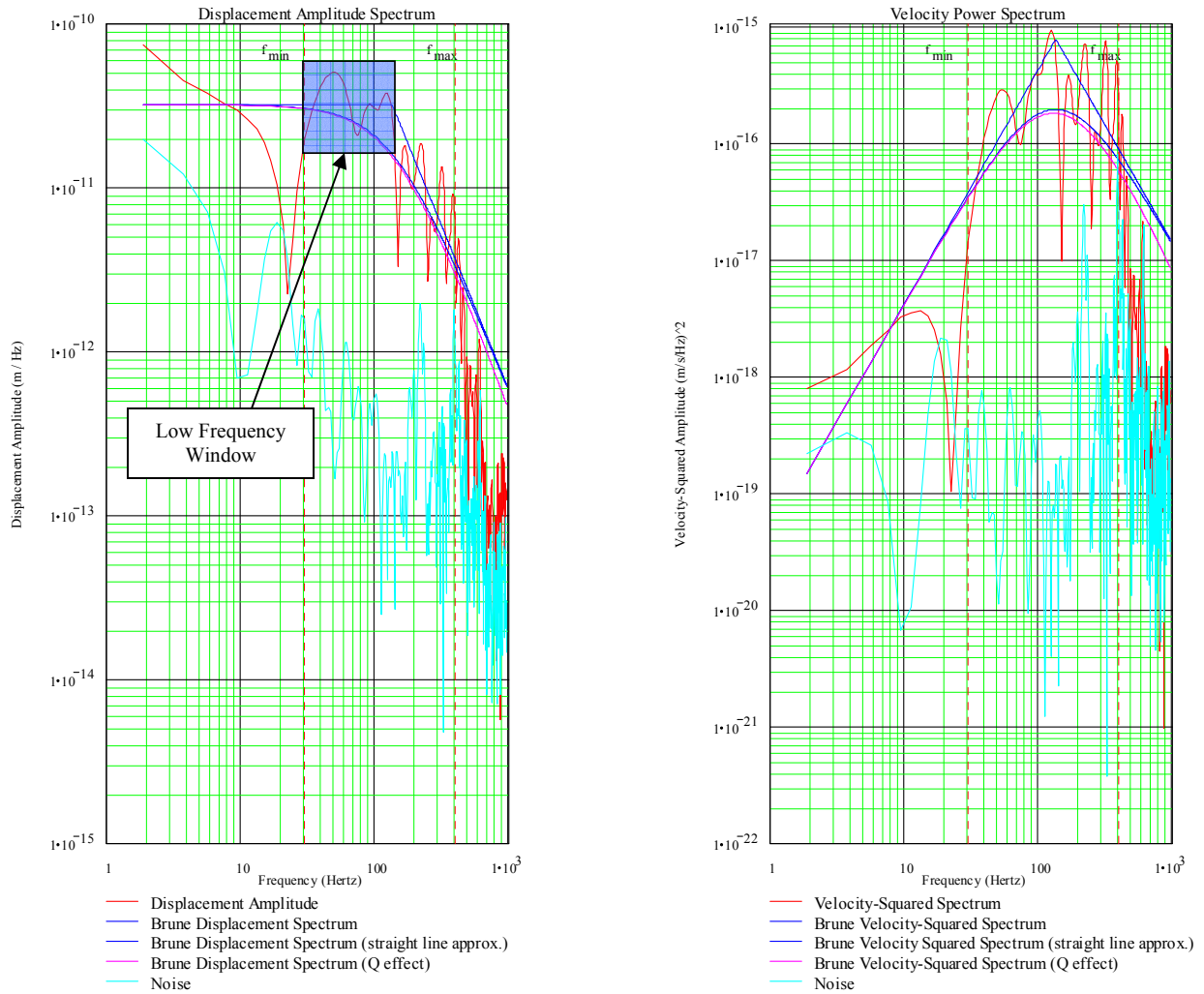
FIGURE 5.10: The Displacement Amplitude Spectra (Left) and Velocity-Squared (Power) Spectra (Right) of the windowed time-series from Figure (5.9). The low-frequency limit (f_{min}) and the high-frequency limit (f_{max}) were determined based on the level of noise. The Low Frequency Window highlights the displacement amplitudes that were used to estimate the zero-frequency displacement amplitude, based on the geometric mean of the amplitudes. The corner frequency and the quality factor were estimated based on visually estimating the theoretical Brune Spectrum that best fit the data.
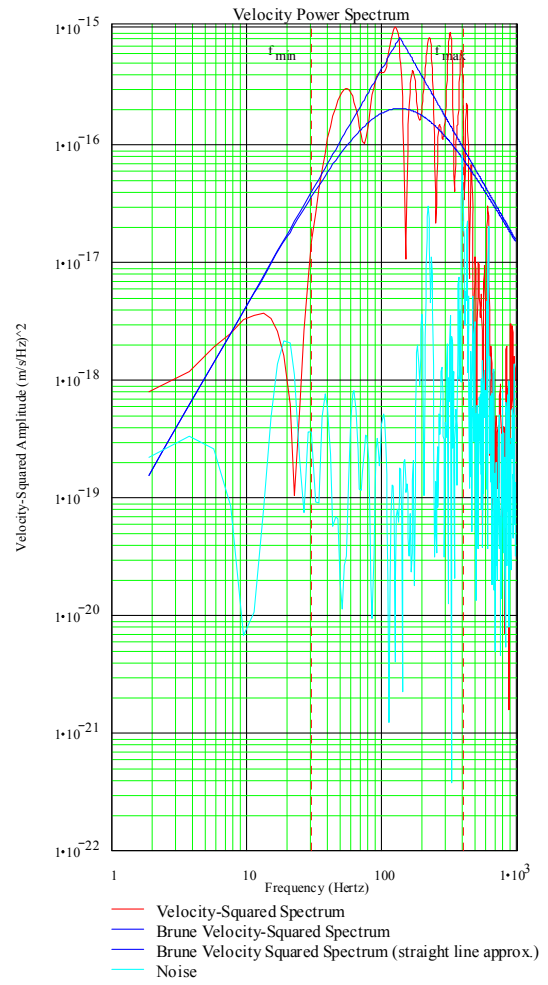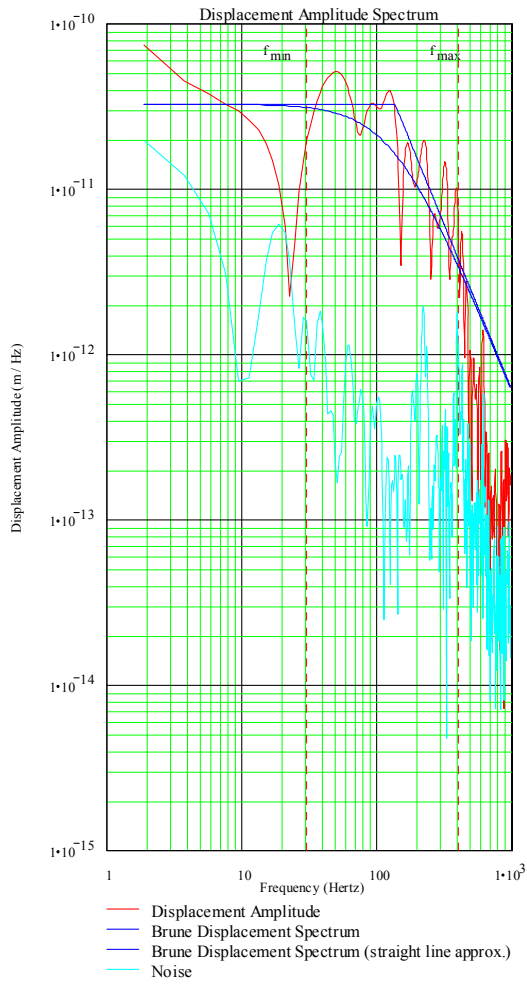
FIGURE 5.11: The *T**-corrected spectra using the estimates of *Q* derived from Figure (5.11).
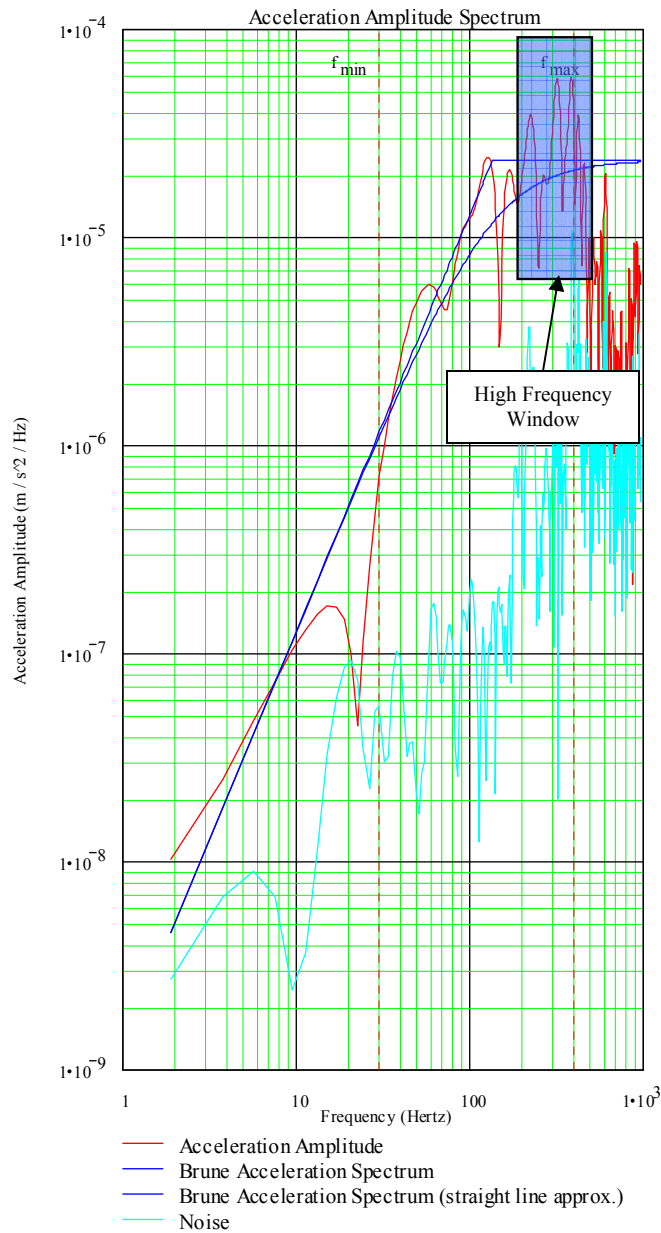
FIGURE 5.12: The *T**-corrected acceleration spectra, where the deviation of the high-frequencies from the theoretical high-frequency spectral plateau based on the Brune model is most obvious. The High Frequency Window of acceleration amplitudes represents the amplitudes that were used to estimate the zero-period (or infinite-frequency) acceleration amplitude to be used in correcting the various integrals of the power spectra for the limitations in high-frequency bandwidth.
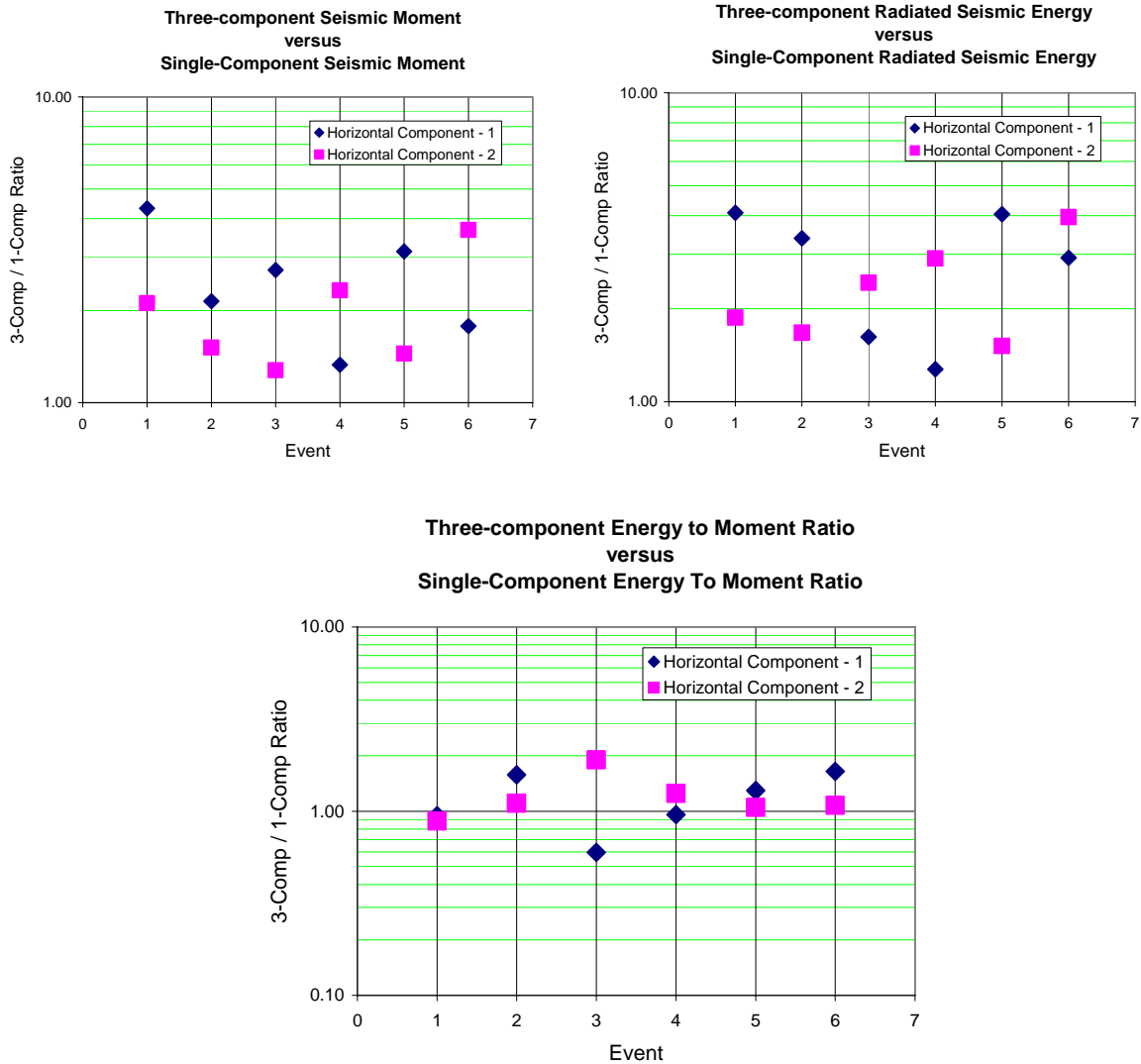
FIGURE 5.13: The three plots illustrate the relationship between the single-component based and the three-component based estimates of the source parameters (Seismic Moment, Radiated Energy and Energy to Moment Ratio) for six events from the Moonee data set. The single-component based source parameter estimates are determined from each of the horizontal components individually. The ratio between the three-component based estimate and the single-component based estimate for each of the three source parameters is plotted above. An important observation is that the ratio between the three-component based estimates and the single-component based estimates for the energy to moment ratio appear to be very close to unity.
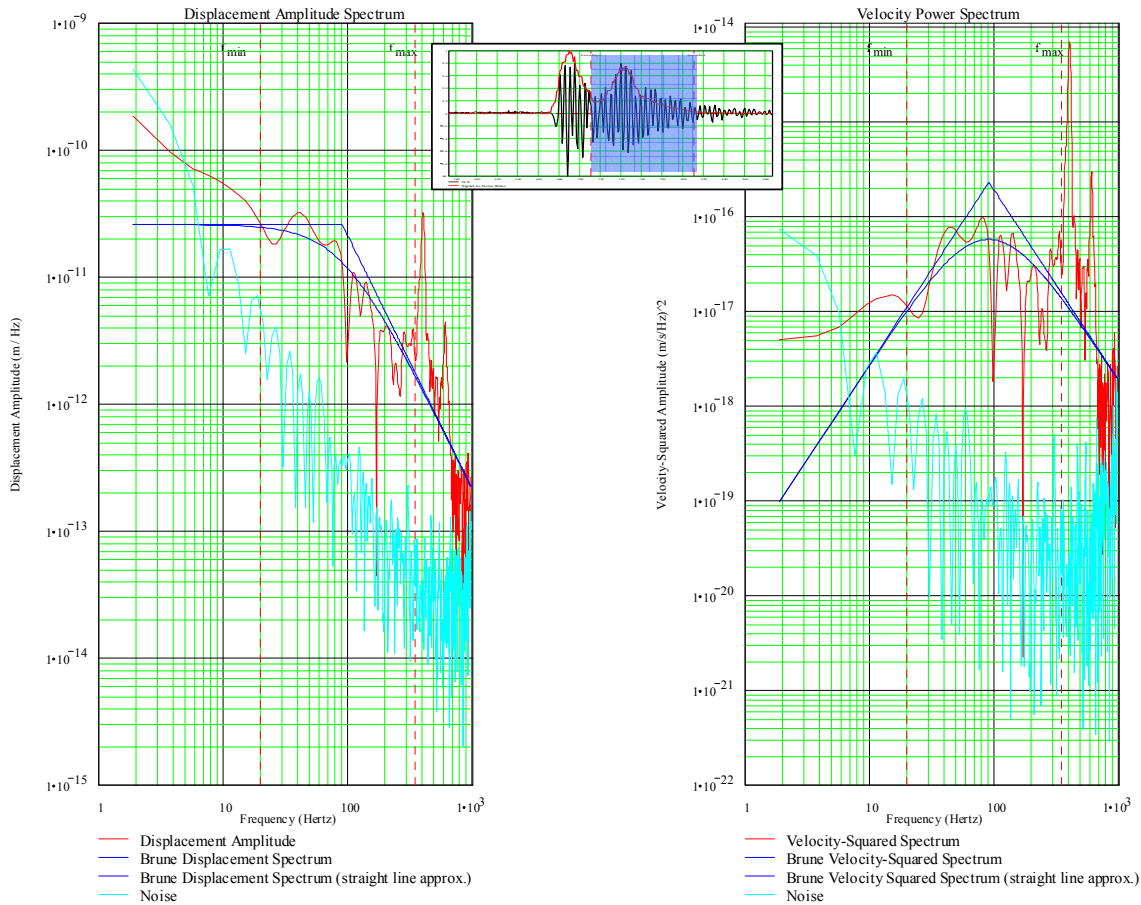
FIGURE 5.14: Fourier amplitude spectra showing prominent spectral peaks at 400 and 625 Hz. The majority of the Fourier amplitude spectra taken from the S-wave windows in the time domain demonstrated similar spectral peaks. We interpret these peaks as due to resonance effects associated with a 2.0 meter thick layer of limestone with P-wave and S-wave velocities of 5000 m/s and 3200 m/s, respectively. The spectra shown here exhibit the largest examples of the assumed resonance phenomenon. The large spectral amplitudes for this particular event (highlighted Blue in the inset time-series) may be due to the proximity of the rock fracture with respect to the 2.0 meter thick layer of limestone that comprises the immediate roof. The harmonic character of the signal implies that the nature of this signal is most likely caused by resonance effects encountered along the transmission path.

Comparison Between Radiated Seismic Energy and Seismic Moment Estimates
(Final Results Uncorrected and Corrected for Attenuation and Limitations in Bandwidth)
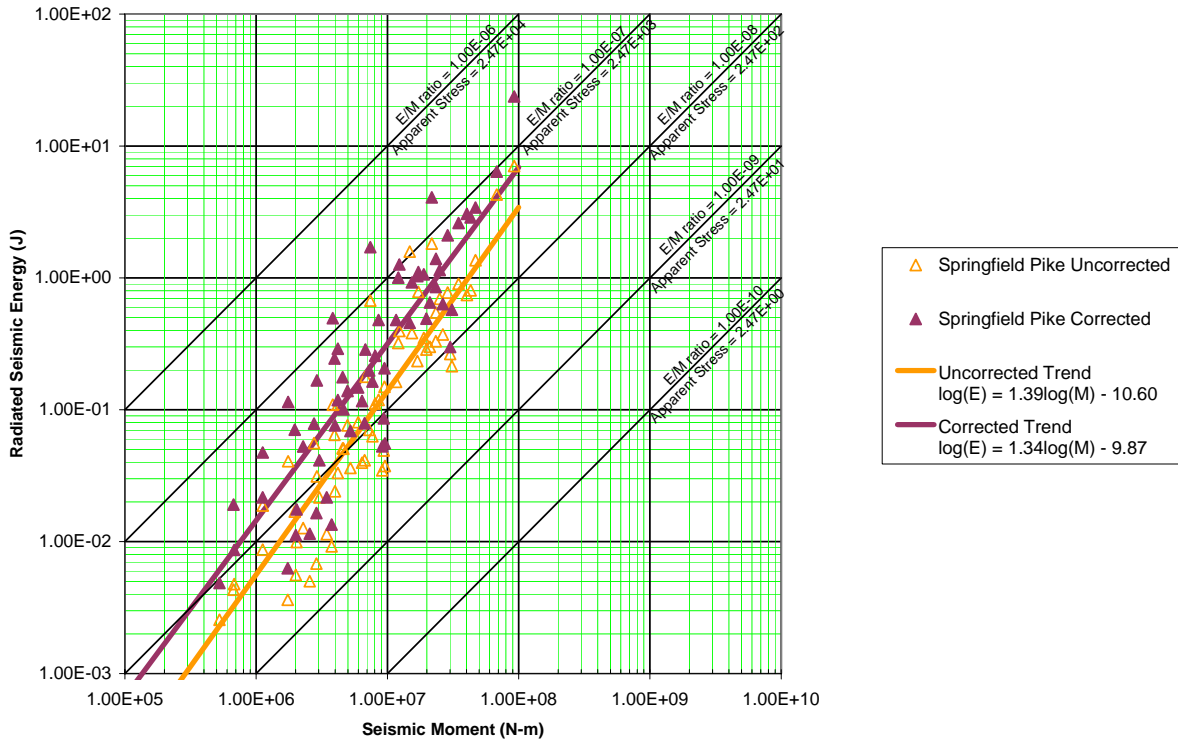
FIGURE 5.15: Uncorrected values (orange triangles) and corrected values (maroon triangles) of the Radiated Seismic Energy versus the Seismic Moment for 64 events from the Springfield Pike Data Set. The results for this data set correspond to estimates in the Seismic Moment and the Radiated Seismic Energy that range from $5 \cdot 10^5 - 1 \cdot 10^8$ N·m and $2 \cdot 10^{-3} - 24$ J, respectively. Equivalently, the Moment Magnitudes lie between -3.75 and -1.33. Lines of constant Apparent Stress and constant Energy to Moment ratio are also plotted, where our assumed material properties lead to a value of $2.47 \cdot 10^{10}$ Pa for rigidity (μ).
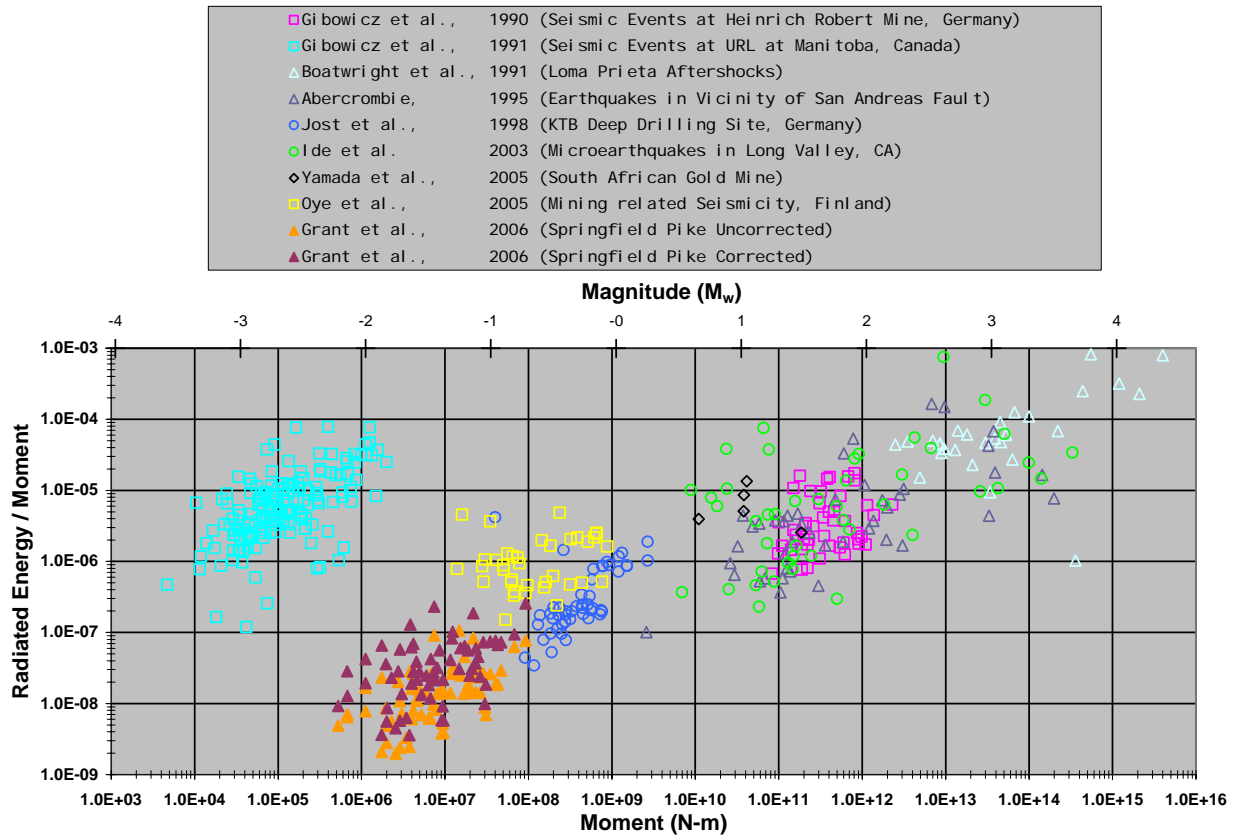
FIGURE 5.16: Final estimates of the ratio between the Radiated Seismic Energy and the Seismic Moment versus the Seismic Moment. Note the relative insignificance of correcting our data for the effects of the bandwidth limitations and the quality factor.
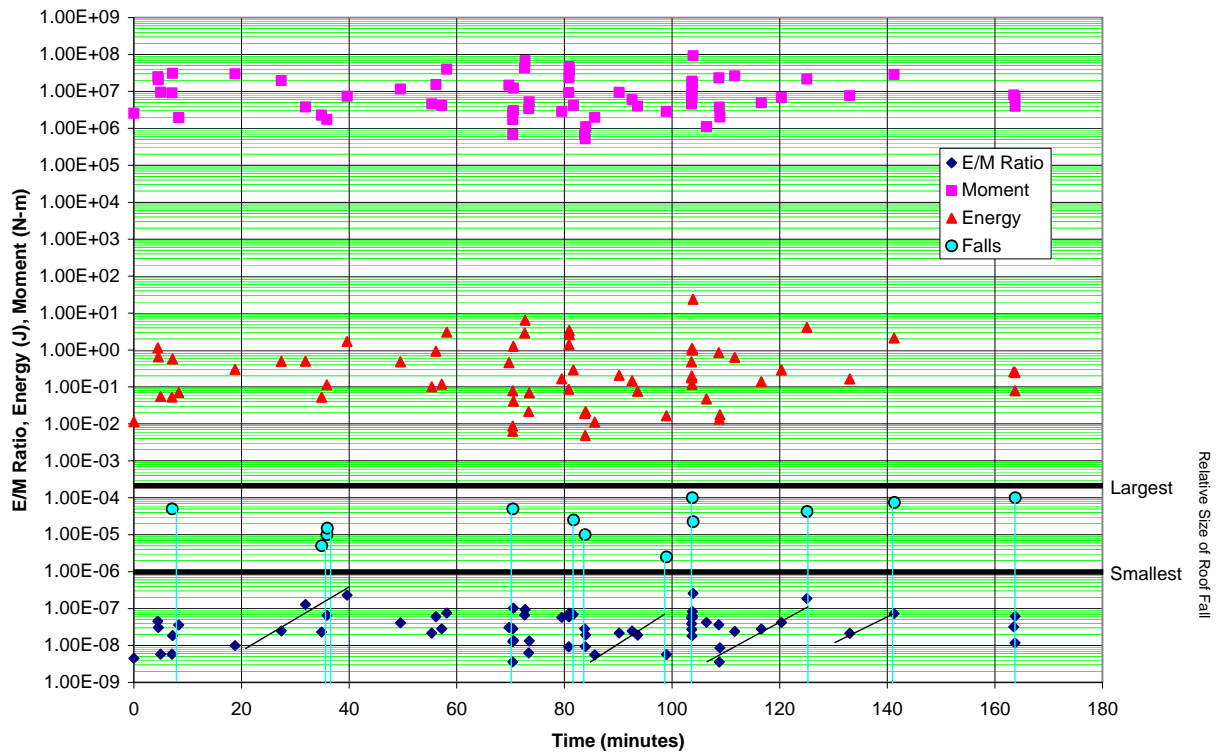
FIGURE 5.17: The Energy to Moment Ratio, the Radiated Seismic Energy, Seismic Moment and the assumed occurrence of roof falls are plotted versus time (in minutes). Over the course of this three-hour time period, thirteen roof falls occurred (based on the assumption that the acoustic signals recorded by the instruments were caused by the displacement of material from the roof). The relative size of the roof fall has been scaled according to the observed approximate peak velocity of roof motion caused by the acoustic disturbance. In some cases, a trend of increasing Energy to Moment Ratio (proportional to Apparent Stress) is seen through time leading up to roof fall events (trends represented as thin black lines through data). The trends plotted here are for events that potentially required many minutes in order for the failure process to develop.
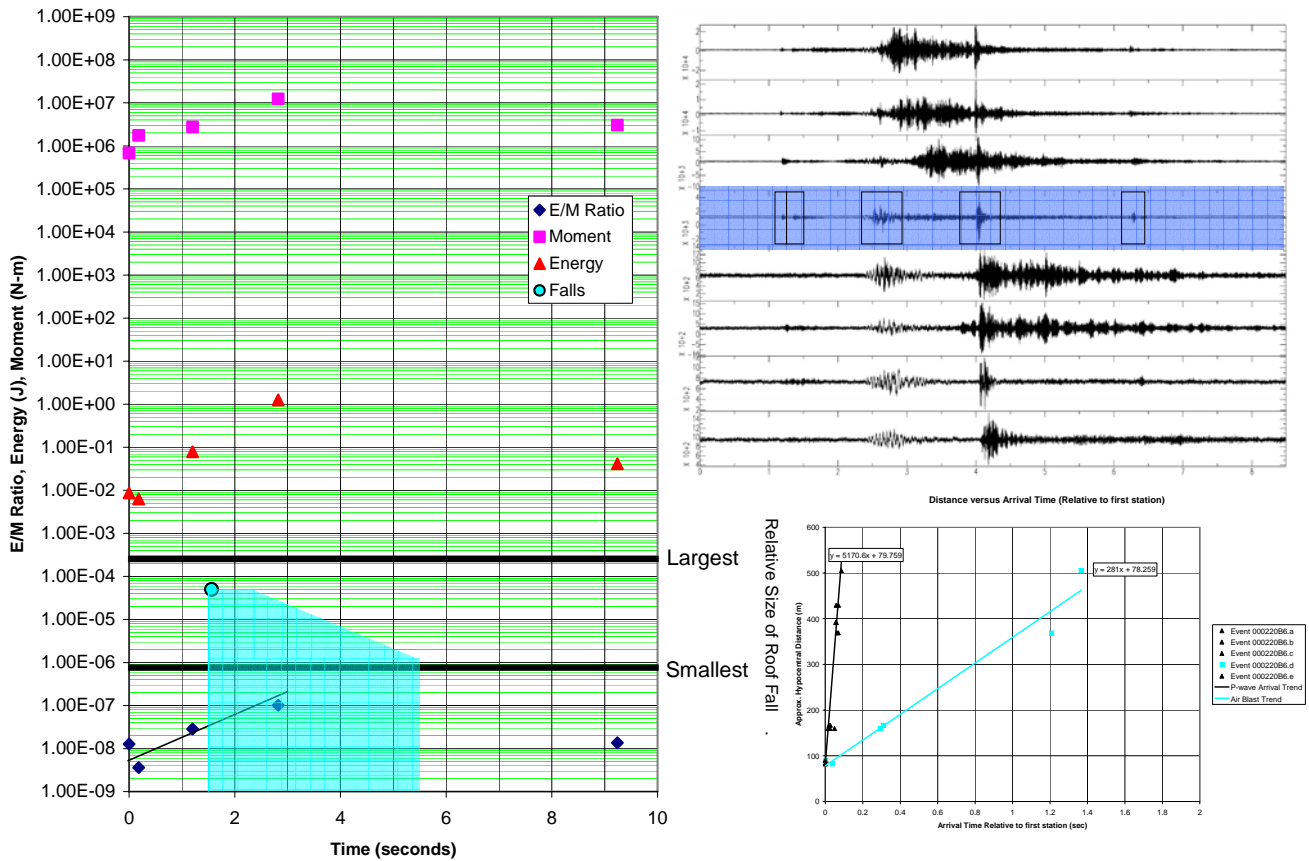
FIGURE 5.18: The Energy to Moment Ratio, the Radiated Seismic Energy, Seismic Moment and relative size of the Roof fall are plotted versus time for the seismic events preceding and following the roof fall associated with the time series in Figure (5.7). The Blue shaded polygon indicates both the approximate duration of the roof fall event and the relative decay in peak air-blast-induced velocity through time. The trends associated with Figure (5.17) are assumed to represent events that require many minutes to develop. The trend of increasing Energy to Moment ratio leading up to this particular roof fall event apparently takes place over a considerably shorter amount of time (a few seconds). The difference in the amount of time that the roof failure develops between this Figure and that of Figure (5.18) may be caused by the difference in the rate that the roof strata were loaded. The data used to obtain the source estimates are highlighted Blue in the time-series, where the individual events are boxed in Black.
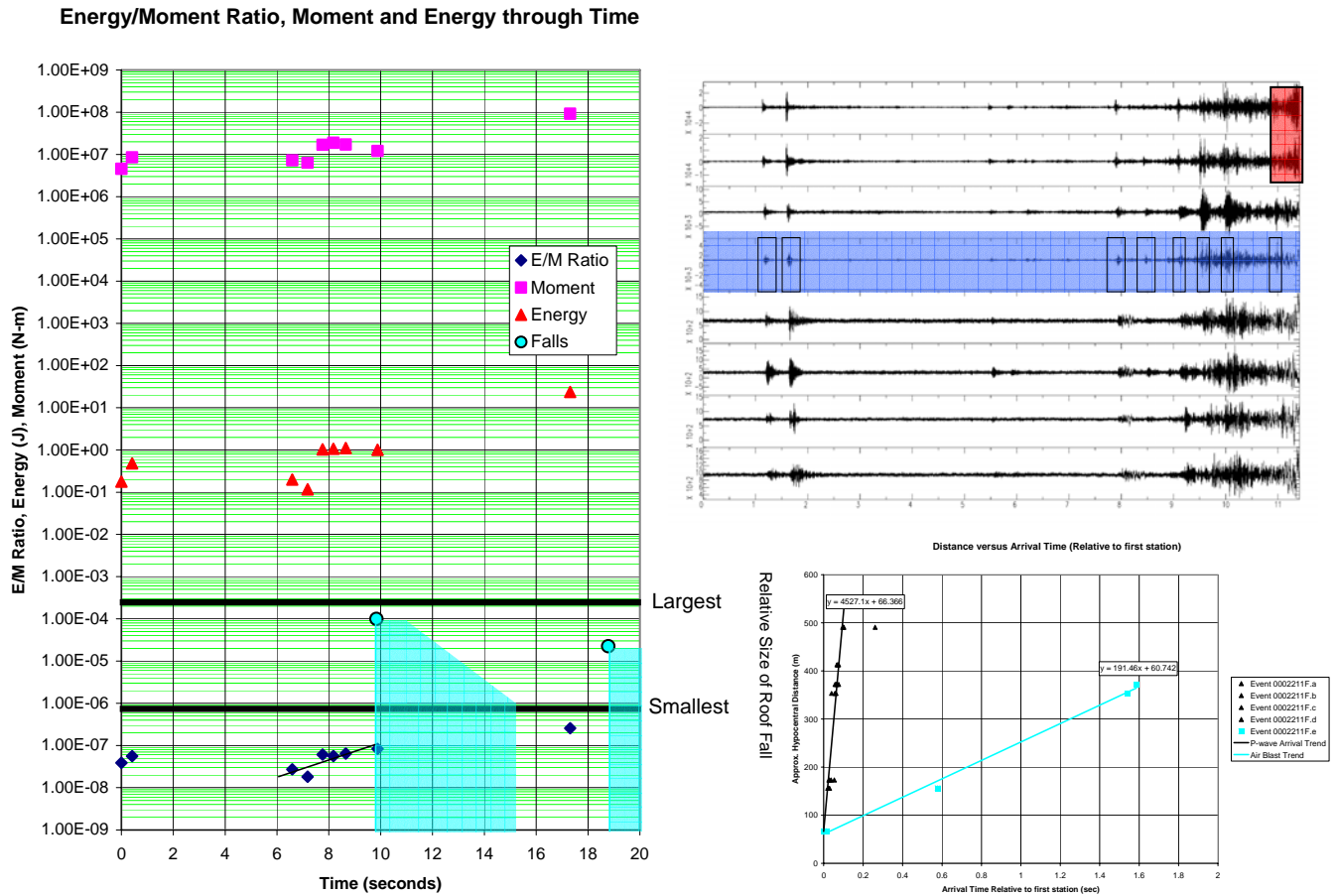
FIGURE 5.19: This in another example of the Energy to Moment Ratio, the Radiated Seismic Energy, Seismic Moment and relative size of the Roof fall plotted versus time for the seismic events preceding and following a roof fall. The Blue shaded polygon indicates both the approximate duration of the roof fall events and the relative decay in peak air-blast-induced velocity through time. As seen in Figure (5.18), the trend of increasing Energy to Moment ratio of the preceding seismic events takes place over a considerably shorter amount of time than the trends identified in Figure (5.17). The difference in the amount of time that the roof failure developed between this Figure and that of Figure (5.17) may be caused by the difference in the rate at which the roof strata were loaded. The data used to obtain the source estimates are highlighted Blue in the time-series, where the individual events are boxed in Black (event file 0002211F). The Red box in the upper-right corner highlights the beginning of the air-blast that occurs ~10 seconds after the first event. The complete air-blast record was saved within another event file (0002211G).

Chapter 6: Discussion of Results and Conclusions

The estimates of the seismic source parameters and the implied source scaling relations derived from the events induced by mining operations at the Moonee Colliery and the Springfield Pike Limestone Quarry are consistent with several recently published studies. Figure (6.1) shows the E_s/M_0 ratio plotted as a function of seismic moment from this study and from eight other studies. This compilation, with one exception, shows a clear trend of increasing E_s/M_0 ratio as a function of seismic moment over ten orders of magnitude of seismic moment. Most of the earlier studies used estimation and correction methods similar to those used in this study. The seismic sources in those studies were both human induced (i.e. mining or fluid injection induced) and tectonically induced (i.e. naturally induced earthquakes). The one exception [Gibowicz *et al.* (1991)] involves events induced by the excavation of a vertical shaft through a granite body. In that case, the source dimension and the magnitudes of the events were much smaller than those involved in the other studies.

In a recent study, Ide and Beroza [2001] developed "corrections" to the Jost *et al.* [1998] and Gibowicz *et al.* [1991] studies. These corrections were meant to account for severe effects of the propagation path, including site induced f_{max}, and recording bandwidth limitations that could not be reconciled in the original data. The results originally published and corrected by Jost *et al.* [1998] and Gibowicz *et al.* [1991] are shown in Figure (6.1). The results of the present study show similarities to originally published results of the earlier studies and do not support the types of corrections offered by Ide and Beroza [2001] for reasons discussed below.

The spectral shapes of the mining induced events of this study clearly demonstrate that they are affected by propagation effects, most likely due to scattering. This, however, did not preclude our ability to make appropriate corrections for the path effects and limitations due to finite bandwidth. The spectra studied here demonstrate an outstanding lack of high frequency energy compared to theoretical events in this magnitude range that would conform to constant stress drop scaling. After correcting for the propagation effects and the limitations associated with a finite recording bandwidth, we observed little change in the trend of increasing E_s/M_0 ratio over two orders of magnitude of seismic moment. The high-frequency displacement amplitudes, in most cases, show nearly constant fall-off rates, as opposed to exponentially decreasing fall-off rates, beyond the observed corner frequencies. Given this, it is not likely that the fundamental observation of nearly constant corner frequencies is due to underestimation of attenuation effects or the existence of some unaccountable site-induced f_{max} as put forth by Ide and Beroza [2001], who favor the constant stress drop model. Rather, the observed increase in the E_s/M_0 ratio versus moment appears to be a real attribute associated with the source of the events studied here. We, therefore, did not use the methods of correction offered by Ide and Beroza [2001], and we interpret the observed trend of increasing E_s/M_0 ratio with increasing seismic moment, in this data set at least, as a well-constrained divergence from constant stress drop scaling (i.e. a divergence from self-similarity).

It is interesting to note that the results of the present study and those of Jost *et al.* [1998] and Gibowicz *et al.* [1991] indicate similar slopes of the E_s/M_0 ratio versus moment relationship (Figure 6.1). The slope of the data on the log-log plot of Figure (6.1) corresponds to

approximately one decade increase on the vertical axis for every one decade increase on the horizontal axis. As shown in Figure (3.13), this slope may be associated with the concept of a minimum source dimension (e.g. Archuleta [1986]). This observation points to the possibility that the apparent breakdown of self-similarity for those data sets may be attributable to a minimum source dimension. In addition, this minimum dimension may be specific to a particular source environment, and not common to all seismogenic regimes. In Figure (6.1), the Gibowicz *et al.* [1991] results plot above the trend defined jointly by the Moonee, the Springfield Pike and the Jost *et al.* [1998] data. The trends shown in Figure (3.13) indicate predicted values for the E_s/M_0 ratio versus seismic moment for a range in minimum source dimensions and suggest that the minimum for the events studied by Jost *et al.* [1998], as well as those at the Moonee Colliery and the Springfield Pike Quarry, are similar (e.g. 5.0 – 30.0 m), whereas the dimension is substantially smaller (approximately 0.1 to 1.0 m) for the events examined by Gibowicz *et al.* [1991].

Earlier work done by Iannacchione *et al.* [2005a] and Iannacchione *et al.* [2005b] have demonstrated that the seismic events in these two underground mine environments are caused by 1) the initiation of fractures within intact rock, 2) the reactivation and growth of pre-existing fractures and, 3) roof material impacting the mine floor. Based on the observation that the E_s/M_0 ratio and seismic moment both increase with time leading up to roof falls at Springfield Pike, it appears that the initial fractures, which conceivably form in large numbers within the roof strata, are relatively small in size and do not allow appreciable amounts of slip to occur across the fracture surface due to significant confinement. However, as the small scale fractures begin to grow, they may form networks that coalesce into larger scale fractures. As growth continues, the potential for significant amounts of slip, and therefore significant amounts of stress release, may increase as the large scale fractures mature.

We propose that the reason for the increased potential in stress release as the failure process develops is likely due to the following combined effects:

- Large scale fractures are not bound by the same relative levels of confinement as are the small scale fractures.
- Large scale fractures represent planes of weakness that have developed through the inception and growth of many small scale fractures.
- Stick - slip behavior along the larger fractures will be more seismically efficient than the formation of the small scale fractures because it does not require as large a fraction of the total available strain energy for fracture growth and for overcoming the friction along fracture surfaces. In the case of the more mature, large scale fractures, a greater fraction of total strain energy will be released as seismic radiation.

We therefore propose a model that combines the concept of a minimum source dimension [Archuleta (1986)] and of slip-weakening [Aki (1979); Byerlee (1967); Dietrich (1979, 1986); Ida (1973); Papageorgiou and Aki (1983a, 1983b), and; Richardson and Jordan (2002)]. As low stress drop, small scale fractures develop within the roof strata and the network created by these fractures begin to coalesce into larger scale fracture planes, larger levels of slip and, as a result, larger releases of stress will tend to occur with each successive event. The progression of small scale fractures to large scale fractures under these assumptions should lead to a trend of both increasing apparent stress and increasing seismic moment with time.

At Springfield Pike, thirteen roof falls were recorded over a three hour time period. We observe trends in the associated rock fracture events leading up to several roof falls indicating that the seismic moment and the apparent stress increase with each successive fracture event until the roof collapsed. The trends were observed to occur over time intervals spanning many tens of minutes to time intervals of only a few seconds. We have assumed that the range in time intervals represent differences in the rate at which the roof strata were loaded, though further investigation is necessary to verify the cause. There appears to be potential for enhancing the warning system in place at Springfield Pike by incorporating near real-time estimates of the apparent stress (or E_s/M_0 ratio) into its decision protocol. The warning system might also improve by installing three-component sensors closer to the problematic area and by installing the sensors to maximize the azimuthal coverage around that area. Better constraints on the locations of the event hypocenters would potentially allow for a weighting factor to be developed based on whether the events tend to occur in clusters or to occur randomly in the roof. This would also improve our understanding of the dominant focal mechanisms during the roof failure process.

The seismic activity at the Moonee Colliery studied here involves events that led up to a single large roof collapse, which is in contrast to the multiple number of smaller successive roof falls at Springfield Pike. The reason for the difference in the failure processes is likely due to the significant difference in the thickness of roof strata comprising the immediate roof. The roof stratum at the Moonee Colliery consists of a ~30 meter thick layer of conglomerate whereas the roof strata at the Springfield Pike Limestone Quarry are composed of ~2 meters thick of limestone overlain by alternating layers of weak claystones, mudstones and sandstones. It has been observed that the roof stratum at the Moonee Colliery collapse as large blocks, instead of small sections. Seismicity at Moonee appears to be distributed over a large area, both within and outside of the roof volume involved in the collapse (Figure 4.1). This is in contrast with the situation at Springfield Pike Limestone Quarry, where the seismic signals associated with the rock fracture events appear to originate near the location of the impending roof falls (Figure 5.2). Incorporating near real-time estimates of the apparent stress (or E_s/M_0 ratio) at the Moonee Colliery, before it closed, might not have been as useful as with Springfield Pike because of the differences in the roof failure processes at the two mines (i.e. Episodic at Moonee versus Progressive at Springfield Pike).

We have found that the seismic events induced by underground mining operations at two locations in sedimentary rock environments do not conform to constant stress drop scaling (i.e. self-similarity). We propose that the dissimilarity in the events is the result of a progression from the inception and growth of small scale fractures to development and slip along large scale fractures as the failure process evolved through time. We find that wave propagation effects and other uncertainties (i.e. associated with data recording limitations, finite signal bandwidth, single-component versus three-component data at one mine, uncertain focal mechanisms) cannot account for the trends that indicate that the apparent stress increases with increasing seismic moment. However, the results of this study do not imply that constant stress drop scaling is violated for *all* events in the studied moment magnitude range. Instead, these results indicate that not all seismic events within seismogenic environments conform to constant stress drop scaling.

The results of this study are perhaps not surprising, given the diversity in tectonic and induced stresses, lithologies, levels of pre-existing deformation, presence or absence of pore fluids, etc. Experience gained in this study indicates that resolution of source controlled effects and effects due to propagation and data collection limitations requires a very high degree of experimental control. In our view, an objective assessment of the entire body of existing evidence strongly indicates that self-similarity does not always hold at the small magnitudes encountered in the mining environment. Arguments for global constant stress drop scaling in this magnitude range [e.g., Ide and Beroza (2001)] are not supported by the results of this study.
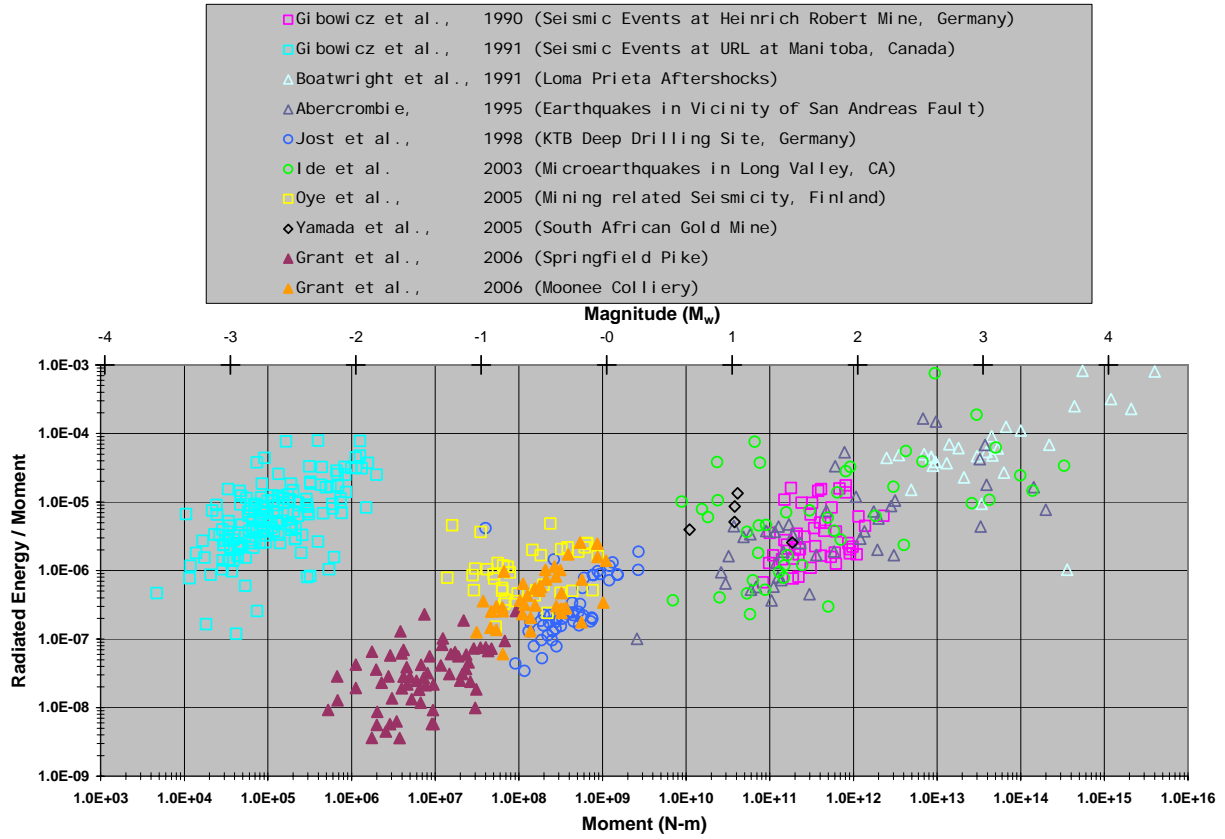
FIGURE 6.1: Ratio of the radiated seismic energy to seismic moment ratio versus the seismic moment for the results from the two data sets studied here and eight additional data sets associated with both induced and natural seismic events.

References

Abercrombie, R. E. (1995). Earthquake source scaling relationships from -1 to 5 M_L using seismograms recorded at 2.5-km depth, *Journal of Geophysical Research* [**100**], 24,015 – 24,036.

Abercrombie, R. E. and P. Leary (1993). Source parameters of small earthquakes recorded at 2.5 km depth, Cajon Pass, southern California: Implications for earthquake scaling, *Geophysical Research Letters* [**20**], 1511 – 1514.

Aki, K. (1967). Scaling law of seismic spectrum, *Journal of Geophysical Research* [**72**], 1217 – 1231.

Aki, K. (1984). Asperities, barriers, characteristic earthquakes and strong ground motion prediction, *Journal of Geophysical Research* [**89**], 5867 – 5872.

Aki, K (1987). Magnitude-frequency relation for small earthquakes: A clue to the origin of f_{max} of large earthquakes, *Journal of Geophysical Research* [**92**], 1349 – 1355.

Aki, K. and P. G. Richards (2002). *Quantitative Seismology* (Second Edition). University Science Books, Sausalito, California, 700 pp.

Anderson, J. G. (1986). Implication of attenuation for studies of the earthquake source, in *Earthquake Source Mechanics, Geophysical Monogram* [**37**], S. Das, J. Boatwright, and C. H. Scholtz (Editors), American Geophysical Union, Washington D.C., 311 – 318.

Anderson, J. G. and S. Hough (1984). A model for the shape of the Fourier amplitude spectrum of acceleration at high frequencies, *Bulletin of the Seismological Society of America* [**74**], 1969 – 1994.

Andrews, D. J. (1980). Fault impedance and earthquake transform energy in the Fourier transform domain, *Bulletin of the Seismological Society of America* [**70**], 1683 – 1698.

Andrews, D. J. (1986). Objective determination of source parameters and similarity of earthquakes of different size, in *Earthquake Source Mechanics, Geophysical Monogram* [**37**], S. Das, J. Boatwright, and C. H. Scholtz (Editors), American Geophysical Union, Washington D.C., 259 – 267.

Archuleta, R. J. (1986). Downhole recordings of seismic radiation, in *Earthquake Source Mechanics, Geophysical Monogram* [**37**], S. Das, J. Boatwright, and C. H. Scholtz (Editors), American Geophysical Union, Washington D.C., 319 – 329.

Archuleta, R. J., R. Cranswick, C. Mueller, and P. Spudich (1982). Source parameters of the 1980 Mammoth Lakes, California, earthquake sequence, *Journal of Geophysical Research* [**87**], 4595 – 4607.

Bakun, W. H, C. G. Bufe, and R. M. Stewart (1976). Body wave spectra of central California earthquakes, *Bulletin of the Seismological Society of America* [**66**], 439– 459.

Boatwright, J. (1980). A spectral theory for circular seismic sources; simple estimates of source dimension, dynamic stress drop, and radiated seismic energy, *Bulletin of the Seismological Society of America* [**70**], 1 – 27.

Boatwright, J. and J. B. Fletcher (1984). The partition of radiated energy between *P* and *S* waves, *Bulletin of the Seismological Society of America* [**74**], 361 – 376.

Boatwright, J., J. B. Fletcher, and T. E. Fumal (1991). A general inversion scheme for source, site, and propagation characteristics using multiply recorded sets of moderate-sized earthquakes, *Bulletin of the Seismological Society of America* [**81**], 1754 – 1782.

Boore, D. M. (1986). The effect of finite bandwidth on seismic scaling relationships, in *Earthquake Source Mechanics, Geophysical Monogram* [**37**], S. Das, J. Boatwright, and C. H. Scholtz (Editors), American Geophysical Union, Washington D.C., 275 – 283.

Brune, J. N. (1970). Tectonic stress and the spectra of seismic shear waves from earthquakes, *Journal of Geophysical Research* [**75**], 4997– 5009.

Brune, J. N. (1971). Correction, *Journal of Geophysical Research* [**76**], 5002.

Byerlee, J. D. (1967). Frictional characteristics of granite under high confining pressure, *Journal of Geophysical Research* [**72**], 3639 – 3648.

Byerlee, J. D. and W. F. Brace (1968). Stick slip, stable sliding, and earthquakes – Effect of rock type, pressure, strain rate, and stiffness, *Journal of Geophysical Research* [**73**], 6031 – 6037.

Chouet, B., K. Aki, and M. Tsujiura (1978). Regional variation of the scaling law of earthquake source spectra, *Bulletin of the Seismological Society of America* [**68**], 49 – 79.

Di Bona, M., A. Rovelli (1988). Effects of the bandwidth limitation on stress drops estimated from integrals of the ground motion, *Bulletin of the Seismological Society of America* [**78**], 1818 – 1825.

Dietrich, J. H. (1979). Modeling of rock friction, 1, Experimental results and constitutive equations, *Journal of Geophysical Research* [**85**], 2161 – 2168.

Dietrich, J. H. (1986). A model for the nucleation of earthquake slip, in *Earthquake Source Mechanics, Geophysical Monogram* [**37**], S. Das, J. Boatwright, and C. H. Scholtz (Editors), American Geophysical Union, Washington D.C., 37 – 47.

Eshelby, J. D. (1957). The determination of the elastic field of an ellipsoidal inclusion and related problems, *Proceedings of The Royal Society of London. Series A*. [**241**], 376 – 396.

Fletcher, J. B., L. C. Haar, F. L. Vernon, J. N. Brune, T. C. Hanks and J. Berger (1986). The effects of attenuation on the scaling of source parameters for earthquakes at Anza, California, in *Earthquake Source Mechanics, Geophysical Monogram* [**37**], S. Das, J. Boatwright, and C. H. Scholtz (Editors), American Geophysical Union, Washington D.C., 331 – 338.

Frankel, A. and L. Wennerberg (1989). Microearthquake spectra from the Anza, California seismic network: Site response and source scaling, *Bulletin of the Seismological Society of America* [**79**], 581 – 609.

Gibowicz, S. J., H.-P. Harjes, and M. Schäfer (1990). Source parameters of seismic events at Heinrich Robert Mine, Ruhr Basin, Federal Republic of Germany: Evidence for non-double-couple events, *Bulletin of the Seismological Society of America* [**80**], 88 – 109.

Gibowicz, S. J., R. P. Young, S. Talebi, and D. J. Rawlence (1991). Source parameters of seismic events at the underground research laboratory in Manitoba, Canada: Scaling relations for events with moment magnitude smaller than -2, *Bulletin of the Seismological Society of America* [**81**], 1157 – 1182.

Guo, H. A., A. Lerner-Lam, and S. E. Hough (1992). Empirical Green's function study of Loma Prieta aftershocks: Evidence for fault zone complexity (abstract), *Seismological Research Letters* [**63**], 76.

Gutenberg, B. and C. Richter (1956). Magnitude and energy of earthquakes, *Annali di Geofisica* [**9**], 1 – 15.

Hanks, T. C. (1982). f_{max}, *Bulletin of the Seismological Society of America* [**72**], 1867 – 1879.

Hanks, T. C. and M. Thatcher (1972). A graphical representative of seismic source parameters, *Journal of Geophysical Research* [**77**], 4393 – 4405.

Iannacchione, A.T., L.M. Burke, and M.C. Chapman (2005a). Characterizing Roof Fall Signatures from Underground Mines, in *6th International Symposium on Rockbursts and Seismicity in Mines*, March 9 – 11, Perth, Australia.

Iannacchione, A. T., G. S Esterhuizen, T. S. Bajpayee, P. L. Swanson, and M. C. Chapman (2005b). Characteristics of Mining-Induced Seismicity Associated with Roof Falls and Roof Caving Events, in *40th U.S. Symposium on Rock Mech.*, ARMA/USRMS 05-678.*ics*

Ida, Y. (1973). The maximum acceleration of seismic ground motion, *Bulletin of the Seismological Society of America* [**63**], 959 – 968.

Ide, S. and G. C. Beroza (2001). Does apparent stress vary with earthquake size?, *Geophysical Research Letters* [**28**], 3349 – 3352.

Ide, S., G. C. Beroza, S. G. Prejean, and W. L. Ellsworth (2003). Apparent break in earthquake scaling due to path and site effects on deep borehole recordings, *Journal of Geophysical Research* [**108**], ESE 16, 1 - 12.

Jepsen, D. C. and B. L. N. Kennett (1990). Three-component analysis of regional seismograms, *Bulletin of the Seismological Society of America* [**80**], 2032 – 2052.

Jost, M. L., T. Büßelberg, Ö. Jost and H.-P. Harjes (1998). Source parameters of injection-induced microearthquakes at 9 km depth at the KTB deep drilling site, Germany, *Bulletin of the Seismological Society of America* [**88**], 815 – 832.

Jurkevics, A. (1988). Polarization analysis of three-component array data, *Bulletin of the Seismological Society of America* [**78**], 1725 – 1743.

Keilis-Borok, V. I. (1959).On the estimation of the displacement in an earthquake source and of source dimensions, *Annali di Geofisica* [**12**], 205 – 214.

Keilis-Borok, V. I. (1960). Investigation of the mechanism of earthquakes, *Soviet Research in Geophysics (English Translation)* [**4**], American Geophysical Union, Consultants Bureau, New York, pp. 201.

Lockner, D. A. and P. G. Okubo (1983). Measurements of frictional heating in granite, *Journal of Geophysical Research* [**88**], 4313 – 4329.

Madariaga, R. (1976). Dynamics of an expanding circular fault, *Bulletin of the Seismological Society of America* [**66**], 639 – 666.

Madariaga, R. (1977). Implications of stress-drop models of earthquakes for the inversion of stress drop from seismic observations, *Pure and Applied Geophysics* [**115**], 301 – 316.

McGarr, A. (1999). On relating apparent stress to the stress causing earthquake fault slip, *Journal of Geophysical Research* [**104**], 3003 – 3011.

McGarr, A., R. B. Hofmann, and G. D. Hair (1964). A moving-time-window signal-spectra process, *Geophysics* [**29**], 212 – 220.

Ohnaka, M. (1973). A physical understanding of the earthquake source mechanism, *Journal of Physics of the Earth* [**21**], 30 – 59.

Oye, V., H. Bungum, and M. Roth (2005). Source parameters and scaling relations for mining-related seismicity within the Pyhäsalmi Ore Mine, Finland, *Bulletin of the Seismological Society of America* [**95**], 1011 – 1026.

Papageorgiou, A. S. and K. Aki (1983a). A specific barrier model for the quantitative description inhomegenous faulting and the prediction of strong ground motion. I. Description of the model, *Bulletin of the Seismological Society of America* [**73**], 693 – 722.

Papageorgiou, A. S. and K. Aki (1983b). A specific barrier model for the quantitative description inhomegenous faulting and the prediction of strong ground motion. Part II. Applications of the model, *Bulletin of the Seismological Society of America* [**73**], 953 – 978.

Prejean, S. G. and W. L. Ellsworth (2001). Observations of earthquake source parameters at 2 km depth in the Long Valley Caldera, Eastern California, *Bulletin of the Seismological Society of America* [**91**], 165 – 177.

Richardson, E. and T. H. Jordan (2002). Seismicity in deep gold mines of South Africa: Implications for tectonic earthquakes, *Bulletin of the Seismological Society of America* [**92**], 1766 – 1782.

Rydelek, P. A., and I. S. Sacks (1989). Testing the completeness of earthquake catalogues and the hypothesis of self-similarity, *Nature* [**337**], 251 – 253.

Sacks, I. S. and P. A. Rydelek (1995). Earthquake "Quanta" as an explanation for observed magnitudes and stress drops, *Bulletin of the Seismological Society of America* [**85**], 808 – 813.

Savage, J. C., and M. D. Wood (1971). The relation between apparent stress and stress drop, *Bulletin of the Seismological Society of America* [**61**], 1381 – 1388.

Snoke, J. A., A. T. Londe, and I. S. Sacks (1983). Apparent stress: an estimate of the stress drop, *Bulletin of the Seismological Society of America* [**73**], 339 – 348.

Snoke, J. A. (1987). Stable determination of (Brune) stress drops, *Bulletin of the Seismological Society of America* [**77**], 530 – 538.

Spottiswoode, S. M. and A. McGarr (1975). Source parameters of tremors in a deep-level gold mine, *Bulletin of the Seismological Society of America* [**65**], 93 – 112.

Tucker, B. E., and J. N. Brune (1973). S-wave spectra and source parameters for aftershocks of the San Fernando earthquake of February 9, 1971, in *Geological and Geophysical Studies* [**3**], *San Fernando Earthquake of February 9, 1971*, National Oceanic and Atmospheric Administration, Washington, D. C., 69 – 122.

Wessel, P. and W. H. F. Smith (1998). New and improved version of Generic Mapping Tools released, *EoS, Transactions of the American Geophysical Union* [**79**], 579.

White, J. E. (1964). Motion product seismograms, *Geophysics* [**29**], 288 – 298.

Wyss, M. and J. N. Brune (1968). Seismic Moment, Stress, and Source Dimension for Earthquakes in the California-Nevada Region, *Journal of Geophysical Research* [**73**], 4681 − 4694.

Yamada, T., J. J. Mori, S. Ide, H. Kawakata, Yoshihisa Iio, and H. Ogasawara (2005a). Radiation efficiency and apparent stress of small earthquakes in a South African gold mine, *Journal of Geophysical Research* [**110**], B01305, 1 − 18.

Yamada, T., J. J. Mori, S. Ide, H. Kawakata, Yoshihisa Iio, and H. Ogasawara (2005b). Correction to "Radiation efficiency and apparent stress of small earthquakes in a South African gold mine", *Journal of Geophysical Research* [**110**], B06301, 1 − 2.

Suggested Reading

Abercrombie, R. E. and J. N. Brune (1994). Evidence for a constant *b*-value above magnitude 0 in the southern San Andreas, San Jacinto and San Miguel fault zones, and at the Long Valley caldera, California, *Geophysical Research Letters* [**21**], 1647 -1650.

Aki, K. (1988). Physical theory of earthquakes, in *Seismic Hazard in Mediterranean Regions*, J. Bonnin, M. Cara, A. Cisternas and R. Fantechi (Editors), Kluwer, Dordrecht, $3 - 33$.

Amitrano, D., J. R. Grasso, and G. Senfaute (2005). Seismic precursory patterns before a cliff collapse and critical point phenomena, *Geophysical Research Letters* [**32**], L08314, $1 - 5$.

Bakun, W. H, C. G. Bufe, and R. M. Stewart (1980a). Do P- and S-wave corner frequencies measure different source parameters?, *United States Geological Survey Open File Report* [**80-602**], $1 - 10$.

Bakun, W. H. and M. McLaren (1984). Microearthquakes and the nature of the creeping-to-locked transition of the San Andreas fault zone near San Juan Bautista, California, *Bulletin of the Seismological Society of America* [**74**], $235 - 254$.

Bakun, W. H, R. M. Stewart, and C. G. Bufe (1978). Directivity in the high frequency radiation of small earthquakes, *Bulletin of the Seismological Society of America* [**68**], $1253 - 1263$.

Bakun, W. H., R. M. Stewart, C. G. Bufe, and S. M. Marks (1980b). Implication of seismicity for failure of a section of the San Andreas fault, *Bulletin of the Seismological Society of America* [**70**], $185 - 201$.

Beeler, N. M., T. –F. Wong, and S. H. Hickman (2003). On the expected relationships among apparent stress, static stress drop, effective shear fracture, and efficiency, *Bulletin of the Seismological Society of America* [**93**], $1381 - 1389$.

Boatwright, J. (1978). Detailed spectral analysis of two small New York State earthquakes, *Bulletin of the Seismological Society of America* [**68**], $1117 - 1131$.

Boatwright, J. (1984a). The effect of rupture complexity on estimates of source size, *Journal of Geophysical Research* [**89**], $1132 - 1146$.

Boatwright, J. (1984b). Seismic estimates of stress release, *Journal of Geophysical Research* [**89**], $6961 - 6968$.

Boatwright, J., G. L. Choy, and L. C. Seekins (2002). Regional estimates of radiated seismic energy, *Bulletin of the Seismological Society of America* [**92**], $1241 - 1255$.

Bodin, P. and S. Horton (2004). Source parameters and tectonic implication of aftershocks of the M_W 7.6 Bhuj earthquake of 26 January 2001, *Bulletin of the Seismological Society of America* [**94**], $818 - 827$.

Bodin, P., L. Malagnini, and A. Akinci (2004). Ground-motion scaling in the Kachchh Basin, India, deduced from aftershocks of the 2001 M_W 7.6 Bhuj earthquake, *Bulletin of the Seismological Society of America* [**94**], 1658 – 1669.

Boore, D. M. (1983). Stochastic simulation of high-frequency ground motion, *Bulletin of the Seismological Society of America* [**73**], 1865 – 1894.

Boore, D. M. and J. Boatwright (1984). Average body-wave radiation coefficients, *Bulletin of the Seismological Society of America* [**74**], 1615 – 1621.

Brune, J. N. and C. R. Allen (1967). A micro-earthquake survey of the San Andreas fault system in southern California, *Bulletin of the Seismological Society of America* [**57**], 277 – 296.

Brune, J. N., R. Archuleta, and S. Hartzell (1979). Far-field S-wave spectra, corner frequencies and pulse shapes, *Journal of Geophysical Research* [**84**], 2262 – 2272.

Brune, J. N., J. B. Fletcher, F. Vernon, L. Haar, T. Hanks, and J. Berger (1986). Low stress-drop earthquakes in the light of new data from the Anza, California telemetered digital array, in *Earthquake Source Mechanics, Geophysical Monogram* [**37**], S. Das, J. Boatwright, and C. H. Scholtz (Editors), American Geophysical Union, Washington D.C., 237 –245.

Brune, J. N., T. L. Henyey, and R. F. Roy (1969). Heat flow, stress, and rate of slip along the San Andreas fault, California, *Journal of Geophysical Research* [**74**], 3821 – 3827.

Campillo, M. (1983). Numerical evaluation of near-field, high-frequency radiation form quasi-static circular faults, *Bulletin of the Seismological Society of America* [**73**], 723 – 734.

Dysart, P. S., J. A. Snoke, and I. S. Sacks (1988). Source parameters and scaling relations for small earthquakes in the Matsushiro Region, Southwest Honshu, Japan, *Bulletin of the Seismological Society of America* [**78**], 571 – 589.

Eshelby, J. D. (1959). The elastic field outside of an ellipsoidal inclusion, *Proceedings of The Royal Society of London. Series A.* [**252**], 561 – 569.

Eshelby, J. D. (1973). Dislocation theory for geophysical applications, *Proceedings of The Royal Society of London. Series A.* [**274**], 331 – 338.

Fletcher, J. B. (1980). Spectra from high-dynamic range digital recordings of Oroville, California, aftershocks and their source parameters, *Bulletin of the Seismological Society of America* [**70**], 735 – 755.

Fletcher, J. B. (1984). Source parameters for aftershocks of the Oroville, California, earthquake, *Bulletin of the Seismological Society of America* [**74**], 1101 – 1123.

Fletcher, J. B. and A. McGarr (2006). Distribution of stress drop, stiffness, and fracture energy over earthquake rupture zones, *Journal of Geophysical Research* [**111**], B03312, 1 – 12.

Frankel, A. (1982). The effects of attenuation and site response on the spectra of microearthquakes in the northeastern Caribbean, *Bulletin of the Seismological Society of America* [**72**], 1379 – 1402.

Gibowicz, S. J. (1973). Stress drop and aftershocks, *Bulletin of the Seismological Society of America* [**63**], 1433 – 1446.

Gibowicz, S. J. (1975). Variation of source properties: The Inangahua, New Zealand, aftershocks of 1968, *Bulletin of the Seismological Society of America* [**65**], 261 – 276.

Gibowicz, S. J. (1984). The mechanism of large mining tremors in Poland, in *Rockbursts and Seismicity in Mines*, N. C. Gay and E. H. Wainwright (Editors), South African Institute of Mining and Metallurgy, Johannesburg, Symposium Series [**6**], 17 – 28.

Hanks, T. C. (1977). Earthquake stress drops, ambient tectonic stresses and stresses that drive plate motions, *Pure and Applied Geophysics* [**115**], 441 – 458.

Hanks, T. C. (1979). *b* values and $\omega^{-\gamma}$ seismic source models: Implications of tectonic stress variations along active crustal fault zones and the estimation of high-frequency strong ground motion, *Journal of Geophysical Research* [**84**], 2235 – 2242.

Hanks, T. C. and M. Wyss (1972). The use of body-wave spectra in the determination of seismic-source parameters, *Bulletin of the Seismological Society of America* [**62**], 561 – 589.

Jin, A. and E. Fukuyamma (2005). Seismic energy for shallow earthquakes in southwest Japan, *Bulletin of the Seismological Society of America* [**95**], 1314 – 1333.

Joyner, W. B. and D. M. Boore (1986) On simulating large earthquakes by Green's-function addition of smaller earthquakes, in *Earthquake Source Mechanics, Geophysical Monogram* [**37**], S. Das, J. Boatwright, and C. H. Scholtz (Editors), American Geophysical Union, Washington D.C., 269 – 274.

Kanamori, H. and C. R. Allen (1986). Earthquake repeat time and average stress drop, in *Earthquake Source Mechanics, Geophysical Monogram* [**37**], S. Das, J. Boatwright, and C. H. Scholtz (Editors), American Geophysical Union, Washington D.C., 227 – 235.

Kanamori, H. and D. Anderson (1975). Theoretical basis of some empirical relations in seismology, *Bulletin of the Seismological Society of America* [**65**], 1073 – 1095.

Kanamori, H., J. Mori, E. Hauksson, T. H. Heaton, L. K. Hutton, and L. M. Jones (1993). Determination of earthquake energy release and M_L using Terrascope, *Bulletin of the Seismological Society of America* [**83**], 330 – 346.

Lockner, D. A., J. D. Byerlee, V. Kuksenko, A. Ponomarev, and A. Sidorin (1992). Chapter 1 – Observations of quasistatic fault growth from acoustic emissions, in *Fault Mechanics and Transport Properties of Rocks*, B. Evans and T. Wong (Editors), Academic, London, 3 – 31.

Madariaga, R. (1979). On the relation between seismic moment and stress drop in the presence of stress and strength heterogeneity, *Journal of Geophysical Research* [**84**], 2243 – 2250.

McGarr, A. (1971). Violent deformation of rock near deep-level, tabular excavations – Seismic events, *Bulletin of the Seismological Society of America* [**61**], 1453 – 1466.

McGarr, A. (1984). Scaling of ground motion parameters, state of stress, and focal depth, *Journal of Geophysical Research* [**89**], 6969 – 6979.

McGarr, A. (1986). Some observations indicating complications in the nature of earthquake scaling, in *Earthquake Source Mechanics, Geophysical Monogram* [**37**], S. Das, J. Boatwright, and C. H. Scholtz (Editors), American Geophysical Union, Washington D.C., 217 – 225.

McGarr, A., R. W. E. Green, and S. M. Spottiswoode (1981). Strong ground motion of mine tremors: Some implications for near-source ground motion parameters, *Bulletin of the Seismological Society of America* [**71**], 295 – 319.

McGarr, A., S. M. Spottiswoode, and N. C. Gay (1975). Relationship of mine tremors to induced stresses and to rock properties in the focal region, *Bulletin of the Seismological Society of America* [**65**], 981 – 993.

Modiano, T. and D. Hatzfeld (1982). Experimental study of the spectral content for shallow earthquakes, *Bulletin of the Seismological Society of America* [**72**], 1739 – 1758.

Mori, J., and A. Frankel (1990). Source parameters for small events associated with the 1986 North Palm Springs, California, earthquake determined using empirical Green functions, *Bulletin of the Seismological Society of America* [**80**], 278 – 295.

Mori, J., R. E. Abercrombie, and Hiroo Kanamori (2003). Stress drops and radiated energies of aftershocks of the 1994 Northridge, California, earthquake, *Journal of Geophysical Research* [**108**], ESE 13, 1 - 12.

Pomeroy, P. W., D. W. Simpson, and M. L. Sbar (1976). Earthquakes triggered by surface quarrying – The Wappingers Falls, New York sequence of June, 1974, *Bulletin of the Seismological Society of America* [**66**], 685 – 700.

Randall, M. J. (1972). Stress drop and the ratio of Seismic energy to Moment, *Journal of Geophysical Research* [**77**], 969 – 970.

Randall, M. J. (1973). The spectral theory of seismic sources, *Bulletin of the Seismological Society of America* [**63**], 1133 – 1144.

Rice, J. R. (1993). Spatio-temporal complexity of slip on a fault, *Journal of Geophysical Research* [**98**], 9885 – 9907.

Takahashi, T., H. Sato, M. Ohtake, and K. Obara (2005). Scale dependence of apparent stress for earthquakes along the subducting Pacific Plate in Northeastern Honshu, Japan, *Bulletin of the Seismological Society of America* [**95**], 1334 – 1345.

Taylor, D. W. A., J. A. Snoke, I. S. Sacks, and T. Takanami (1990). Nonlinear frequency-magnitude relationships for the Hokkaido Corner, Japan, *Bulletin of the Seismological Society of America* [**80**], 340 – 353.

Turcotte, D. L. (1989). Fractals in geology and geophysics, *Pure and Applied Geophysics* [**131**], 171 – 196.

Walsh, J. B. (1965). The effect of cracks on the uniaxial elastic compression of rocks, *Journal of Geophysical Research* [**70**], 399 – 411.

Walsh, J. B. (1965). The effect of cracks in rocks on Poisson's ratio, *Journal of Geophysical Research* [**70**], 5249 – 5257.

Walsh, J. B. (1966). Seismic wave attenuation in rock due to friction, *Journal of Geophysical Research* [**71**], 2591 – 2599.

Wyss, M. (1970). Stress estimates for the South American shallow and deep earthquakes, *Journal of Geophysical Research* [**75**], 1529 – 1544.

Appendix 1: Integral of the Power Spectra assuming a Brune Source Spectral Shape

In this section we evaluate the Integral of the square of the ground motion Spectra (or Power Spectra) assuming the Brune [1970, 1971] model for the Source Spectral Shape. We first define the Fourier Amplitude Spectrum of the Far-field Ground Displacement, $U(f)$, after the model presented by Brune [1970, 1971]. $U(f)$ takes the form

$$|U(f)| = \frac{\Omega_0}{\left[1 + \left(f/f_c\right)^2\right]},$$

where (f) is the frequency, (Ω_0) is the Zero-Frequency Displacement Amplitude and (f_c) is the corner frequency. The Fourier Amplitude Spectrum of the Far-field Ground Velocity, $\dot{U}(f)$, is found by multiplying the Displacement Amplitude, $U(f)$, at each frequency by $2\pi f$. $\dot{U}(f)$ may be written as

$$\dot{U}(f) = U(f) \cdot 2\pi f = \frac{(2\pi f)(f_c)^2}{(f_c)^2 + (f)^2} \Omega_0$$

The solution to the integral of the square of the ground displacement and ground velocity, I_{D2} and I_{V2}, can be obtained in either the time domain or the frequency domain (by Parseval's Relation). In the frequency domain, the solution to the integrals of the square of the ground motion can be computed as follows:

$$I_{D^2} = \int_{-\infty}^{+\infty} \left|U(f)\right|^2 df$$

$$= 2\int_0^{+\infty} \left|U(f)\right|^2 df$$

$$= 2\int_0^{+\infty} \left(\frac{\Omega_0(f_c)^2}{(f_c)^2 + (f)^2}\right)^2 df$$

$$= 2(\Omega_0)^2 \int_0^{+\infty} \left(\frac{(f_c)^2}{(f_c)^2 + (f)^2}\right)^2 df$$

$$I_{V^2} = \int_{-\infty}^{+\infty} \left|\dot{U}(f)\right|^2 df$$

$$= 2\int_0^{+\infty} \left|\dot{U}(f)\right|^2 df$$

$$= 2\int_0^{+\infty} \left(\frac{(2\pi f)(f_c)^2}{(f_c)^2 + (f)^2}\Omega_0\right)^2 df$$

$$= 8\pi^2 (\Omega_0)^2 (f_c)^4 \int_0^{+\infty} \left(\frac{f}{(f_c)^2 + (f)^2}\right)^2 df$$

- We prescribe a trigonometric relationship between the frequency (f) and the corner frequency (f_c), as in the figure below.
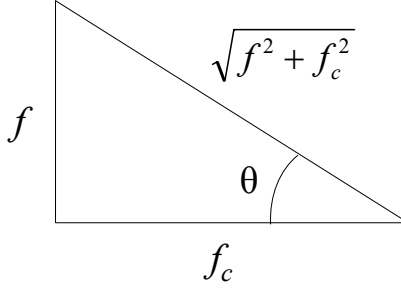
- The relationship between the frequency, corner frequency and θ is:

$$\tan(\theta) = \frac{f}{f_c}$$

$$\cos(\theta) = \frac{f_c}{\sqrt{(f_c)^2 + (f)^2}}$$

- By using the above relationship, we convert the integrand that is in terms of f and f_c into an integrand that is in terms of θ and f_c:

  ○ $\dfrac{(f_c)^2}{(f_c)^2 + (f)^2} = \cos^2(\theta)$

  ○ $f = f_c \tan(\theta)$

  ○ $(f_c)^2 + (f)^2 = \left(\dfrac{f_c}{\cos(\theta)}\right)^2$

  ○ $\left(\dfrac{f}{(f_c)^2 + (f)^2}\right)^2 = \left(\dfrac{f_c \tan(\theta)}{\left(f_c / \cos(\theta)\right)^2}\right)^2 = \dfrac{\sin^2(\theta) \cdot \cos^2(\theta)}{(f_c)^2}$

  ○ The limits of integration change by:

  $$0 \le f \le +\infty \quad \Rightarrow \quad \theta = \tan^{-1}\left(\frac{f}{f_c}\right) \quad \Rightarrow \quad \tan^{-1}\left(\frac{0}{f_c}\right) \le \theta \le \tan^{-1}\left(\frac{+\infty}{f_c}\right)$$

  $$\Rightarrow \qquad 0 \le \theta \le \frac{\pi}{2}$$

  ○ The variable of integration changes by:

  $$f = f_c \tan(\theta) \quad \Rightarrow \quad \frac{df}{d\theta} = f_c \sec^2(\theta) \quad \Rightarrow \quad df = f_c \sec^2(\theta)\, d\theta$$

- Trigonometric substitution into the integral of the displacement power spectra yields:

$$I_{D^2} = 2(\Omega_0)^2 \int_0^{+\infty} \left(\frac{(f_c)^2}{(f_c)^2 + (f)^2} \right)^2 df$$

$$= 2(\Omega_0)^2 \int_0^{\frac{\pi}{2}} \left(\cos^4(\theta) \right) \cdot \left(f_c \sec^2(\theta) \right) d\theta$$

$$= 2(\Omega_0)^2 (f_c) \int_0^{\frac{\pi}{2}} \cos^2(\theta) \, d\theta$$

$$= 2(\Omega_0)^2 (f_c) \int_0^{\frac{\pi}{2}} \left(\frac{1 + \cos(2\theta)}{2} \right) d\theta$$

$$= (\Omega_0)^2 (f_c) \int_0^{\frac{\pi}{2}} \left(1 + \cos(2\theta) \right) d\theta$$

$$= (\Omega_0)^2 (f_c) \left[\left(\theta + \frac{1}{2} \sin(2\theta) \right) \Big|_0^{\frac{\pi}{2}} \right]$$

$$= (\Omega_0)^2 (f_c) \left[\left(\frac{\pi}{2} + \frac{1}{2} \sin(\pi) \right) - \left(0 + \sin(0) \right) \right]$$

$$= \boxed{\frac{\pi (\Omega_0)^2 (f_c)}{2}}$$

This result is given between Equations (9) and (10) by Andrews [1986].

-    Trigonometric substitution into the integral of the velocity power spectra yields:

$$I_{V^2} = 8\pi^2(\Omega_0)^2(f_c)^4 \int_0^{+\infty}\left(\frac{f}{(f_c)^2+(f)^2}\right)^2 df$$

$$= 8\pi^2(\Omega_0)^2(f_c)^4 \int_0^{\frac{\pi}{2}}\left(\frac{\sin^2(\theta)\cdot\cos^2(\theta)}{(f_c)^2}\right)\cdot\left(f_c\sec^2(\theta)\right)d\theta$$

$$= 8\pi^2(\Omega_0)^2(f_c)^4 \int_0^{\frac{\pi}{2}}\left(\frac{\sin^2(\theta)}{(f_c)}\right)d\theta$$

$$= 8\pi^2(\Omega_0)^2(f_c)^3 \int_0^{\frac{\pi}{2}}\sin^2(\theta)\,d\theta$$

$$= 8\pi^2(\Omega_0)^2(f_c)^3 \int_0^{\frac{\pi}{2}}\left(\frac{1-\cos(2\theta)}{2}\right)d\theta$$

$$= 4\pi^2(\Omega_0)^2(f_c)^3 \int_0^{\frac{\pi}{2}}(1-\cos(2\theta))d\theta$$

$$= 4\pi^2(\Omega_0)^2(f_c)^3\left[\left(\theta-\frac{1}{2}\sin(2\theta)\right)\Big|_0^{\frac{\pi}{2}}\right]$$

$$= 4\pi^2(\Omega_0)^2(f_c)^3\left[\left(\frac{\pi}{2}-\frac{1}{2}\sin(\pi)\right)-(0-\sin(0))\right]$$

$$= \boxed{2\pi^3(\Omega_0)^2(f_c)^3}$$

This result is given between Equations (9) and (10) by Andrews [1986].

The results for the integrals of the square of the ground motion may also be derived in the time domain, using Parseval's Relation (Equation 2.13). Using Equation (2.1) and assuming the Heaviside function is unity when $t \geq 0$, the integrals in the time domain become:

$$I_{D^2} = \int_0^{+\infty}\Omega_0\frac{t}{\tau^2}e^{-t/\tau}dt \quad \text{and} \quad I_{V^2} = \int_0^{+\infty}\left[\Omega_0\frac{1}{\tau^2}e^{-t/\tau}-\Omega_0\frac{t}{\tau^3}e^{-t/\tau}\right]dt$$

Appendix 2: Correction for Bandwidth Limitations

In this section we determine corrections to be applied to our estimates of the integrals of the velocity and displacement power spectra for the effects of the bandwidth limitations after Snoke [1987]. The corrections assume that the Fourier Amplitude Spectra of the ground motion conform to the model proposed by Brune [1970, 1971]. For continuous data conforming to Brune's model, the Integrals of the Velocity and Displacement Power Spectra are

$$I_{V^2} = \int_{-\infty}^{+\infty} \left(\dot{u}(t) \right)^2 dt = \int_{-\infty}^{+\infty} \left| \dot{U}(f) \right|^2 df = 2\int_{0}^{+\infty} \left| \dot{U}(f) \right|^2 df$$

$$I_{D^2} = \int_{-\infty}^{+\infty} \left(u(t) \right)^2 dt = \int_{-\infty}^{+\infty} \left| U(f) \right|^2 df = 2\int_{0}^{+\infty} \left| U(f) \right|^2 df \quad ,$$

where (t) and (f) represent continuous time and frequency (respectively), $(\dot{u}(t))$ and $(u(t))$ represent the ground velocity and ground displacement time series (respectively), $(\dot{U}(f))$ and $(U(f))$ represent the Fourier amplitude spectra of the ground velocity and ground displacement time series (respectively), and the factor of 2 outside of the integral for only positive frequencies (far right) accounts for the negative frequencies (since $\dot{U}(f) = \left[\dot{U}(-f) \right]^*$ and $U(f) = \left[U(-f) \right]^*$, where (*) denotes the complex conjugate).

As discussed by Snoke [1987], real data represent the discrete approximation of continuous ground motion. Instruments are only capable of recording a finite number of samples (N) at a finite sample rate (Δt). The Integrals for the Velocity and Displacement Power Spectra therefore become discrete summations in the time or frequency domain such that

$$I_{V^2} = \Delta t \cdot \sum_{\tau=0}^{N-1} \left(\dot{u}(\theta \cdot \Delta t) \right)^2 = \Delta f \cdot \sum_{\nu=-\frac{N}{2}}^{\frac{N}{2}} \left| \dot{U}(\nu \cdot \Delta f) \right|^2 = 2\Delta f \cdot \sum_{\nu=0}^{\frac{N}{2}} \left| \dot{U}(\nu \cdot \Delta f) \right|^2$$

$$I_{D^2} = \Delta t \cdot \sum_{\tau=0}^{N-1} \left(u(\theta \cdot \Delta t) \right)^2 = \Delta f \cdot \sum_{\nu=-\frac{N}{2}}^{\frac{N}{2}} \left| U(\nu \cdot \Delta f) \right|^2 = 2\Delta f \cdot \sum_{\nu=0}^{\frac{N}{2}} \left| U(\nu \cdot \Delta f) \right|^2 \quad ,$$

where (θ) represents the sample point in the time domain, (N) represents the number of samples in the time or frequency domain, (ν) represents the sample in the positive or negative frequency domain and (Δf) is the frequency interval with the relation $(\Delta f = (N \cdot \Delta t)^{-1})$.

In addition to the artificial limitations imposed by the recording procedure, real data are also affected by noise contamination. Noise contamination will typically reduce the lower and upper spectral bandwidth limits from the original/observable range $(0 - N \cdot \Delta f / 2)$ to a subset of the original range $(v_1 \cdot \Delta f - v_2 \cdot \Delta f)$. We assume that in the absence of noise contamination and recording limitations that the Fourier Amplitude Spectra for the ground velocity and the ground displacement will conform to the Brune model [1970, 1971]. If the Zero-Frequency Displacement Amplitude (Ω_0) and the Corner Frequency (f_c) are defined within the spectral limits $(v_1 \cdot \Delta f - v_2 \cdot \Delta f)$, then it is possible to apply correction factors to account for the spectral amplitudes that are assumed to exist outside of the spectral bandwidth imposed by the recording procedure or noise contamination. The discrete summations in the frequency domain become

$$ I_{V^2} = C_{V^2}^{\langle 1 \rangle} + 2\Delta f \cdot \sum_{v=v_1}^{v_2} \left| \dot{U}(v \cdot \Delta f) \right|^2 + C_{V^2}^{\langle 2 \rangle} $$

$$ I_{D^2} = C_{D^2}^{\langle 1 \rangle} + 2\Delta f \cdot \sum_{v=v_1}^{v_2} \left| U(v \cdot \Delta f) \right|^2 + C_{D^2}^{\langle 2 \rangle} $$

where $(C_{V^2}^{\langle 1 \rangle})$ and $(C_{V^2}^{\langle 2 \rangle})$ represent the spectral correction factors that account for the missing bandwidth in the velocity power spectra for frequencies less than $(v_1 \cdot \Delta f)$ and greater than $(v_2 \cdot \Delta f)$, while $(C_{D^2}^{\langle 1 \rangle})$ and $(C_{D^2}^{\langle 2 \rangle})$ represent the spectral correction factors that account for the missing bandwidth in the displacement power spectra for frequencies less than $(v_1 \cdot \Delta f)$ and greater than $(v_2 \cdot \Delta f)$.

We approximate the correction factors under the assumption that

$$U(f \leq f_c) = \Omega_0$$

$$U(f > f_c) = \left(\frac{f_c}{f}\right)^2 \cdot \Omega_0 \text{ , Hanks and Thatcher [1972]}$$

which represents an approximation to the Brune model, using straight lines, for the Fourier Amplitude Spectrum of the Ground Displacement. When analyzing real data, however, the corner frequency is typically not constrained well enough by visual inspection to use it in this context. Instead, by adapting the method used to estimate the Zero-Frequency Displacement Amplitude (Ω_0) we can estimate the Zero-Period Acceleration Amplitude (Ψ_0) from the acceleration spectra by calculating the geometric mean of a window of high-frequency (or low-period) amplitudes from the acceleration spectrum. This leads to an approximation for the acceleration spectrum, using straight lines, where the amplitudes at frequencies greater than (f_c) are now independent of (f_c)

$$\ddot{U}(f \leq f_c) = \left(\frac{f}{f_c}\right)^2 \cdot \Psi_0$$

$$\ddot{U}(f > f_c) = \Psi_0$$

Under these assumptions we can determine the approximate correction factors that will account for the frequencies outside of the spectral limits ($v_1 \cdot \Delta f$ to $v_2 \cdot \Delta f$). The correction factors for the Integrals of the Velocity and Displacement Power Spectra, assuming $v_1 \cdot \Delta f << f_c$, $v_2 \cdot \Delta f >> f_c$ and $\dot{U}(f) = \left[\dot{U}(-f) \right]_*$ (where * denotes complex conjugate), become

$$C_{V^2}^{\langle 1 \rangle} = 2 \cdot \int_0^{v_1 \cdot \Delta f} \left| \dot{U}(f) \right|^2 df = 8\pi^2 \cdot \int_0^{v_1 \cdot \Delta f} \left| f \cdot U(f) \right|^2 df = \frac{8}{3}\pi^2 (\Omega_0)^2 \cdot \left[f^3 \right]_0^{v_1 \cdot \Delta f_1}$$

$$= \boxed{\frac{8}{3}\pi^2 (\Omega_0)^2 (v_1 \cdot \Delta f)^3}$$

$$C_{V^2}^{\langle 2 \rangle} = 2 \cdot \int_{v_2 \cdot \Delta f}^{\infty} \left| \dot{U}(f) \right|^2 df = \frac{1}{2\pi^2} \cdot \int_{v_2 \cdot \Delta f}^{\infty} \left| \frac{\ddot{U}(f)}{f} \right|^2 df = \frac{1}{2\pi^2} (\Psi_0)^2 \cdot \left[-\frac{1}{f} \right]_{v_2 \cdot \Delta f}^{\infty}$$

$$= \boxed{\frac{(\Psi_0)^2}{2\pi^2 (v_2 \cdot \Delta f)}}$$

$$C_{D^2}^{\langle 1 \rangle} = 2 \cdot \int_0^{v_1 \cdot \Delta f} \left| U(f) \right|^2 df = \frac{2}{3} (\Omega_0)^2 \cdot \left[f \right]_0^{v_1 \cdot \Delta f_1}$$

$$= \boxed{\frac{2}{3} (\Omega_0)^2 (v_1 \cdot \Delta f)}$$

$$C_{D^2}^{\langle 2 \rangle} = 2 \cdot \int_{v_2 \cdot \Delta f}^{\infty} \left| U(f) \right|^2 df = \frac{1}{8\pi^4} \cdot \int_{v_2 \cdot \Delta f}^{\infty} \left| \frac{\ddot{U}(f)}{f^2} \right|^2 df = \frac{1}{24\pi^4} (\Psi_0)^2 \cdot \left[-\frac{1}{f^3} \right]_{v_2 \cdot \Delta f}^{\infty}$$

$$= \boxed{\frac{(\Psi_0)^2}{24\pi^4 (v_2 \cdot \Delta f)^3}}$$

The correction factors for the low-frequency spectral amplitudes are the same as that discussed in Snoke [1987]. The only thing novel here is basing the correction factors for the high-frequency spectral amplitudes on Ψ_0, which has applications for spectra with high-frequency amplitudes that are not well constrained.

Appendix 3: Ratio between the Apparent Stress and the Brune Stress Drop

As done by Hanks and Thatcher [1972], the most straightforward way to calculate the ratio between the Apparent Stress and the Brune Stress Drop is to first reduce and simplify the terms associated with the Apparent Stress. The Source Parameters Seismic Moment as developed by Keilis-Borok [1960] can be estimated for the S-wave energy using

$$M_0 = \frac{4\pi\rho\beta^3 R\Omega_0}{R_{\phi\theta}}$$

The radiated Seismic Energy as developed by Boatwright and Fletcher [1984] is measured for the S-wave energy using

$$E_s = \frac{4\pi\rho\beta R^2 \left\langle R_{\phi\theta}\right\rangle^2}{R_{\phi\theta}^{\,2}} I_{V^2}$$

If we assume the Fourier Amplitude Spectra of the ground motion conform to the Brune [1970, 1971] model, then the Integral of the Velocity Power Spectrum (I_{V2}) can be characterized in terms of the Zero-Frequency Displacement Amplitude (Ω_0) and the Corner Frequency (f_c) using the solution obtained in Appendix (1). The equation for the Radiated Seismic Energy becomes

$$E_s = \frac{4\pi\rho\beta R^2 \left\langle R_{\phi\theta}\right\rangle^2}{R_{\phi\theta}^{\,2}} \left(2\pi^3 (\Omega_0)^2 (f_c)^3\right)$$

If we substitute the equations for the Radiated Seismic Energy and the Seismic Moment into the equation for the Apparent Stress, after Wyss and Brune [1968], we have

$$\sigma_a = \mu \frac{E_s}{M_0}$$

$$= \mu \frac{\dfrac{4\pi\rho\beta\, R^2 \left\langle R_{\phi\theta}\right\rangle^2}{R_{\phi\theta}^{\,2}} \left(2\pi^3 (\Omega_0)^2 (f_c)^3\right)}{\dfrac{4\pi\rho\beta^3 R\Omega_0}{R_{\theta\phi}}}$$

$$= 2\pi^3 \rho R\Omega_0 (f_c)^3 \frac{\left\langle R_{\phi\theta}\right\rangle^2}{R_{\phi\theta}}$$

The ratio between the Apparent Stress and the Brune Stress Drop, after Brune [1970, 1971] for $\langle R_{\theta\phi} \rangle = \sqrt{2/5}$ [Aki and Richards (2002), pg. 115] becomes:

$$\frac{\sigma_a}{\sigma_B} = \frac{2\pi^3 \rho R \Omega_0 (f_c)^3 \dfrac{\langle R_{\phi\theta} \rangle^2}{R_{\phi\theta}}}{\left(\dfrac{7}{16}\right) \dfrac{4\pi\rho\beta^3 R\Omega_0}{R_{\theta\phi}} \left(\dfrac{2\pi f_c}{\beta\sqrt{7\pi/4}}\right)^3}$$

$$= \frac{(7\pi)^{3/2}}{56\pi} \langle R_{\phi\theta} \rangle^2$$

$$= \frac{(7\pi)^{3/2}}{140\pi} \approx 0.2345$$

This is the same result obtained by both Andrews [1986] and Snoke [1987]:

$$\frac{\sigma_B}{\sigma_a} = \frac{140\pi}{(7\pi)^{3/2}} \approx 4.265$$

Appendix 4: The Effect of an Uncertain Data Sample Rate on Estimating Source Parameters

This section addresses the effect of an uncertain data sample rate on estimating the Seismic Moment, Radiated Seismic Energy, Apparent Stress and Brune Stress Drop. In this analysis we assume and define the following:

- The initial data are instrument corrected and represent the VELOCITY of the recorded motion (this must be satisfied in order for the analysis in the section to hold)
- The sample points representing the P-wave arrival (T_P) and the S-wave arrival (T_S) are known
- Fourier transform of the S-wave Window in the time domain results in the Brune theoretical spectral shape in the frequency domain
- The assumed time interval is Δt_A (seconds / sample)
- The real (actual) time interval is Δt_R (seconds / sample)
- The material properties (density and wave velocity) and radiation pattern are known
- The only quantities that depend on the sample rate are:
  - Difference in time between P-wave arrival and S-wave arrival, i.e. $(T_S - T_P) \cdot \Delta t$
  - Zero-Frequency Displacement Amplitude (Ω_0)
  - Source Spectrum Corner Frequency (f_c)

Consider the velocity record of an event where the P-wave arrival occurs at sample point (T_P) and the S-wave arrival occurs at sample point (T_S). To determine the hypocentral distance between the event and the instrument in terms of the P- and S-wave velocities (α and β, respectively) as well as the P- and S-wave arrival times ($T_P \cdot \Delta t$ and $T_S \cdot \Delta t$, respectively), one can use the following equation:

$$ R(\Delta t) = \frac{\alpha\beta(T_S - T_P)\Delta t}{(\alpha - \beta)} $$

Based on the above expression for the hypocentral distance, the number of samples between the P-wave arrival and the S-wave arrival are known. However, uncertainty in the sample rate leads to uncertainty (proportional to Δt) in the actual amount of time separating the P-wave arrival and S-wave arrival.

To determine the Zero-Frequency Displacement Amplitude from a windowed section of the velocity time-series $\mathring{u}(t)$, it is necessary to first convert the discrete velocity time-series $\mathring{u}(t)$ into the frequency domain $\mathring{U}(f)$. This can be done by computing the Discrete Fourier Transform for discrete time sample (θ), discrete frequency sample (ν) and a windowed velocity time-series $\mathring{u}(t)$ of N discrete samples:

$$\dot{U}(\nu \cdot \Delta f, \Delta t) = \Delta t \cdot \sum_{\theta=0}^{N-1} \dot{u}(\theta \cdot \Delta t) \cdot e^{-i2\pi\nu\theta/N}$$

The Zero-Frequency Displacement Amplitude (at the first non-zero frequency sample point, i.e. $\nu_1 = 1$) is:

$$\Omega_0(\Delta t) = U(\nu_1 \cdot \Delta f, \Delta t) = \frac{\dot{U}(\Delta f, \Delta t)}{2\pi\Delta f} = \frac{\dot{U}(\Delta f, \Delta t)}{2\pi\left(\dfrac{1}{N \cdot \Delta t}\right)} = \frac{(N \cdot \Delta t^2)}{2\pi} \cdot \sum_{t=0}^{N-1} \dot{u}(t) \cdot e^{-i2\pi\theta/N}$$

Based on the above expression for the zero-frequency displacement amplitude, the forward Fourier transform introduces uncertainty proportional to Δt and the derivative of the velocity spectrum in the frequency domain introduces additional uncertainty proportional to Δt. This leads to uncertainty in estimating the zero-frequency displacement amplitude proportional to Δt^2.

The corner frequency can be estimated by inspection from either the velocity or displacement frequency spectra. If the corner frequency is observed to occur at frequency sample ν_{f_c}, then the corner frequency will be equivalent to:

$$f_c(\Delta t) = \nu_{f_c} \cdot \Delta f = \frac{\nu_{f_c}}{N \cdot \Delta t}$$

Based on the above expression, the uncertainty in the estimate of the corner frequency is proportional to $1 / \Delta t$.

If we assume a time interval of Δt_A and further assume that this time interval represents the lower bound of the real time interval Δt_R, (i.e. $\Delta t_R = \varepsilon \cdot \Delta t_A$ | where $\varepsilon = 1, 2, 3, \dots, 25$), then we can determine the effects of an uncertain sample interval on the estimates of the hypocentral distance, the zero-frequency displacement amplitude and the corner frequency by comparing the ratio between estimates using Δt_A and estimates using Δt_R:

$$\frac{R(\Delta t_A)}{R(\Delta t_R)} = \frac{\Delta t_A}{\Delta t_R} = \frac{\Delta t_A}{\varepsilon \cdot \Delta t_A} = \frac{1}{\varepsilon}$$

$$\frac{\Omega_0(\Delta t_A)}{\Omega_0(\Delta t_R)} = \left(\frac{\Delta t_A}{\Delta t_R}\right)^2 = \left(\frac{\Delta t_A}{\alpha \cdot \Delta t_A}\right)^2 = \frac{1}{\varepsilon^2}$$

$$\frac{f_c(\Delta t_A)}{f_c(\Delta t_R)} = \left.\frac{\dfrac{1}{\Delta t_A}}{\dfrac{1}{\Delta t_R}}\right. = \frac{\Delta t_R}{\Delta t_A} = \frac{\varepsilon \cdot \Delta t_A}{\Delta t_A} = \varepsilon$$

Each of the above ratios quantifies the effect of an uncertain sample rate. If $\varepsilon \neq 1$ and is not accounted for properly, the estimates of the hypocentral distance will be under-estimated by ε^{-1}, the zero-frequency displacement amplitude will be under-estimated by ε^{-2} and the corner frequency will be over-estimated by ε. By applying similar logic, the equations for the Seismic Moment, Radiated Seismic Energy, Apparent Stress, and Brune Stress Drop as a function of the sample interval are:

The Seismic Moment (M_0) after Keilis-Borok [1960] -

$$M_0(\Delta t) = \frac{4\pi\rho\beta^3 R(\Delta t) \cdot \Omega_0(\Delta t)}{\mathcal{R}_{\phi\theta}}$$

The Radiated Seismic Energy (E_s) after Boatwright and Fletcher [1984]
Substitution for the solution to the integral, I_{V2}, from Appendix (2) -

$$E_s(\Delta t) = \frac{4\pi\rho\beta(R(\Delta t))^2 <\mathcal{R}_{\phi\theta}>^2}{\mathcal{R}_{\phi\theta}^2}\left(I_{V^2}(\Delta t)\right) = \frac{4\pi\rho\beta(R(\Delta t))^2 <\mathcal{R}_{\phi\theta}>^2}{\mathcal{R}_{\phi\theta}^2}\left(2\pi^3(f_c(\Delta t))^3(\Omega_0(\Delta t))^2\right)$$

The Apparent Stress (σ_a) after Wyss and Brune [1968] -

$$\sigma_a(\Delta t) = \mu\frac{E_s(\Delta t)}{M_0(\Delta t)}$$

The Brune Stress Drop (σ_B) after Brune [1970, 1971] -

$$\sigma_B(\Delta t) = \left(\frac{2\pi(f_c(\Delta t))}{\beta\sqrt{7\pi/4}}\right)^3\left(\frac{7}{16}\right)(M_0(\Delta t))$$

The effects of an uncertain sample rate on the estimates of the Seismic Moment, Radiated Seismic Energy, Apparent Stress and Brune Stress Drop are then:

$$\frac{M_0(\Delta t_A)}{M_0(\Delta t_R)} = \left(\frac{R(\Delta t_A)}{R(\Delta t_R)}\right)\left(\frac{\Omega_0(\Delta t_A)}{\Omega_0(\Delta t_R)}\right)^2 = \left(\frac{\Delta t_A}{\Delta t_R}\right)\left(\frac{\Delta t_A}{\Delta t_R}\right)^2 = \left(\frac{\Delta t_A}{\Delta t_R}\right)^3 = \left(\frac{\Delta t_A}{\varepsilon \cdot \Delta t_A}\right)^3 = \frac{1}{\varepsilon^3}$$

$$\frac{E_s(\Delta t_A)}{E_s(\Delta t_R)} = \left(\frac{R(\Delta t_A)}{R(\Delta t_R)}\right)^2\left(\frac{f_c(\Delta t_A)}{f_c(\Delta t_R)}\right)^3\left(\frac{\Omega_0(\Delta t_A)}{\Omega_0(\Delta t_R)}\right)^2 = \left(\frac{\Delta t_A}{\Delta t_R}\right)^2\left(\frac{\frac{1}{\Delta t_A}}{\frac{1}{\Delta t_R}}\right)^3\left(\frac{\Delta t_A}{\Delta t_R}\right)^4 = \left(\frac{\Delta t_A}{\Delta t_R}\right)^3 = \left(\frac{\Delta t_A}{\varepsilon \cdot \Delta t_A}\right)^3 = \frac{1}{\varepsilon^3}$$

$$\frac{\sigma_a(\Delta t_A)}{\sigma_a(\Delta t_R)} = \frac{\left(E_s(\Delta t_A)\middle/M_0(\Delta t_A)\right)}{\left(E_s(\Delta t_R)\middle/M_0(\Delta t_R)\right)} = \frac{\left(\Delta t_A\middle/\Delta t_A\right)^3}{\left(\Delta t_R\middle/\Delta t_R\right)^3} = 1$$

$$\frac{\sigma_B(\Delta t_A)}{\sigma_B(\Delta t_R)} = \frac{\left((f_c(\Delta t_A))^3 \cdot M_0(\Delta t_A)\right)}{\left((f_c(\Delta t_R))^3 \cdot M_0(\Delta t_R)\right)} = \frac{\left(\left(\frac{1}{\Delta t_A}\right)^3 \cdot (\Delta t_A)^3\right)}{\left(\left(\frac{1}{\Delta t_R}\right)^3 \cdot (\Delta t_R)^3\right)} = 1$$

Each ratio above quantifies the effect of an uncertain sample rate on each source parameter. If $\varepsilon \neq 1$ and is not accounted for properly, the estimates of the Seismic Moment will be under-estimated by ε^{-3}, the Radiated Seismic Energy will be under-estimated by ε^{-3} and the Apparent Stress in addition to the Brune Stress Drop will be unaffected.